Big-bang nucleosynthesis with a long-lived slepton and a 125 GeV Higgs boson in the (next-to-)minimal super symmetric standard model

125 GeV

Graduate School of Science and Engeneering
Course in Material Science

11DS001
Shingo Ohta

March 4, 2014

In this thesis, we investigate allowed parameter region in the next-to-minimal supersymmetric standard model (NMSSM) where correct dark matter relic density, light elements abundances, and the Higgs mass are obtained simultaneously.

First, we review some phenomenological problems in the standard model (SM) of particle physics. There are several shortcomings in the SM though it have been precisely confirmed by many experiments. In this thesis we especially focus on the lepton flavor violation (LFV), the existence of dark matter, and the lithium problems in the standard Big-bang nucleosynthesis (BBN).

Next, we confirm that observed light elements (including lithium(s)) abundances are obtained as well as dark matter relic density in the minimal supersymmetric standard model (MSSM). We consider slepton coannihilation scenario to obtain observed dark matter relic density, where the bino-like neutralino is the lightest supersymmetric particle (LSP), the lightest slepton is the next-to-lightest one (NLSP), and their masses are tightly degenerated. The slepton can be long-lived due to the mass degeneracy and affect the BBN forming bound state with light element nucleus. The success of such exotic BBN requires sufficient longevity and the number density of the slepton and the rates of the exotic BBN processes caused by bound state effects. We note that the LFV decay of the slepton can make the lifetime much shorter than that in case where the slepton has only stau component. We show that in both case with/without LFV, there exists the parameter region of the MSSM where observed dark matter relic density and light elements abundances are obtained.

Finally, we extend the framework into the NMSSM and observed Higgs mass is also obtained. In the NMSSM a singlet scalar contributes to the Higgs sector. It arises new tree contributions with couplings, λ and κ, in the Higgs boson mass, and they can push it up to the experimental value easier comparing to the case of the MSSM. In the neutralino sector, singlino, which is superpartner of the singlet scalar, exist and we mainly consider the case where the lightest neutralino is singlino-like. The coupling relevant to the decay of the slepton includes the NMSSM parameters, λ and κ, and is typically much smaller than that in case where the lightest neutralino is bino-like in the MSSM. We know the favorable range of the lifetime of the slepton and relevant timescales of the exotic BBN processes for solving lithium problems. However, the small couplings easily lead to too long lifetime of the slepton and/or timescales of the exotic BBN processes. Thus we first calculate those values and require them to be in favorable range for solving lithium problems to obtain a favored region on λ-κ plane. Next we choose several points on the favored region, and calculate the dark matter relic density and the Higgs mass at each point using a numerical calculation code to confirm whether the values are consistent with the observations. Then we calculate the slepton relic density and light elements abundances at each point where observed dark matter relic density and the Higgs mass are obtained. In this thesis we investigate such allowed region following the above procedure in three cases; (i) small λ-κ region with large $\tan\beta$ for singlino-like LSP, (ii) large λ-κ region with small $\tan\beta$ for singlino-like LSP, and (iii) large λ-κ region with small $\tan\beta$ for bino-like LSP. At last, we show the allowed parameter region in the NMSSM where correct dark matter relic density, light elements abundances, and the Higgs mass are obtained simultaneously.

Contents

Chapter 1

Introduction

The flame work of the SM of particle physics is established in 1970s, and since then, it has been precisely verified by many experiments. All the particle contents in the SM had finally been obtained by the discovery of the Higgs boson in 2012 [1, 2]. However, a number of questions which suggest the presence of a more fundamental theory has still been left. For instance, the existence of dark matter has often been discussed in many extended models since it verified by observations. Supersymmetric models are attractive candidates for such a theory. The simplest extension, the MSSM, is often analyzed. The LSP should be neutral and stable, and thus can be a candidate of the dark matter. One of the other extension is the NMSSM which includes an extra singlet scalar sueprmultiplet. This account for so-called μ-problem [3] that complicates the MSSM, and better reconciles with the observed Higgs mass. The MSSM predicts a Higgs mass lighter than that of the Z boson at the tree level, and requires significant loop contribution to lift it up to the observed value, about 125 GeV. On the other hand, the Higgs mass in the NMSSM has additional terms contributed from the singlet, and it potentially offers a straight forward interpretation of the observations.

A series of works by the present authors explored impacts of the supersymmetry on the nucleosynthesis in the early universe [4, 5, 6, 7, 8]. Focus in these works have been on the case where the next-to-lightest supersymmetric particle (NLSP) is charged and long-lived so that it survives until the time of nucleosynthesis after the big-bang. It takes part in the nuclear reactions and alters the present-day abundance of the light elements. Possible disagreement indeed persists on the abundance of lithium compared with the calculation based on the Standard Model. The standard calculation predicts the ratio of abundance $\mathrm{Log}_{10}(^7\mathrm{Li}/\mathrm{H})$ to be -9.35 ± 0.06 [7], while the observation indicates -9.63 ± 0.06 [9]. Lithium 6 provides another possible disagreement; its observed ratio of abundance $^6\mathrm{Li}/^7\mathrm{Li} = 0.046 \pm 0.022$ is about 10^2–10^3 larger than the theoretical prediction [10]. These discrepancies can be the trace of the interaction between nuclei and the NLSP which is absent in the standard BBN sceanrio. Our scenario can thereby account for the abundance of the dark matter and of the lithium in a single framework. We analyzed if this scenario works within the MSSM with staus as the NLSP and neutralinos as the LSP, and found the parameter region that can account for these observational handles to the new physics [4, 5, 6, 7].

Now that the mass of Higgs particle is determined, we are to examine whether it is compatible with our scenario. Our previous work analyzed the constrained minimal supersymmetric standard model [11]. There we found allowed regions in the parameter space, and presented phenomenological predictions such as mass spectra and branching ratios. In the present paper, we further extend our scenario to the NMSSM with the flavor violation and search for its further applications. We demonstrate that the NMSSM under our scenario can simultaneously account for the three phenomenological clues: the abundance of dark matter, that of lithium, and Higgs mass. We explore parameter space and discover parameter points that qualify the requirements. Special interest is in the case where the NMSSM singlet is the major component of the neutralino LSP in expectation of the difference from

the MSSM. The case of bino-like neutralino is analyzed as well.

This thesis is organized as followes: In Chap. 2, we introduce some shortcomings of the Standard Model which motivate this study; lepton flavor violation, dark matter, and lithium problems in the standard theory of the big-bang nucleosynthesis. In Chap. 3, we show the parameter region where correct dark matter relic density and light elements abundances including lithiums are obtained in the MSSM. In Chap. 4, we extend the model into the NMSSM and investigate the parameter region where observed light element abundances are obtained as well as the Higgs mass and dark matter relic density. Finally we summarize this study in Chap. 5.

Chapter 2

Phenomenological shortcomings in the Standard Model

As we introduced in the previous chapter, several shortcomings exist in the SM, and so, many types of extended models have been suggested in order to overcome them. In this thesis we focus on the following three points;

(1) light element abundances

(2) relic density of dark matter

(3) the Higgs mass

We investigate allowed parameter region where consistent values of the above quantities with their observational/experimental values are obtained at the same time in an extended model, the NMSSM. This is the main theme of this thesis. In this chapter, we consider the lepton flavor violation, dark matter, and the standard BBN theory as the topics relevant to (1), (2), and (3) before extending the SM.

2.1 Lepton Flavor Violation

Leptons have their lepton flavor number, and the sum of the numbers for initial state particles is equal to that for final state in an interaction, i.e., the lepton flavor number is conserved in the SM. However, lepton flavor violating phenomena have already been observed.

Neutrino ocsillation
   The neutrino oscillations have been searched and observed as lepton flavor violating phenomena. The probability that ν_e converts into ν_μ when the initial state is electron neutrino in the oscillation between two generations is given by

$$P(\nu_e \to \nu_\mu; t) = \sin^2 2\theta \sin^2 \left[1.27 \frac{\Delta m^2 \ (\text{eV})^2}{E \ \text{GeV}} \ L \ \text{km} \right], \qquad (2.1)$$

where θ is the mixing angle between the two states, Δm^2 is the absolute value of the squared mass difference between the two mass eigenstates, E is the energy of the neutrino, and $L(= ct)$ is flight length. The discovery of the neutrino oscillation means that the neutrinos have non-zero masses, since the squared mass difference, Δm^2, must not be zero in order for the probability not to be zero. On the other hand neutrinos are massless in the SM, and hence, the discovery of the neutrino oscillation indicates the existence of the physics beyond the SM.

Table 2.1: Present experimental bounds and future sensitivities of BR and CR by cLFV search experiments. This table is from Ref. [12].

LFV process	Present bound		Future sensitivity	
$BR(\mu \to e\gamma)$	5.7×10^{-13}	[13]	6×10^{-14}	[14]
$BR(\tau \to e\gamma)$	3.3×10^{-8}	[15]	10^{-9}	[16]
$BR(\tau \to \mu\gamma)$	4.4×10^{-8}	[15]	10^{-9}	[16]
$BR(\mu \to 3e)$	1.0×10^{-12}	[17]	$\sim 10^{-16}$	[18]
$BR(\tau \to 3e)$	2.7×10^{-8}	[19]	2.3×10^{-10}	[16]
$BR(\tau \to 3\mu)$	2.1×10^{-8}	[19]	8.2×10^{-10}	[16]
$CR(\mu - e, \mathrm{Ti})$	4.3×10^{-12}	[20]	$\mathcal{O}(10^{-18})$	[21]
$CR(\mu - e, \mathrm{Au})$	7×10^{-13}	[22]		
$CR(\mu - e, \mathrm{Al})$			$\mathcal{O}(10^{-16})$	[23]

Charged Lepton Flavor Violation (cLFV)

Flavor violating phenomena is supposed to exist not only in the neutrino sector but also in the charged lepton sector (charged Lepton Flavor Violation; cLFV). While many search experiments for several cLFV processes have been done, no cLFV signal has been observed. Figure. 2.1 shows the upper limits and future sensitivity of the branching (or conversion) ratios for several violating processes (left column) given by the corresponding search experiments.

We take cLFV into account in the MSSM (Chap. 3) and the NMSSM (Chap. 4) which are models beyond the SM. The cLFV of a new particle, slepton, which appear both in the MSSM and the NMSSM, plays a crucial role in this study.

2.2 Dark Matter

In 1933, F. Zwicky pointed out the existence of dark matter for the first time observing large velocity dispersion of galaxies in the Coma cluster which can not be explained by only gravitation of luminous matter [24]. Since then, many observational evidences of the existence of dark matter have been acquired. One of the most famous and classical evidence is the rotation curve of spiral galaxies [25]. Figure 2.1 shows rotation velocity of NGC3198 as a function of distance from galactic center. The top curve is fitted one to observational results (dots with error bars). The other two curves show those of the galactic disc and halo, respectively. We see that the observed flat velocity distribution can not be reproduced by only luminous component (disc), and the existence of non-luminous component (halo) enable us to reproduce observed distribution. The non-luminous component is considered to be dark matter. Many other evidences of the existence of dark matter have been obtained in these decades, e.g., by observation of the bullet cluster [26], weak [27] and strong [28] lensing, and so on.

The non-luminous nature means that dark matter does not interact with other matters by electromagnetic interaction. Dark matter is known as one of the main components (which occupies about 27% of the total energy) in the present universe from the observation of the Cosmic Microwave Background (CMB) [29]. From the result, dark matter is considered to be stable or at least has a lifetime as long as the age of the Universe. The observational relic density of dark matter is consistent with weak scale mass and interactions.

The particle species which were in thermal equilibrium at the time of decoupling is called as thermal relic (we do not consider non-thermal ones in this thesis). Thermal relic density is different depending on whether the particle species are relativistic at the time of decoupling. The (non-)relativistic species
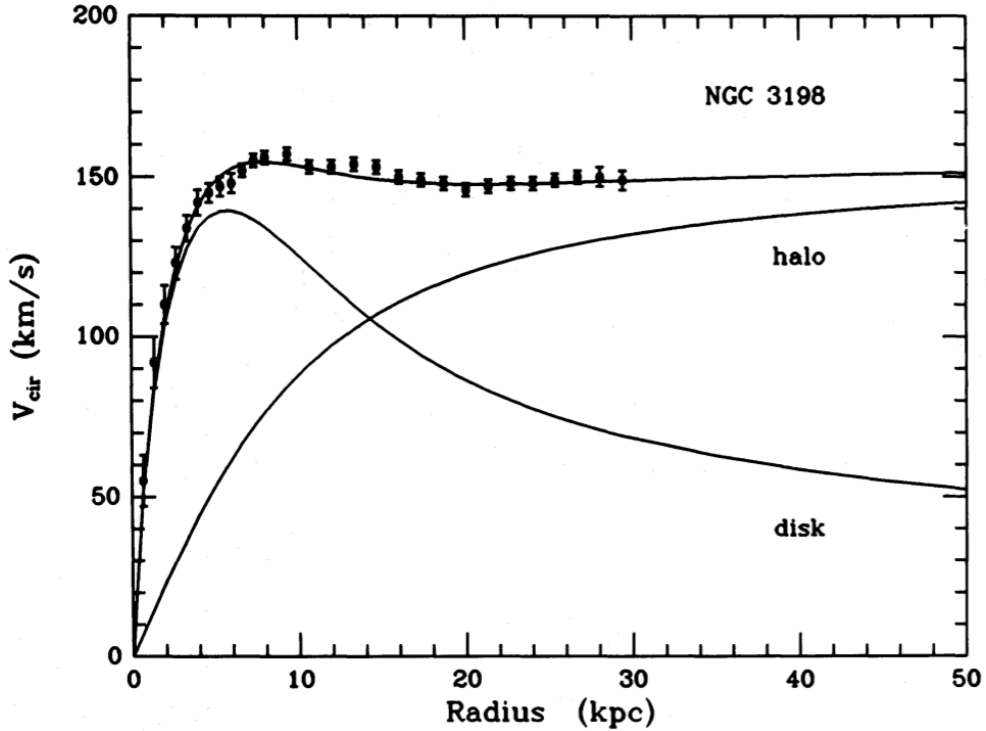
Figure 2.1: Rotation curve of NGC3198, an evidence of the existence of dark matter. The horizontal axis is the distance from galactic center (kpc), and the vertical axis is rotation velocity (km/s). This figure is from Ref. [25].

is called as hot(cold) relics. For example neutrino in the SM is one of the hot relics. However, it is known that if the neutrino is the main component of dark matter, present structure of the Universe can not be reproduced though it is neutral and interacts with other particles by weak interaction. Furthermore, the mass of neutrinos are quite small comparing to those of the other elementary particles. Therefore they can not be the main component of the dark matter particles, and thus no suitable candidate of dark matter particle exist in the SM. In this thesis, we consider Weakly Interacting Massive Particle, WIMP, as dark matter particle. It is one of the cold relics appear in many particle theories beyond the SM, and is one of the most promising candidates with possible mass range from 1 GeV to 100 TeV and interaction cross section with ordinary matter from 10^{-40} to 10^{-50} cm^2.

Many kinds of dark matter search experiments have been carried out since the possibility of direct detection through the interactions between dark matter and ordinary matter discussed in [30]. There are several approaches to probe the interaction of dark matter with ordinary matter as shown in Fig. 2.2.

As an example we show the latest result of direct detection experiment by the LUX Collaboration [32] in Fig. 2.3. The blue line represents 90% confidence level limit (shaded region: $\pm 1\sigma$ error) on upper bound of spin-independent cross section of WIMP-nucleon elastic scattering as a function of WIMP mass.

2.3   Standard Big-Bang Nucleosynthesis and Lithium problems

Primordial nucleosynthesis, which is so-called Big-Bang Nucleosynthesis, is occurred in the cosmic time $t \sim 1\text{-}10^3$s (correspond to the temperature of the Universe $T \sim 1\text{-}0.01$MeV) . Figure 2.4 shows
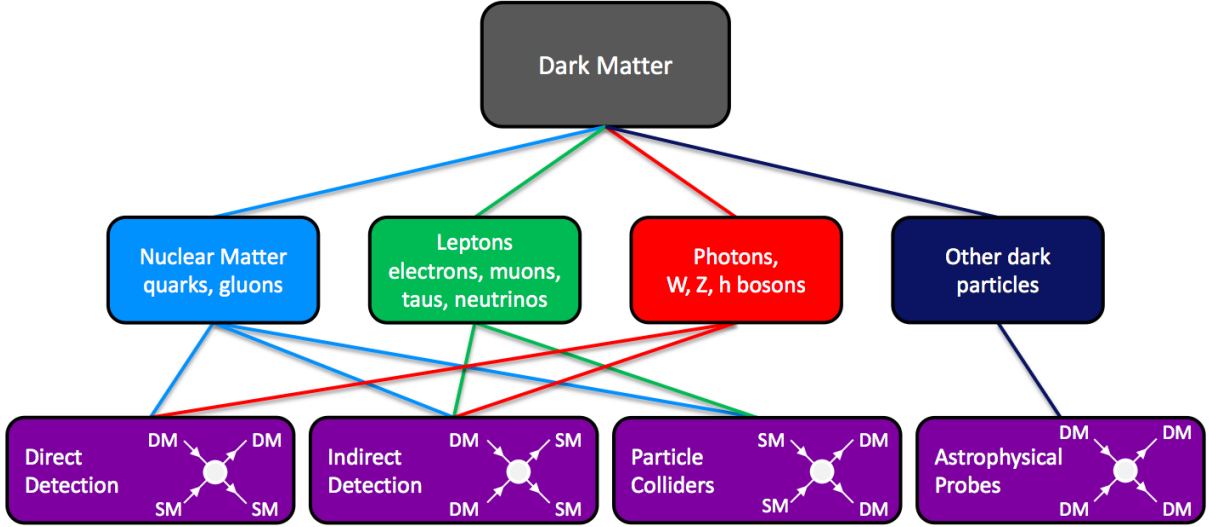
Figure 2.2: Theoretically dark matter may interact with many known particles and other dark matters. These interactions are probed by several different ways. This figure is from Ref. [31].

time and temperature evolution of the number density of light elements by the standard BBN theory [44]. The curves with H and N are number densities of proton and neutron divided by that of baryon, respectively. The curve with Y_p is number density of ^{4}He divided by that of proton. The number densities of the other light elements are also divided by that of proton.

In the standard BBN theory, light element abundances synthesized in the primordial nucleosynthesis are decided by only one parameter, baryon-to-photon ratio η. Its observational value is known from the result by observation of the Cosmic Microwave Background (CMB). Figure 2.5 shows ratios of number densties of ^{4}He, D, ^{3}He, and ^{7}Li to that of H as a function of baryon-to-photon ratio η ($\times 10^{10}$) given by the standard BBN theory (horizontal colored bands). The vertical width of each band means theoretical uncertainty. The narrow vertical band indicates observational value of η from CMB and the wider one indicates the BBN concordance range (both at 95% level). Therefore the crossed region of each horizontal band and vertical band indicates theoretical prediction of each number density ratio. The small (large) boxes show the observational values with $\pm 2\sigma$ statistical (statistical and systematic) error. Thus we see in the top and middle panels that the standard BBN predicts correct number densities for ^{4}He and D. However, for ^{7}Li in the bottom panel, theoretical value is a few times larger than that of observational one. This discrepancy between observation and theory is called as the ^{7}Li problem [46]. Actually such discrepancy exists also for ^{6}Li but in this case theoretical value is smaller than observational one. This is called as the ^{6}Li problem [10].

In particle physics, it is known that the lithium problems could be solved by exotic nuclear reactions with a long-lived charged massive particles called as slepton in the MSSM. In the next chapter, we introduce the MSSM. Then we show the Li problems can be solved in the framework by the exotic BBN reactions with a long-lived slepton. After that in Chap. 4, we finally confirm that they can be solved also in the framework of the NMSSM.
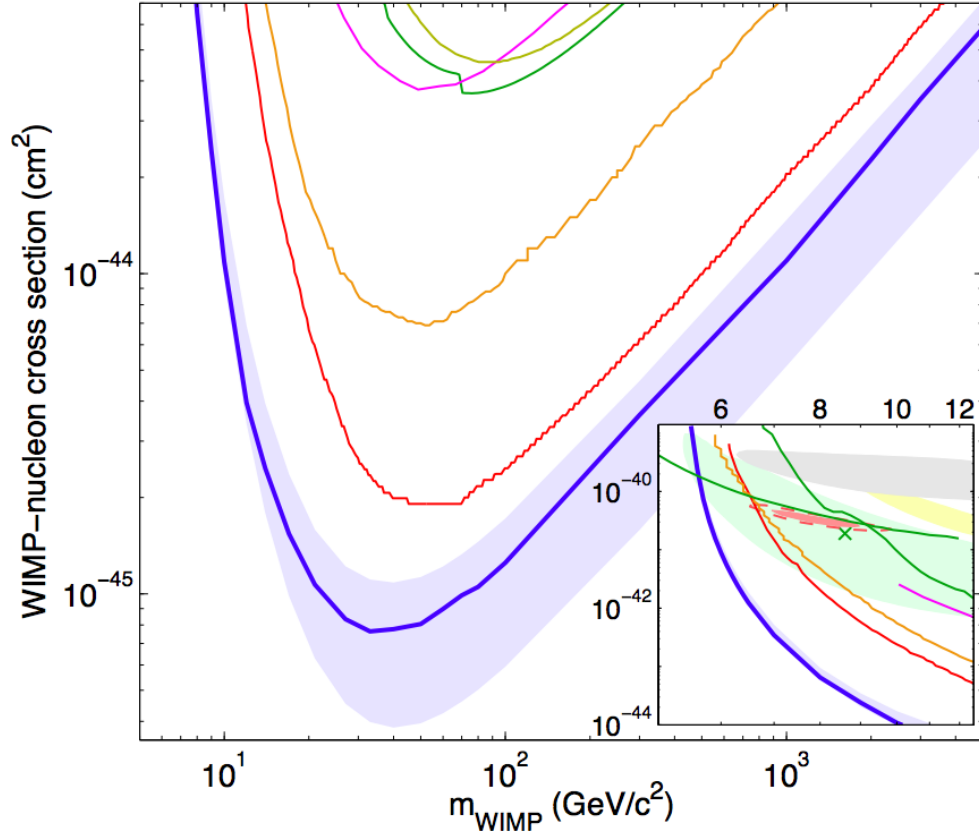
Figure 2.3: First result of LUX experiment. The horizontal axis is a WIMP mass and the vertical axis is spin-independent cross section of WIMP-nucleon elastic scattering. The blue line is 90% confidence level limit and the blue shade is $\pm 1\sigma$ error. The other lines are the results of Edelweiss II [33] (dark yellow), CDMS II [34] (green line), ZEPLIN-III [35] (magenta), and XENON100 100 live-day [36] (orange), and 225 live-day [37] (red). The minimum cross section is $7.6 \times 10^{-46} \mathrm{cm}^2$ which is given at $m_{\mathrm{WIMP}} = 33 \mathrm{GeV}$. In the smaller square, the axies are same as those of larger one. The other results are shown; the regions measured from annual modulation in CoGeNT [38] (light red, shaded), along with exclusion limits from low threshold re-analysis of CDMS II data [39] (upper green line), 95% allowed region from CDMS II silcon detectors [40] (green shaded) and centroid (green x), 90% allowed region from CRESST II [41] (yellow shaded) and DAMA/LIBRA allowed region [42] interpreted by [43] (grey shaded). This figure is from Ref. [32].
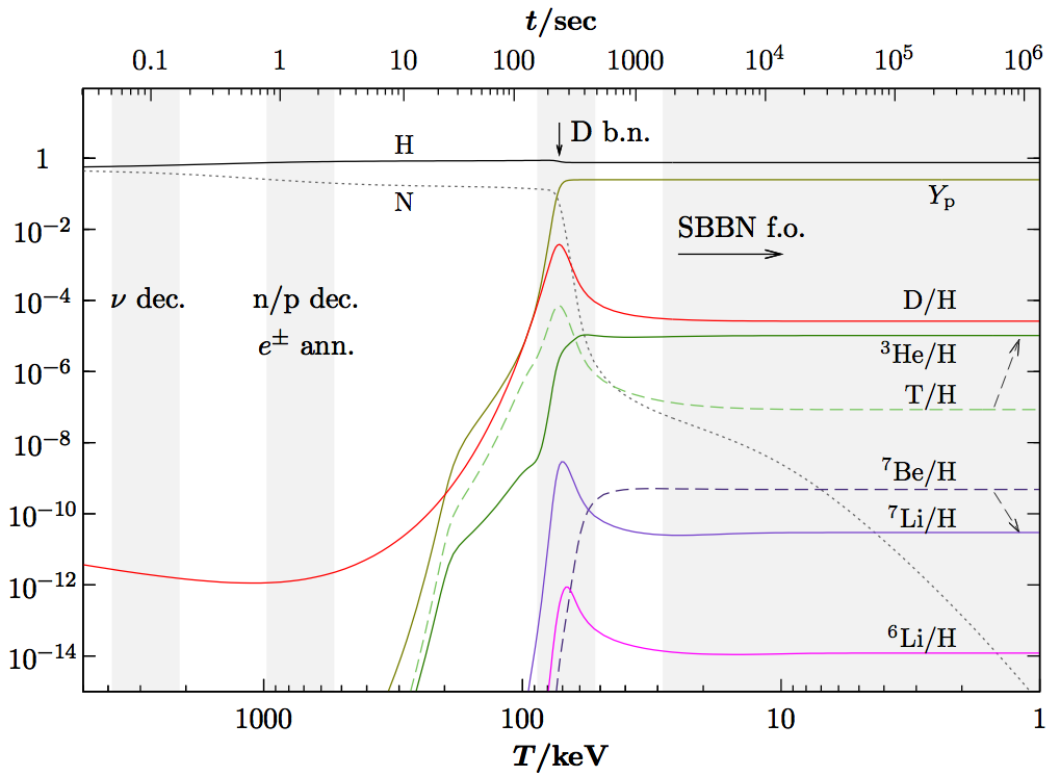
Figure 2.4: Time and temperature evolution of nuclear number density for each element synthesized by the standard BBN. The number density of protons (H) and neutrons (N) are shown as relative ones to that of baryons, n_b. The curve with Y_p is number density of ^{4}He divided by that of proton. The number densities of the other light elements are also divided by that of proton. The light nuclei are synthesized among cosmic time $t \sim 1\text{-}10^3$s and then frozen out. This figure is from Ref. [44].

Figure 2.5: The number density ratio of light elements to H as a function of baryon-to-photon ratio η ($\times 10^{10}$) by the standard BBN (colored bands) and observational values of them (boxes). This figure is from Ref. [45].

Chapter 3

Big-Bang Nucleosynthesis with a long-lived slepton in the MSSM

In this chapter we investigate allowed exotic BBN and flavor mixing of the slepton in the MSSM, before we extend to the NMSSM.

3.1 Neutralino dark matter
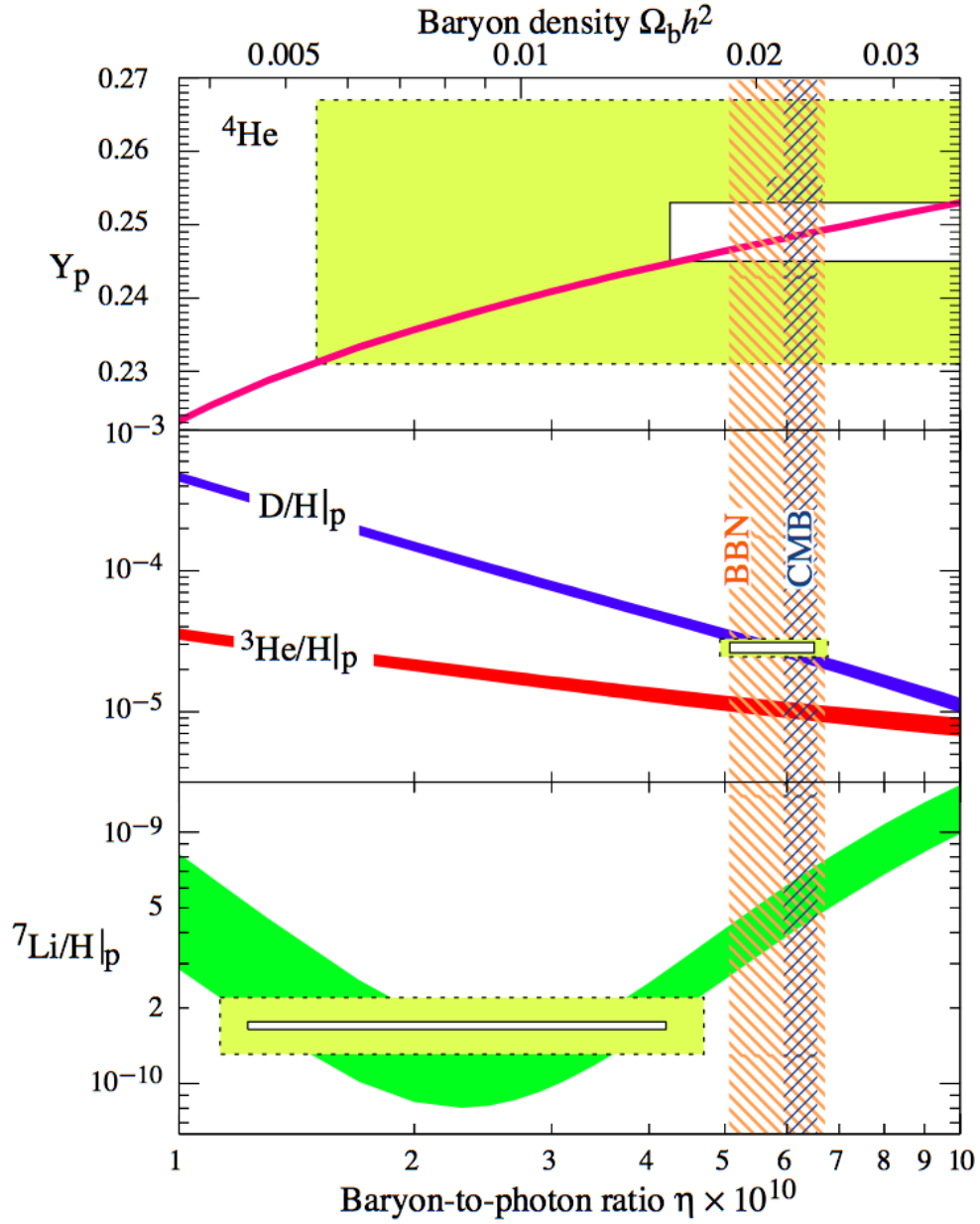
We consider the lightest neutralino as a candidate of dark matter. First of all we introduce R-parity which guarantees stability of the lightest neutralino, and then we introduce neutralinos in the MSSM.

R-parity conservation

We introduce a new symmetry, so-called R-parity. R-parity violating terms leads to rapid decay of proton, and thus we require that R-parity is conserved. Actually, this result in stabilizing the LSP not only prohibiting proton decay as we see in the following. R-parity is defined as follows:

$$P_R = (-1)^{3(B-L)+2s}, \tag{3.1}$$

where B, L, and s are baryon number, lepton number, and spin of each particle, respectively. Quarks and squarks have $B = 1/3$ and $L = 0$, and leptons and sleptons have $B = 0$ and $L = 1$ while the the other particles have $B = L = 0$. As a result of the assignment, for the SM particles and SUSY particles, P_R are assigned as $+1$ and -1, respectively. R-parity conservation means that the product of the values is invariant in an interaction. Therefore the LSP can not decay into an other SUSY particle and a SM particle, i.e., is stable. The LSP can be a candidate of dark matter due to the stability.

Neutralinos

We consider the lightest neutralino, a kind of WIMPs, as the dark matter particle in the MSSM. The MSSM includes four neutralinos, which are linear combinations of bino $\tilde{B}$, wino $\tilde{W}$, and higgsinos $\tilde{H}_d^0$ and $\tilde{H}_u^0$:

$$\tilde{\chi}_i^0 = N_{i\tilde{B}}\tilde{B} + N_{i\tilde{W}}\tilde{W} + N_{i\tilde{H}_d^0}\tilde{H}_d^0 + N_{i\tilde{H}_u^0}\tilde{H}_u^0 \tag{3.2}$$

where i runs from 1 to 4. The mass matrix of the neutralinos is given by the following symmetric

expression in the basis $(\tilde{B}, \tilde{W}, \tilde{H}_d^0, \tilde{H}_u^0)$:

$$
\mathcal{M}_{\tilde{\chi}^0} = \begin{pmatrix} M_1 & 0 & -c_\beta s_W m_Z & s_\beta s_W m_Z & 0 \\ & M_2 & c_\beta c_W m_Z & -s_\beta c_W m_Z & 0 \\ & & 0 & -\mu & -\mu s_\beta \\ & & & 0 & -\mu c_\beta \end{pmatrix}
\tag{3.3}
$$

where $c_\beta = \cos\beta, s_\beta = \sin\beta, c_W = \cos\theta_W$, and $s_W = \sin\theta_W$. Here θ_W is the Weinberg angle. The masses of bino, wino, and higgsinos are denoted by M_1, M_2, and μ, respectively. In this chapter we consider the case where the lightest neutralino is mainly composed of bino ($\tilde{\chi}_1^0 = \tilde{B}$). The observed dark matter relic density can be obtained especially when the NLSP is the lighter stau and the mass difference between the stau and the neutralino, δm, is quite small. At most a few percent of the degeneracy ($\delta m / m_{\tilde{\chi}_1^0} \sim$ a few %) is required. In this case, pair annihilation between the stau and the neutralino, and two staus must be taken into account when we calculate dark matter relic density by solving the Boltzmann equations for total number density of SUSY particles (we will see them later). This mechanism to obtain observed dark matter relic density is called as coannihilation [47, 48]. Small δm can make the lifetime of the stau NLSP much longer compared to that of the other SUSY particles due to phase space suppression. Next we consider the stau and its lifetime, and then generalize it to have flavor mixings.

3.2 Long-lived slepton and its flavor violating decay

The flavor eigenstates of the stau, $\tilde{\tau}_L$ and $\tilde{\tau}_R$, are expressed by linear combinations of the mass eigenstates, $\tilde{\tau}_1$ and $\tilde{\tau}_2$:

$$
\begin{pmatrix} \tilde{\tau}_L \\ \tilde{\tau}_R \end{pmatrix} = \begin{pmatrix} \cos\theta_\tau & \sin\theta_\tau e^{i\gamma_\tau} \\ \sin\theta_\tau & \cos\theta_\tau \end{pmatrix} \begin{pmatrix} \tilde{\tau}_1 \\ \tilde{\tau}_2 \end{pmatrix}
\tag{3.4}
$$

where θ_τ and γ_τ are the left-right mixing angle and the CP-violating phase, respectively. The lighter one of the two mass eigenstates can be the NLSP, and we denote it by $\tilde{\tau}$ in the followings. We now consider the case where the lifetime of the stau is long due to small mass difference between the stau and the neutralino.

The interaction Lagrangian relevant to the decay of the stau is

$$
-\mathcal{L}_{\tilde{\chi}_1^0\text{-}\tau\text{-}\tilde{\tau}} = \tilde{\tau}^* \overline{\tilde{\chi}_1^0}(g_L P_L + g_R P_R)\tau + \text{h.c.},
\tag{3.5}
$$

where the couplings are

$$
g_L = \frac{g_2}{\sqrt{2}} \tan\theta_W \cos\theta_\tau,
\tag{3.6}
$$

$$
g_R = \sqrt{2} g_2 \tan\theta_W \sin\theta_\tau e^{i\gamma_\tau},
\tag{3.7}
$$

and the lightest neutralino is assumed to be purely bino, $\tilde{\chi}_1^0 = \tilde{B}$. We consider the following decay modes of the stau (each mode corresponds to (a), (b), and (c) in Fig. 3.1, respectively):

$$
\tilde{\tau}^\pm \to \tilde{\chi}_1^0 + \tau^\pm
\tag{3.8a}
$$

$$
\tilde{\tau}^\pm \to \tilde{\chi}_1^0 + \nu_\tau + \pi^\pm
\tag{3.8b}
$$

$$
\tilde{\tau}^\pm \to \tilde{\chi}_1^0 + \nu_\tau + l^\pm + \nu_l \quad (l \in e, \mu)
\tag{3.8c}
$$

The top panel in Fig. 3.2 shows the lifetime of the stau as a function of the mass difference δm (red-solid line). We see that the lifetime strongly depends on the mass difference, and it suddenly

becomes long at $\delta m = m_\tau$. This is because the two-body decay Eq. (3.8a) is kinematically forbiden when $\delta m < m_\tau$. Furthermore, as the mass difference becomes smaller, the lifetime gets longer by phase space suppression. In this thesis we focus on the range where $\delta m \lesssim 0.1$ GeV. The lifetime can reach $\mathcal{O}(1)$ s in the range, and then the stau can affect the BBN. In the following sections, we will require such long-lived stau to form bound state with nucleus and modify the BBN through some exotic nuclear reactions so that observed light element abundances are obtained.

We have to note the case where the stau has flavor mixings. Now we consider the state in which the stau is mixed with other flavor eigenstates of smuon and selectron. We call it as slepton and denote as

$$\tilde{l} = \sum_{f=e,\mu,\tau} c_f \tilde{f}, \quad \tilde{f} = \cos\theta_f \tilde{f}_L + \sin\theta_f e^{i\gamma_f} \tilde{f}_R, \tag{3.9}$$

where $\tilde{f}_L$ and $\tilde{f}_R$ are the flavor eigenstates. The coefficients c_e, c_μ, and c_τ are the mixing parameters. These are in ranges from zero to unity and normalized as $c_e^2 + c_\mu^2 + c_\tau^2 = 1$. In this thesis, we assume c_e, c_μ, and c_τ to be real and positive parameters for simplicity. In addition, for the left-right mixings and the CP-violating phase, we assume that $\sin\theta_e = \sin\theta_\mu = \sin\theta_\tau$ and $\gamma_f = 0$ for $f = e, \mu$, and τ. If we consider the slepton with non-zero c_e and/or c_μ, we must take the following flavor violating two-body decays into account when we calculate the lifetime (each mode corresponds to (d) and (e) in Fig. 3.1, respectively):

$$\tilde{l}^\pm \to \tilde{\chi}_1^0 + l^\pm \quad (l \in e, \mu). \tag{3.10}$$

These modes are kinematically allowed for $\delta m > m_e$ and m_μ, respectively. The two-body decay rates are quite large compared to those of three- and four-body decays. Therefore, the flavor violating two-body decays can shorten the lifetime significantly even for tiny flavor mixings. The bottom panel in Fig. 3.2 shows the lifetime of the slepton with/without flavor mixings as a function of the mass difference. The solid line is the lifetime without flavor mixings and the other four lines are those with flavor mixings whose magnitudes are attached along the lines. We see that the lifetime is very sensitive to the magnitude of the flavor mixings. In the followings we call the stau as the slepton even if it does not have flavor mixing.

3.3 Exotic BBN reactions with long-lived slepton

We consider the effects of the long-lived slepton on the BBN. The sleptons survived until the BBN era form bound states with light element nuclei synthesized in that time. Then the bound state effect leads to exotic nuclear reactions which are not included in the standard BBN. The Li problems can be solved by the exotic BBN reactions. We will see the results of the calculation of light element abundances in which these processes are included in the last section of this chapter.

3.3.1 Internal conversion processes

The internal conversion processes are known as a possible solution of the ^{7}Li problem[4, 52]. In these processes, the slepton firstly form bound state with nucleus and then the nucleus is converted into lighter one (Fig. 3.3):

$$(^7\text{Be } \tilde{l}^-) \to {}^7\text{Li} + \tilde{\chi}_1^0 + \nu_l, \tag{3.11a}$$

$$(^7\text{Li } \tilde{l}^-) \to {}^7\text{He} + \tilde{\chi}_1^0 + \nu_l, \tag{3.11b}$$

where $(X \tilde{l}^-)$ denotes bound state between a nucleus X and the slepton. The timescale of the bound state formation is $\mathcal{O}(10^3)$ s and that of the conversion is typically small compared to the formation
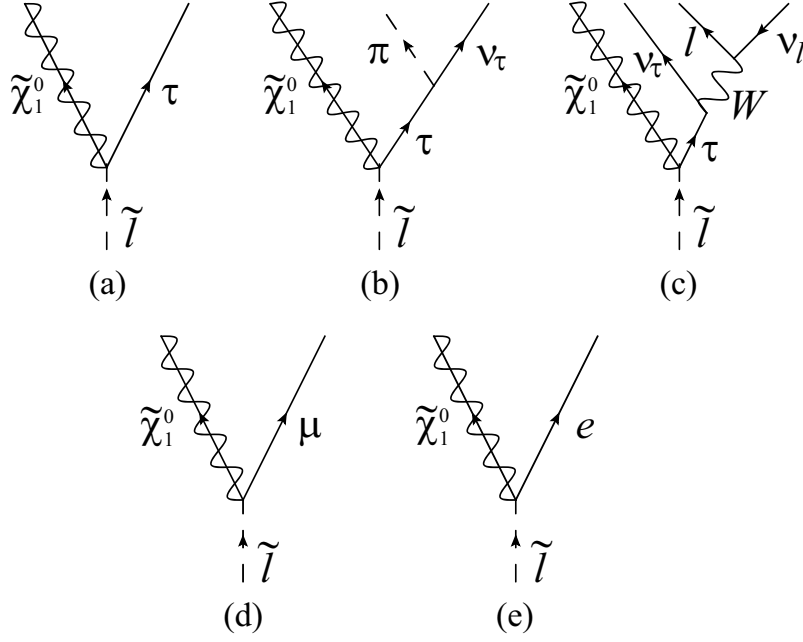
Figure 3.1: Decay modes of the slepton. Flavor conserving processes (a) $\tilde{l} \to \tilde{\chi}_1^0 + \tau$, (b) $\tilde{l} \to \tilde{\chi}_1^0 + \nu_\tau + \pi$, and (c) $\tilde{l} \to \tilde{\chi}_1^0 + \nu_\tau + l + \nu_l$, and flavor violating processes (d) $\tilde{l} \to \tilde{\chi}_1^0 + \mu$ and (e) $\tilde{l} \to \tilde{\chi}_1^0 + e$ are shown.

timescale. The abundance of ^{7}Li observed in the present Universe is sum of the abundances of ^{7}Li and ^{7}Be produced in the BBN era, since ^{7}Be is unstable and decay into ^{7}Li by electron capture after the BBN era.

The internal conversion processes (3.11) reduce ^{7}Li and ^{7}Be abundances, and thus the ^{7}Li problem could be solved. Without the bound state formation, there exists similar processes which reduce ^{7}Be and ^{7}Li by the interaction between a nucleus and a real pion arisen from the decay of free slepton:

$$\tilde{l}^{\pm} \to \tilde{\chi}_1^0 + \nu_l + \pi^{\pm} \tag{3.12}$$

$$\pi^+ + {}^7\text{Li} \to {}^7\text{Be} \tag{3.13}$$

$$\pi^- + {}^7\text{Be} \to {}^7\text{Li} \tag{3.14}$$

$$\pi^- + {}^7\text{Li} \to {}^7\text{He} \tag{3.15}$$

However, the internal conversion processes are more effective than these processes, since the overlap of wave functions between the nucleus and the slepton is large. Furthermore, the distance between the nucleus and the slepton is short, and virtual exchange of the hadronic current is possible even for $\delta m < m_{\pi^{\pm}}$.

3.3.2 Slepton-catalyzed fusion process

The catalyzed fusion process is known as a possible solution to the ^{6}Li problem [54, 55]. In this process the slepton forms bound state with ^{4}He, and the ^{4}He is catalyzed by the slepton with D to produce ^{6}Li:

$$({}^4\text{He}\ \tilde{l}^-) + \text{D} \to {}^6\text{Li} + \tilde{l}^-. \tag{3.16}$$

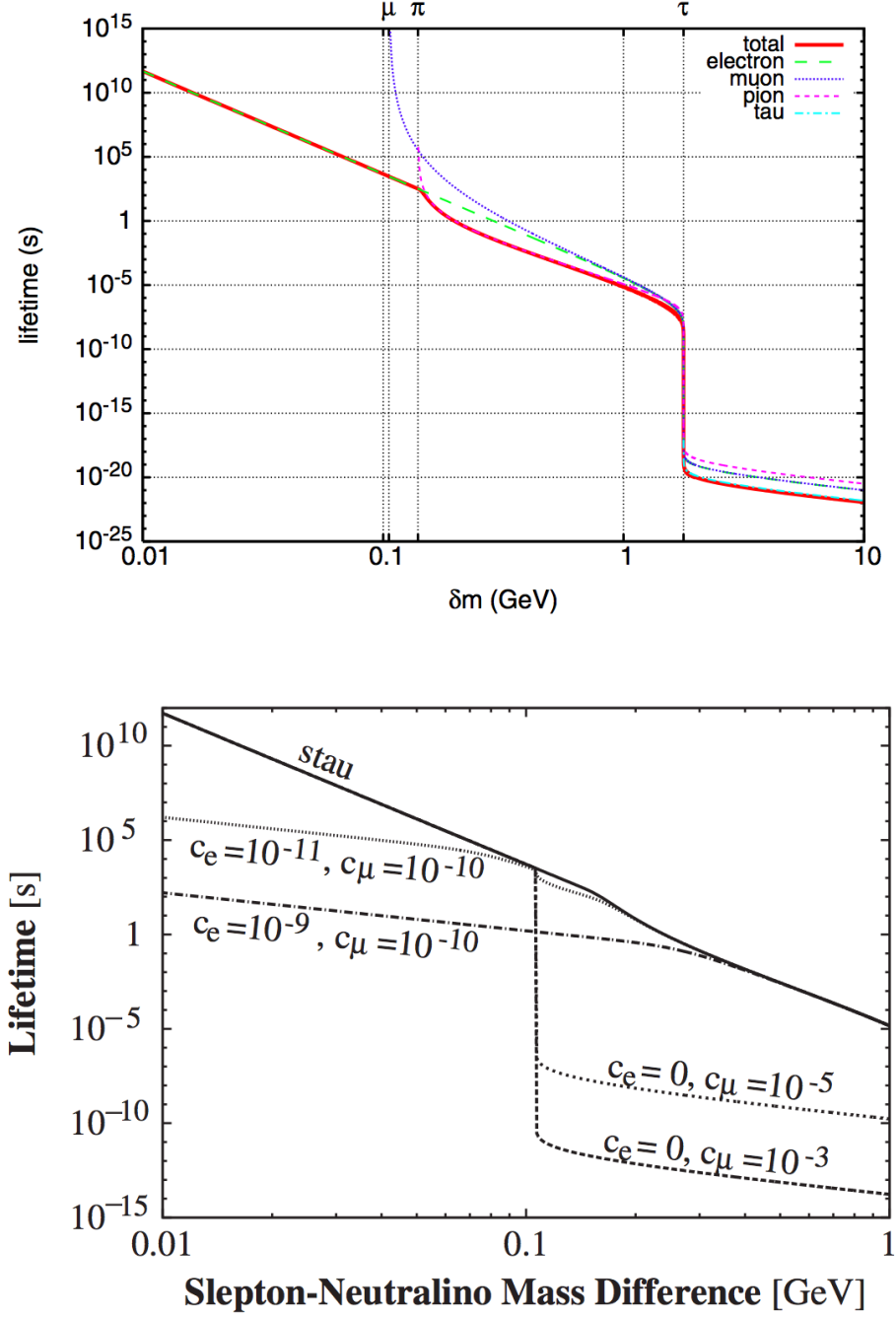Figure 3.2: The lifetime of the stau (red-solid line in the top panel) and the slepton (dotted lines in the bottom panel) as a function of the mass difference. Parameters are $m_{\tilde{\chi}^0} = 300\text{GeV}$, $\theta_\tau = \pi/3$, and $\gamma_\tau = 0$ in the top panel, and $m_{\tilde{\chi}^0} = 350\text{GeV}$, $\sin\theta_\tau = 0.8$, and $\gamma_\tau = 0$ in the bottom panel. The top panel is from Ref. [49].
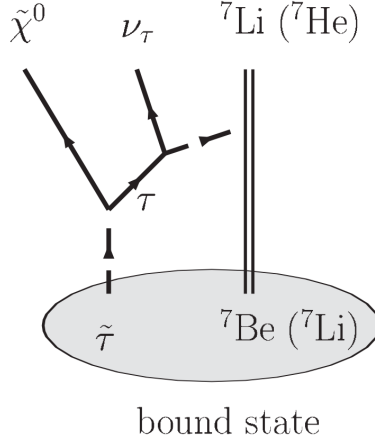
Figure 3.3: Internal conversion processes. This figure is from Ref. [4].

The cross section of this process is much larger than that of another production process for ^{6}Li in the standard BBN,

$$^4\text{He} + d \rightarrow {}^6\text{Li} + \gamma. \tag{3.17}$$

The timescale of the bound state formation between ^{4}He and the slepton is $\mathcal{O}(10^4)$s, which is longer than that of $(^7\text{Be}\ \tilde{l}^-)$ and $(^7\text{Li}\ \tilde{l}^-)$ formations in the internal conversion processes, $\mathcal{O}(10^3)$s. Therefore ^{6}Li can be overproduced when the lifetime of the slepton is too long, while the lifetime must be at least longer than the timescale of the internal conversion in order to solve the ^{7}Li problem. However, sufficient longevity of the slepton could lead to produce sufficient amount of ^{6}Li and solve the ^{6}Li problem.
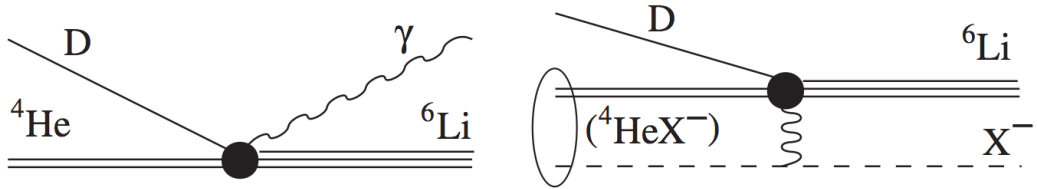
Figure 3.4: Production processes for ^{6}Li in the standard BBN (left) and catalyzed BBN (right). This figure is from Ref. [54].

3.3.3 ^{4}He spallation processes

We must include the ^{4}He spallation processes due to bound state effect which have the bound state $(^4\text{He}\ \tilde{l}^-)$ as well as the catalyzed fusion process. In these processes ^{4}He is destroyed into triton (T), deuteron (D), and neutron (n) (corresponding diagrams are shown in Fig. 3.5) :

$$(^4\text{He}\ \tilde{l}^-) \rightarrow \tilde{\chi}_1^0 + \nu_l + \text{T} + n, \tag{3.18a}$$

$$(^4\text{He}\ \tilde{l}^-) \rightarrow \tilde{\chi}_1^0 + \nu_l + \text{D} + 2n, \tag{3.18b}$$

$$(^4\text{He}\ \tilde{l}^-) \rightarrow \tilde{\chi}_1^0 + \nu_l + p + 3n. \tag{3.18c}$$

The timescale of these processes can be shorter than that of the catalyzed fusion process (3.16), since these processes proceed only by the bound state effects while the catalyzed fusion process needs external deuteron. We note that these spallation processes could arise overproduction of T and D, and modify the standard BBN prediction of the abundance of d and ^{3}He. Figure 3.6 shows the lifetime of the slepton (curve with "stau lifetime") and timescales of the ^{4}He spallation processes (curves with "tn" for (3.18a), "dnn" for (3.18b), and "pnnn" for (3.18c)) and catalyzed fusion process at $T = 30$ keV (which corresponds to the cosmic time of 10^3 s) as functions of the mass difference between the slepton and the neutralino. The parameters used in the calculation are $m_{\tilde{\tau}} = 350$ GeV, $\sin\theta_\tau = 0.8$, and $\gamma_\tau = 0$. Overproduction of t and d could arise for $\delta m \gtrsim 0.026$ GeV where the ^{4}He spallation processes are open.
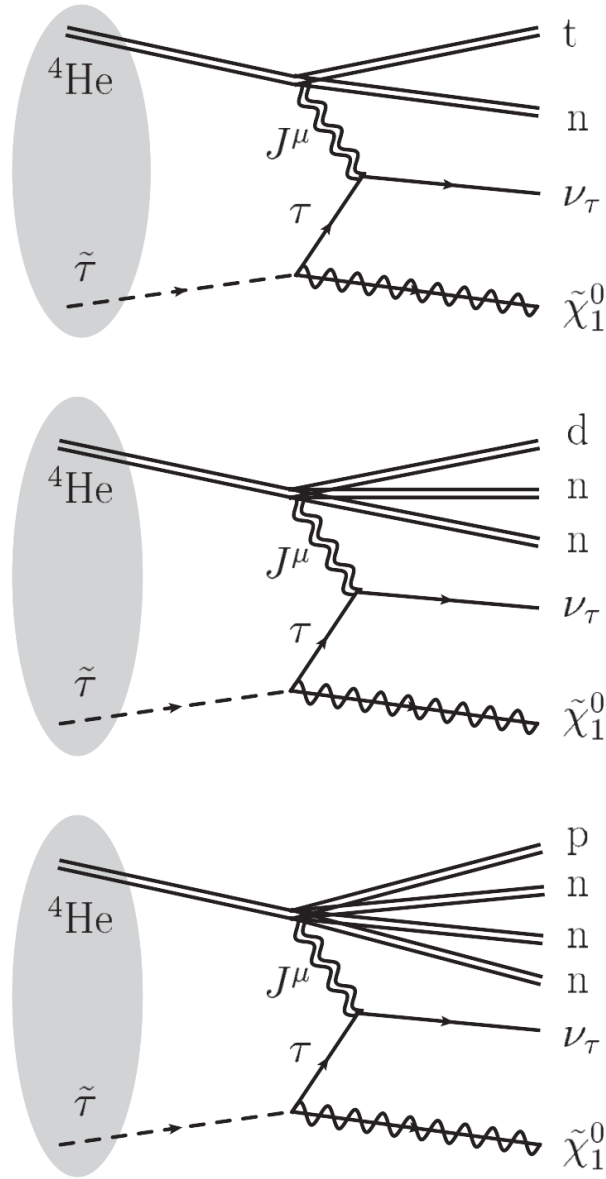

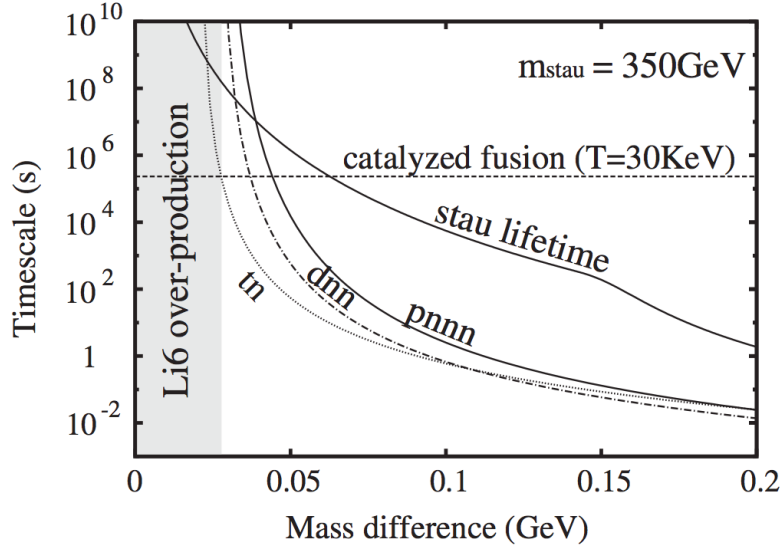Figure 3.5: Diagrams of the ^{4}He spallation processes. This figure is from Ref. [7].

Figure 3.6: Comparison of the timescales among the ^{4}He spallation processes (3.18a) (solid curve), (3.18b) (dash-dotted curve), and (3.18c) (dotted curve), and the catalyzed fusion (3.16) , for $T = 30$K (horizontal dotted line). This figure is from Ref. [7].

3.4   Number density of the long-lived slepton

As we discuss in the previous section, longevity of the slepton is quite important for solving lithium problems by the exotic BBN reactions. Predicted light element abundances by the exotic BBN depend also on the number density of the slepton at the BBN era. Indeed, the number density is quite sensitive to the flavor mixing parameters of the slepton c_e and c_μ, in the mass-degenerate scenario. Therefore, the number density has to be accurately calculated as a function of the mixing parameters in order to constrain the flavor mixing. In the end of this chapter, we show the allowed parameter region for the mixing parameters constrained from our successful exotic BBN.

Calculation of the number density evolution of the slepton has two steps. For the first step, we calculate total number density of the SUSY particles at the time of their chemical decoupling. The number density of the slepton continues to evolve by scattering among the slepton and cosmic thermal background till the temperature $T \simeq \delta m$ even after the chemical decoupling. In addition the number density of the slepton is reduced by its own natural decay. Then, as the second step, the evolution of the number density is acquired by solving relevant Boltzmann equations implementing the scatterings and the decays. We first explain the calculation of the number density, and then present a set of Boltzmann equations for the calculation.

3.4.1   Total number density of SUSY particles

Firstly we calculate the total number density of SUSY particles. All SUSY particles eventually decay into LSP, the lightest neutralino in our case, due to R-parity conservation. Thus the total number density of SUSY particles,

$$N = \sum_i n_i \tag{3.19}$$

where i denotes all SUSY particle species, is equal to the relic density of dark matter in the present Universe. Calculation of the relic density of the neutralino dark matter in the stau-neutralino coannihilation scenario has been developed so far [47, 48]. Assuming the flavor mixing is not so large and the

main component of the slepton is stau, $c_\tau \simeq 1$, the calculation method is applicable to our situation. That is, cross sections of the coannihilation processes are firstly calculated, and then we solve the Boltzmann equations for the total number density of SUSY particles.

After the chemical decoupling, the total number density of SUSY particles remains the value at that time. This value does not have correlation with the flavor mixing. This value is required as the initial condition for calculating the slepton number densety as a function of the flavor mixing.

3.4.2 Ratio of the number density between the slepton to the neutralino

Even after the chemical decoupling, the number density ratio of the slepton to the neutralino continues to evolve via exchange processes,

$$\tilde{l}^\pm + \gamma \leftrightarrow \tilde{\chi}_1^0 + \mu^\pm, \ \tilde{l}^\pm + \gamma \leftrightarrow \tilde{\chi}_1^0 + \tau^\pm, \ \tilde{\chi}_1^0 + \gamma \leftrightarrow \tilde{l}^\pm + l^\mp \quad (l \in e, \mu). \tag{3.20}$$

Contribution of the other exchange processes, e.g., $\tilde{l} + e + \bar{\nu}_e \leftrightarrow \tilde{\chi}_1^0 + \nu_\tau$, $\tilde{l} + \nu_\tau \leftrightarrow \tilde{\chi}_1^0 + \mu + \bar{\nu}_\mu$, and so on, are negligible due to weak interactions. Note here that $\tilde{l}^\pm + \gamma \leftrightarrow \tilde{\chi}_1^0 + e^\pm$ must not be included. The decay mode $\tilde{l} \to \tilde{\chi}_1^0 + e$ is open when $c_e \neq 0$, so the exchange process contributes as a radiative correction to the decay and inverse decay modes. We thus do not include the exchange process to (3.20) in order to avoid double counting. Another exchange process $\tilde{l}^\pm + \gamma \leftrightarrow \tilde{\chi}_1^0 + \mu^\pm$ is also excluded when $\tilde{l} \to \tilde{\chi}_1^0 + \mu$ by the same reason.

These exchange processes (3.20) keep the slepton and the neutralino in kinematical equilibrium. The number density ratio of the slepton to the neutralino maintain the Boltzmann distribution due to this kinematical equilibrium. The number density of the slepton for a fixed δm therefore decreases as the temperature of the Universe decreases;

$$n_{\tilde{l}} = \frac{n_{\tilde{l}}}{n_{\tilde{\chi}_1^0}} \frac{n_{\tilde{\chi}_1^0}}{n_{\tilde{\chi}_1^0} + n_{\tilde{l}^+} + n_{\tilde{l}^-}} N = e^{-\delta m/T} \frac{N}{2(1 + e^{-\delta m/T})}, \tag{3.21}$$

where T is the temperature, and N is a sum of the densities of the slepton and the neutralino that are obtained in the first step (see Sec. 3.4.1). The kinematical equilibrium is broken when the Hubble expansion rate overwhelms the reaction rates of the exchange processes. Hence it is important to know when the Hubble expansion rate overwhelms the reaction rate. We numerically solve a set of Boltzmann equations to obtain accurate resultant number density of the slepton.

3.4.3 Boltzmann equations for relic number density of the slepton

The evolutions of the number densities of the negatively charged slepton $n_{\tilde{l}^-}$, the positively charged slepton $n_{\tilde{l}^+}$, and the neutralino $n_{\tilde{\chi}_1^0}$ are described by the following set of Boltzmann equations:

$$\frac{dn_{\tilde{l}^-}}{dt} + 3H n_{\tilde{l}^-} = -\sum_{i,X,Y} \left[\langle \sigma' v \rangle_{iY} n_{\tilde{l}^-} n_X^{eq} - \langle \sigma' v \rangle_{\tilde{l}^- X} n_i n_Y^{eq} \right]$$
$$- \sum_{X,Y,...} \left[\langle \Gamma \rangle_{\tilde{\chi}_1^0 XY...} n_{\tilde{l}^-} - \langle \Gamma \rangle_{\tilde{l}^-} n_{\tilde{\chi}_1^0}^{eq} n_X^{eq} n_Y^{eq}... \right], \tag{3.22}$$

$$\frac{dn_{\tilde{l}^+}}{dt} + 3H n_{\tilde{l}^+} = -\sum_{i,X,Y} \left[\langle \sigma' v \rangle_{iY} n_{\tilde{l}^+} n_X^{eq} - \langle \sigma' v \rangle_{\tilde{l}^+ X} n_i n_Y^{eq} \right]$$
$$- \sum_{X,Y,...} \left[\langle \Gamma \rangle_{\tilde{\chi} XY...} n_{\tilde{l}^+} - \langle \Gamma \rangle_{\tilde{l}^+} n_{\tilde{\chi}_1^0}^{eq} n_X^{eq} n_Y^{eq}... \right], \tag{3.23}$$

$$\frac{dn_{\tilde{\chi}_1^0}}{dt} + 3Hn_{\tilde{\chi}_1^0} = - \sum_{i,X,Y} \left[\langle \sigma'v \rangle_{iY} n_{\tilde{\chi}} n_X^{eq} - \langle \sigma'v \rangle_{\tilde{\chi}X} n_i n_Y^{eq} \right]$$
$$- \sum_{i,X,Y,...} \left[\langle \Gamma \rangle_i n_{\tilde{\chi}_1^0} n_X^{eq} n_Y^{eq}... - \langle \Gamma \rangle_{\tilde{\chi}_1^0 XY...} n_i \right], \qquad (3.24)$$

where t is time and H is the Hubble parameter. In the right-hand side of each equation, $\langle \sigma'v \rangle$ is the thermal averaged cross sections of the exchange processes in Eq. (3.20), and $\langle \Gamma \rangle$ is the thermal averaged decay rate (or inverse decay rate). The index i represents relevant SUSY particles, and indices X and Y represent the SM particles, respectively. Subscripts to both $\langle \sigma'v \rangle$ and $\langle \Gamma \rangle$ denote the final states of each processes. In the equations, we assumed that the relevant SM particles are thermalized.

In the presence of the flavor mixing, $\langle \sigma'v \rangle$ and $\langle \Gamma \rangle$ depend on the mixing parameters. Solving a set of the Boltzmann equations above, the number density of the slepton at the BBN era is obtained as a function of the mixing parameters. Then we perform the BBN calculations and predict light element abundances by using obtained number density. Comparing them with observational values, we can constrain or predict the mixing parameters.

3.5 Analytical constraint on the flavor mixing

We give analytical estimations for bounds on the mixing parameters c_e and c_μ in Eq. (3.9). The mixing parameters are constrained from above by two requirements. The first one is the sufficient longevity of the slepton, and the second one is the sufficient number density of the slepton at the moment of decoupling from the exchange processes. For the first requirement, the lifetime of the slepton must be longer than $\mathcal{O}(10^3)$ s to solve the ^{7}Li problem through the internal conversion processes as we discussed in Sec. 3.2. The lifetime varies by a few order of magnitudes as δm and $c_{e,\mu}$ vary. Due to the kinematical thresholds for the decays, the dependence on both c_e and c_μ is different for $\delta m > m_\mu$ or $\delta m < m_\mu$ as in the bottom panel of Fig. 3.2. Therefore, the lifetime should be studied in each δm region to obtain bounds on the mixing parameters.

To obtain the bounds analytically, we consider two cases in which either $c_e = 0$ or $c_\mu = 0$ for simplicity. For the case where $c_\mu = 0$, the slepton decays into an electron and the lightest neutralino (2-body decay). Then the lifetime of the slepton is approximately given by

$$\tau_{\tilde{l}}(\tilde{l} \to \tilde{\chi}_1^0 + e) \simeq \frac{8\pi}{g^2 \tan^2 \theta_W} \frac{m_{\tilde{l}}}{(\delta m)^2} \frac{1}{\cos^2 \theta_e + 4\sin^2 \theta_e} \frac{1}{c_e^2}, \qquad (3.25)$$

where $m_{\tilde{l}}$ is the mass of the slepton. Inserting $\cos \theta_e = 0.6$ for a reference value, the lifetime is

$$\tau_{\tilde{l}} \left(\tilde{l} \to \tilde{\chi}_1^0 + e \right) \simeq 1.34 \times 10^3 \left[\frac{m_{\tilde{l}}}{300 \text{GeV}} \right] \left[\frac{0.1 \text{GeV}}{\delta m} \right]^2 \left[\frac{4 - 3(0.6)^2}{4 - 3\cos^2 \theta_e} \right] \left[\frac{10^{-10.5}}{c_e} \right]^2 \text{s}.$$

Requiring $\tau_{\tilde{l}} \geq \mathcal{O}(10^3 \text{s})$, we obtain the bound on the selectron component, $c_e \lesssim 3.2 \times 10^{-11}$ for $\delta m = 0.1$ GeV and $m_{\tilde{l}} = 300$ GeV. Similarly, for the case where $c_e = 0$, the lifetime is approximately represented by

$$\tau_{\tilde{l}} \left(\tilde{l} \to \tilde{\chi}_1^0 + \mu \right) \simeq 10^3 \left[\frac{10^{-10.5}}{c_\mu} \right]^2 \left[\frac{0.12 \text{GeV}}{\delta m} \right]^2 \left[\frac{m_{\tilde{l}}}{300 \text{GeV}} \right] \left(1 - \frac{25}{36} \left[\frac{0.12 \text{GeV}}{\delta m} \right]^2 \right)^{-1/2} \text{s}, \qquad (3.26)$$

where $\cos \theta_\mu = 0.6$. Then the upper bound on c_μ is obtained as 3.2×10^{-11} for $\delta m = 0.1$ GeV and $m_{\tilde{l}} = 300$ GeV.

We can derive another upper bounds on the mixing parameters from the second requirement that the number density should be sufficient at the decoupling time from the exchange processes to destroy the ^{7}Li and ^{7}Be nuclei. Again in the case where $c_\mu = 0$, the relevant exchange processes are $\tilde{l} + e \leftrightarrow \tilde{\chi}_1^0 + \gamma$ and $\tilde{l} + \tau \leftrightarrow \tilde{\chi}_1^0 + \gamma$. The former process keeps working even after the freeze out of the latter process. This is because densities of electron and photon are still quite large in thermal bath for $T \lesssim m_\tau$. Therefore the slepton number density continues to decrease as explained in the previous section. The reaction rate of the former process is proportional to c_e^2. Hence the larger the mixing is, the more the number density decreases. The reaction rate of $\tilde{l} + e \leftrightarrow \tilde{\chi}_1^0 + \gamma$ must be suppressed to ensure a sufficient number density of the slepton. The bound on c_e is estimated by comparing this reaction rate with that of processes with tau.

In the absence of the flavor mixing or pure stau case, freeze out of the exchange processes ($\tilde{l}^\pm + \gamma \leftrightarrow \tilde{\chi}_1^0 + \tau^\pm$ and $\tilde{\chi}_1^0 + \gamma \leftrightarrow \tilde{l}^\pm + \tau^\mp$) occurs at $T \simeq 70$MeV, and is almost independent of both δm and $m_{\tilde{l}}$ [6]. Then the number density of the slepton manages to be a sufficient amount. This fact suggests that the reaction rate of $\tilde{l}e \leftrightarrow \tilde{\chi}_1^0 \gamma$ must be smaller than that of the processes in the absence of the flavor mixing at $T = 70$ MeV. Parameterizing the cross section of this process as $\langle \sigma' v \rangle_e = c_e^2 \langle \sigma' v \rangle_\tau$, the ratio of these reaction rates at $T = 70$ MeV is given by

$$\frac{\langle \sigma' v \rangle_e Y_{\tilde{l}} Y_e}{\langle \sigma' v \rangle_\tau Y_{\tilde{l}} Y_\tau} \simeq (1.08 \times 10^9) c_e^2, \tag{3.27}$$

where $Y_{\tilde{l}}$ and $Y_{e,\tau}$ are the yield values of the slepton and electron/tau, respectively. The mixing parameter c_e is therefore required to be $\lesssim 3 \times 10^{-5}$. For the case where $c_e = 0$, the reaction rate of the process $\tilde{l} + \mu \leftrightarrow \tilde{\chi}_1^0 + \gamma$ is compared with that without the mixing. Parameterizing the cross section of the process as $\langle \sigma' v \rangle_\mu = c_\mu^2 \langle \sigma' v \rangle_\tau$, the ratio of the reaction rates is given by

$$\frac{\langle \sigma' v \rangle_\mu Y_{\tilde{l}} Y_\mu}{\langle \sigma' v \rangle_\tau Y_{\tilde{l}} Y_\tau} \simeq (9.93 \times 10^7) c_\mu^2, \tag{3.28}$$

at temperature $T = 70$ MeV. From Eq. (3.28), c_μ must be smaller than 10^{-4}.

As we will see later, we can constrain c_e from below by the relic abundance of light elements. Thus we will get an allowed region for c_e.

3.6 Results of the BBN with a long-lived slepton in the MSSM

Now we search for an allowed region of the slepton mixing parameters and show that light element abundances are obtained correctly as well as dark matter relic density in the MSSM. First we see that the upper bounds on c_e and c_μ obtained in the previous section are in a good agreement with numerical analysis. Then we numerically compute reaction networks of light elements including the exotic nuclear reactions we saw in Sec. 3.3, and find parameter regions as a function of δm allowed by the observational light element abundances in case with/without the flavor mixing. After that we finally show the allowed region on c_e–c_μ plane where the ^{7}Li and/or ^{6}Li problems can be solved.

3.6.1 Constraint on slepton flavor mixing

First we show bounds on the mixing parameter c_μ for $\delta m < m_\mu$. We fix $Y_{\tilde{l}} = 2 \times 10^{-13}$ for the sufficient number density to solve the ^{7}Li problem based on Ref. [4].

Figure 3.7 shows the temperature evolution of the yield values of the slepton for each values of c_μ attached along the curve. From top to bottom panels, the mass differences are taken to be $\delta m = 20$ MeV, 60 MeV, and 100 MeV, respectively. The curves tagged by "stau" represent the yield values without flavor mixing, and the curves tagged by "Equilibrium" are the yield values of

the slepton in kinetic equilibrium. In shaded region, number density of the slepton is insufficient to solve the ^{7}Li problem. In each panel, we took $c_e = 0$, because bound on c_e is $c_e \lesssim 10^{-10}$ and hence contributions of c_e are negligible when the exchange processes are still working. As is expected, larger value of c_μ keeps yield values of the slepton to be in kinetic equilibrium and leads smaller number densities of the slepton.

The bound on $c_\mu \lesssim 5 \times 10^{-5}$ for $\delta m = 20$ MeV (Fig. 3.7(a)) accurately reproduces our estimation in the previous section. For larger δm, the bounds on c_μ become more stringent; $c_\mu \lesssim 2 \times 10^{-6}$ for $\delta m = 60$ MeV (Fig. 3.7(b)), and $c_\mu \lesssim 2 \times 10^{-7}$ for $\delta m = 100$ MeV (Fig. 3.7(c)). This is understood as follows. The cross sections for the processes (3.20) are not so dependent on δm for $\delta m < m_\mu$. They are more dependent on the muon number density and hence the temperature. It means that the decoupling temperature of these processes are almost same as long as c_μ is same. Then these processes must decouple earlier for larger mass difference to have a sufficient yield. See Eq. (3.21). Thus less intergenarational mixing is allowed for larger mass difference.

In the case of $\delta m \geq m_\mu$, more stringent bounds on c_μ are derived from the requirement on lifetimes of the slepton. To solve the ^{7}Li problem, sufficient amount of the bound states of the slepton and ^{7}Be (^{7}Li) have to be formed. This formation requires the lifetime of the slepton to be at least 1000s, preferably 2000s (see Fig. 1 in Ref. [5]). Fig. 3.8 shows bounds both on c_μ and c_e for $\delta m = 106$ MeV, 114 MeV, and 122 MeV, respectively. Values near each curves are the lifetime of the slepton. In shaded region, the lifetime of the slepton is shorter than 1000 s, and hence the parameters in this region are excluded. In left-side and down-side region in each panel, 4-body decay process is dominant because the mixing parameters are so small. This result is consistent with the result in Fig. 3.2. The upper bounds on c_μ obtained here are $c_\mu \lesssim 2 \times 10^{-10}$ for $\delta m = 106$ MeV, which is just above the threshold of the decay of the slepton into a muon, and $c_\mu \lesssim 6 \times 10^{-11}$ for $\delta m = 114$ MeV, and $c_\mu \lesssim 2 \times 10^{-11}$ for $\delta m = 122$ MeV.
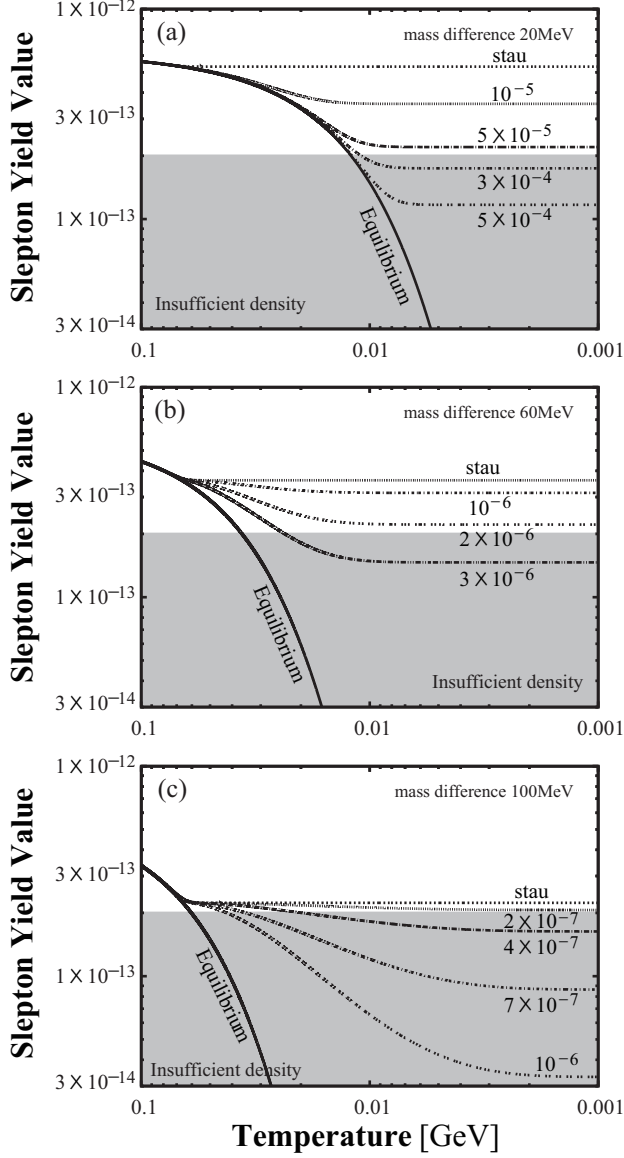
Figure 3.7: Evolution of slepton yield values $Y_{\tilde{l}}$ for each smuon component c_μ, which values are attached on corresponding curve. Curves tagged by "stau" are yield values of pure stau, and curves tagged by "Equilibrium" are yield values of the slepton in kinetic equilibrium. In shaded region, number density of the slepton is insufficient for solving the ^{7}Li problem.
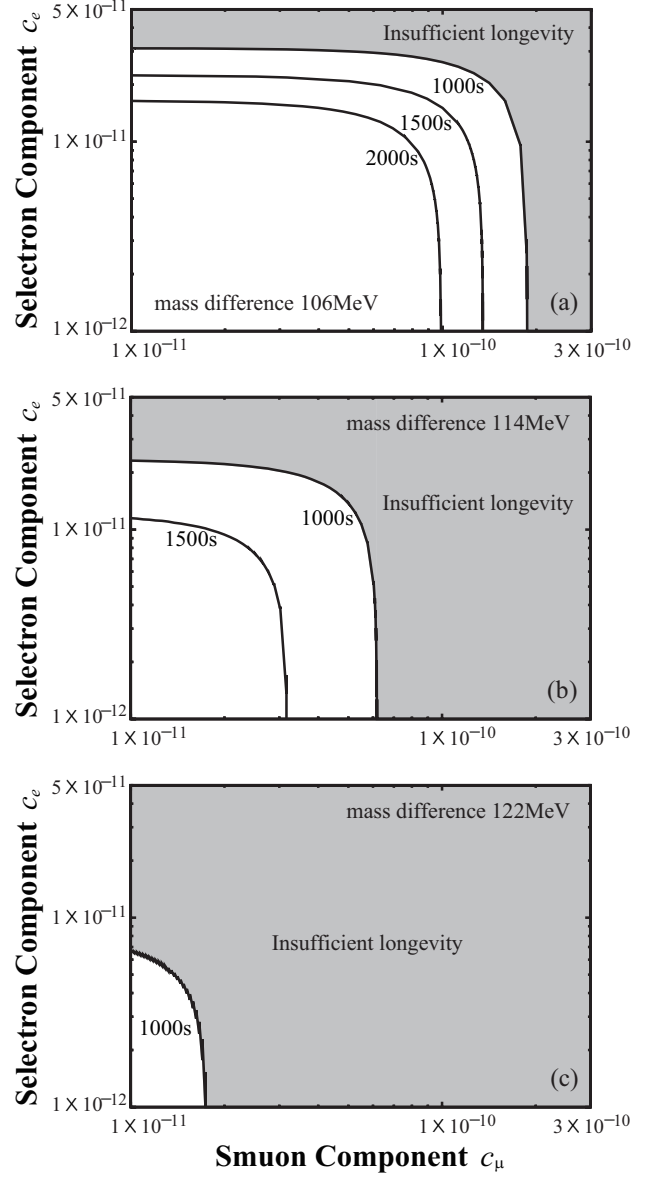
Figure 3.8: Bounds both on c_μ and c_e for $\delta m \geq m_\mu$. Shaded region is disfavored in light of solving the ^{7}Li problem, wherein the slepton decays before forming a bound state with ^{7}Be and ^{7}Li.

3.6.2 Allowed regions by Big-Bang Nucleosynthesis

By numerically solving the Boltzmann equations, we obtain time evolutions of the bound states such as (^{4}He $\tilde{l}^-$), (^{7}Li $\tilde{l}^-$), and (^{7}Be $\tilde{l}^-$) including charge-exchange reactions [50, 51]. Once those bound states are formed, the elements are immediately destroyed through the internal conversion processes for ^{7}Li and ^{7}Be, and the spallation processes for ^{4}He, induced by bound-state effects [4, 52, 5, 6]. Then by solving coupled equations of the reactions including those nonstandard processes, we can obtain final abundances of the light elements. We adopt a value of baryon to photon ratio $\eta = (6.225 \pm 0.170) \times 10^{-10}$ (68% C.L.) which was reported by the WMAP satellite [53]. ^{7}Be and ^{7}Li are efficiently destroyed through the internal conversion processes (3.11a) with a following standard process ^{7}Li $+ p \rightarrow ^4$He$+^4$He, or another subdominant internal conversion process (3.11b). Then we can compare this theoretical value with the observational abundance. It is notable that most of primordial ^{7}Li is produced by primordial ^{7}Be through its electron capture at a much later time for the adopted value of η. We have also included the production process of ^{6}Li through the bound-state effect (3.16) [54, 55].

On the other hand, D and ^{3}He are nonthermally produced by the ^{4}He spallation processes (3.18), and subsequent standard processes for n and p [6]. Note that ^{7}Li or ^{7}Be is also secondarily produced by those nonthermally-produced energetic T and ^{3}He, which may worsen the ^{7}Li problem partly in the parameter spaces.

In Fig. 3.9 we plot regions allowed by observational light element abundances in δm–$Y_{\tilde{l}^-}$ planes in cases of $c_e = 10^{-11}$ (top panel), 5×10^{-11} (middle panel), and 10^{-10} (bottom panel). Lines of the constraints are plotted for D/H, ^{3}He/D, and ^{6}Li/^{7}Li at 2σ. An exception is ^{7}Li/H whose lines are denoted by both dotted lines at 2σ, and solid lines at 3σ. The theoretical curve of the relic abundance is also plotted as a thick solid line. For simplicity, here we have assumed $c_\mu = 0$. Figure 3.10 is the result in case without flavor mixings [7]. The parameters used in the calculation for this figure is same as those for Fig. 3.9. We see that this result is almost same as that with $c_e = 10^{-11}$, the top panel in Fig. 3.9 though the constraints for ^{6}Li/^{7}Li is not imposed in this figure.

In Fig. 3.11, we also plot allowed regions in the δm–c_e plane by using the theoretical value of the relic abundance for the negatively charged slepton at each point of the plane. Each panel is plotted with same parameters. The region on the bottom-left side of thick dotted line is free from ^{7}Li problem at 3σ, and the region on the other side of the line is excluded due to insufficient density of the slepton. The regions between two blue-solid lines are allowed for ^{6}Li/^{7}Li at 2σ. The ^{4}He spallation processes exclude shaded, light shaded, and dark shaded regions due to over-productions of D/H, ^{3}He/D, and ^{7}Li/H at 2σ, respectively. The region on the bottom-left side of left blue-solid line is excluded by ^{6}Li overproduction. Thus the white region in top panel (bottom panel) is the parameter space which is consistent with all of observational light element abundances including ^{7}Li (both ^{7}Li and ^{6}Li).
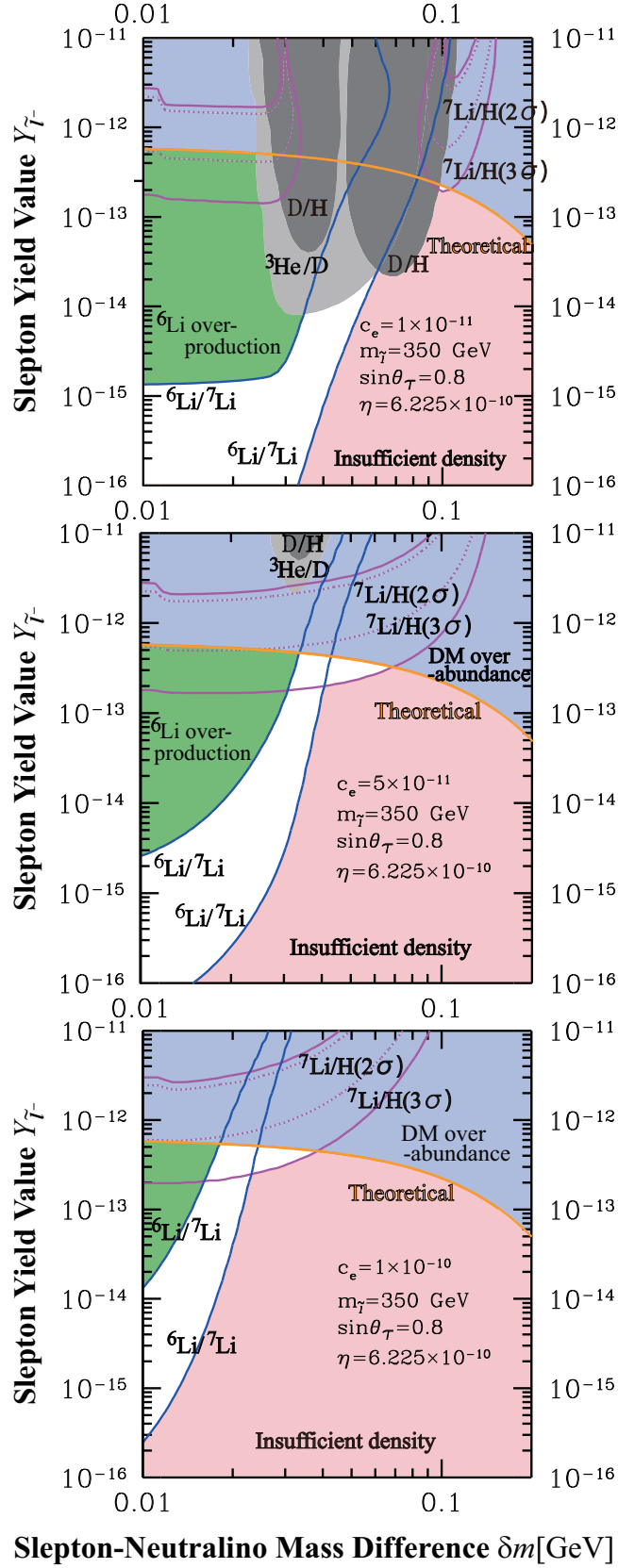
Figure 3.9: Allowed regions by observational light element abundances in δm–$Y_{\tilde{l}^-}$ planes in cases of $c_e = 10^{-11}$ (top panel), 5×10^{-11} (middle panel), and 10^{-10} (bottom panel). The lines of the constraints are plotted for D/H, ^{3}He/D, and ^{6}Li/^{7}Li at 2σ. An exception is ^{7}Li/H whose constraints are denoted by both dotted lines at 2σ, and solid lines at 3σ. The theoretical curve of the relic abundance is also plotted as a thick solid line.
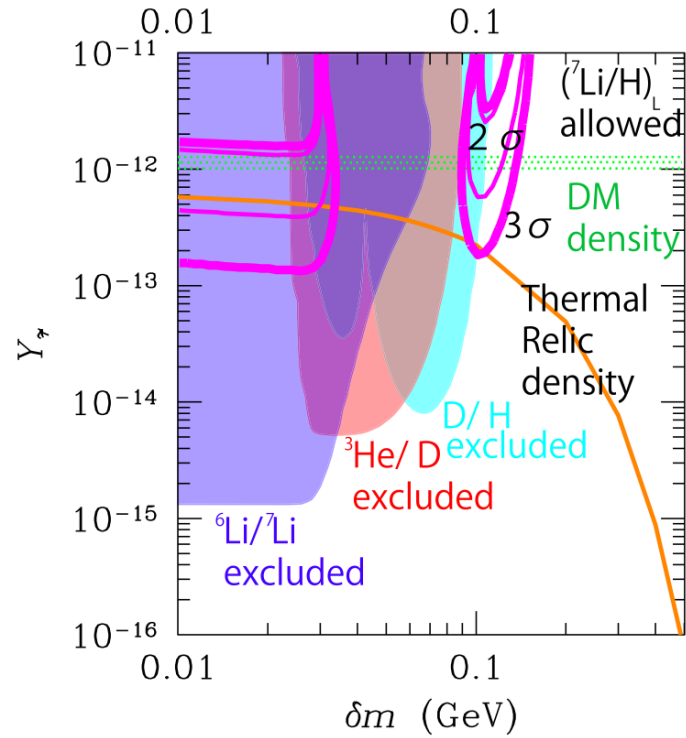
Figure 3.10: Allowed regions from observational light element abundances at 2σ. Here we have adopted higher value of the observational ^{7}Li/H in [9] denoted by $(^7\text{Li/H})_\text{H}$, and have plotted both the 2σ (thin line) and 3σ (thick line) only for ^{7}Li/H. The horizontal band mean the observationally-allowed dark matter density. We have adopted $m_{\tilde{l}} = 350$ GeV, $\sin\theta_l = 0.8$, $\gamma_l = 0$, respectively. This figure is from Ref. [7].
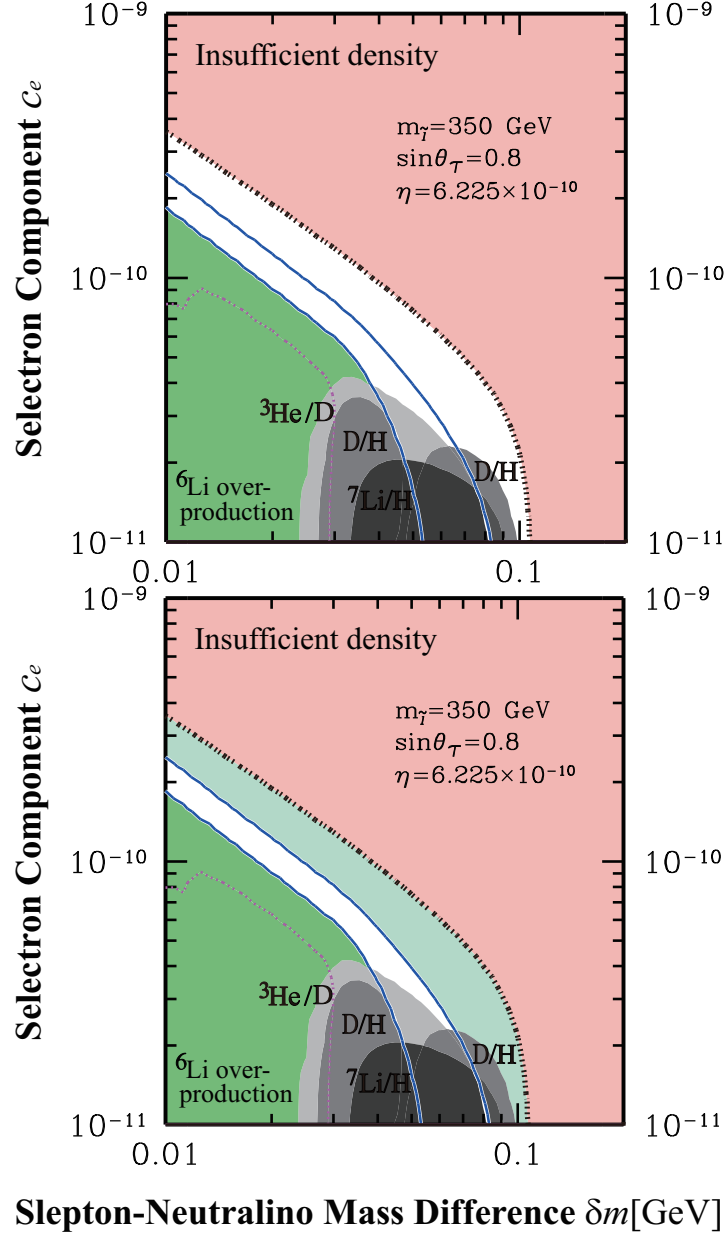
Figure 3.11: Allowed region in the δm–c_e plane. Each panel is plotted with same parameters. The region on the bottom-left side of thick dotted line is free from ^{7}Li problem at 3σ. The regions between two blue-solid lines are allowed for ^{6}Li/^{7}Li. The ^{4}He spallation processes exclude shaded, light shaded, and dark shaded regions due to over-productions of D/H, ^{3}He/D, and ^{7}Li/H, respectively. The region on the bottom-left side of left blue-solid line is excluded by ^{6}Li over-production. The white region in top panel (bottom panel) is the parameter space which is consistent with all of observational light element abundances including ^{7}Li (both ^{7}Li and ^{6}Li).

Chapter 4

Big-Bang Nucleosynthesis with a long-lived slepton in the NMSSM

We finally extend the MSSM into the NMSSM adding a singlet superfield and show that observed light element abundances are obtained as well as dark matter relic density and the Higgs mass.

In the following we first introduce the NMSSM with $\mathcal{Z}_3$ invariance and especially focus on the Higgs mass and neutralino sector in the model. We consider two types of the lightest neutralino, singlino- and bino-ilke ones. Then we propose a strategy to search for the parameter sets which explain observed light element abundances, dark matter relic density, and the Higgs mass. Finally we show the parameter sets desired parameter points are acquired along the strategy.

4.1 The Next-to-Minimal Supersymmetric Standard Model

We recapitulate the Higgs and neutralino sectors, and explain exotic BBN processes with a long-lived slepton in the NMSSM.

4.1.1 Higgs bosons

The NMSSM specific part of the superpotential and the soft-breaking terms are

$$W^{\mathrm{NMSSM}} \supset \lambda \hat{S} \hat{H}_d \cdot \hat{H}_u + \frac{1}{3}\kappa \hat{S}^3, \tag{4.1}$$

$$-\mathcal{L}^{\mathrm{NMSSM}}_{\mathrm{soft}} \supset m_S^2 |S|^2 + \left(\lambda A_\lambda H_d \cdot H_u S + \frac{1}{3}\kappa A_\kappa S^3 + \mathrm{h.c.} \right), \tag{4.2}$$

where $\mathcal{Z}_3$ parity conservation is assumed. In Eq. (4.1), $\hat{H}_d$, $\hat{H}_u$ and $\hat{S}$ are Higgs superfields and the singlet superfield. The couplings λ and κ are dimensionless parameters. In Eq. (4.2),

$$H_d = \begin{pmatrix} H_d^0 \\ H_d^- \end{pmatrix}, \ H_u = \begin{pmatrix} H_u^+ \\ H_u^0 \end{pmatrix}, \ S \tag{4.3}$$

are two Higgs doublets and a singlet scalar. We denote vacuum expectation values of their neutral components by v_d, v_u, and s, respectively. The soft-breaking parameters are m_S, A_λ and A_κ. The free parameters in the Higgs sector are $\lambda, \kappa, A_\lambda, A_\kappa, \tan\beta (\equiv v_u/v_d)$, and $\mu_{\mathrm{eff}} (\equiv \lambda s)$.

The Higgs mass up to dominant 1-loop contribution is

$$
\begin{aligned}
m_h^2 =& m_Z^2 \cos^2 2\beta + \lambda^2 v^2 \sin^2 2\beta - \frac{\lambda^2}{\kappa^2} v^2 (\lambda - \kappa \sin 2\beta)^2 \\
&+ \frac{3m_t^2}{16\pi^2 v^2} \left\{ \log\left(\frac{m_s^2}{m_t^2} \right) + \frac{X_t^2}{m_s^2} \left(1 - \frac{X_t^2}{12m_s^2} \right) \right\},
\end{aligned}
\tag{4.4}
$$

where m_Z is Z boson mass, $m_s \equiv \sqrt{m_{\tilde{t}_1} m_{\tilde{t}_2}}$ is geometric mean of stop masses, $X_t = A_t - \mu_{\text{eff}} \cot \beta$, and $v = \sqrt{v_d^2 + v_u^2}$. The second and third tree terms are characteristic in the NMSSM, and can lift up the Higgs mass. This is one of the attractive features of the model. In contrast, significant 1-loop contribution (the last term in Eq. (4.4)) is required to obtain the Higgs mass around 125 GeV in the MSSM since the tree contribution is at most m_Z. The 1-loop contribution is maximized by the relation, $X_t = \sqrt{6} m_s$, with large stop mass scale. In the NMSSM we do not need to rely on such conditions to obtain observed Higgs mass.

Figure 4.1 shows upper bound (m_{max}) on the Higgs mass in the NMSSM and the MSSM as a function of $\tan \beta$ [56]. For the calculation, not only the leading 1-loop term but also higher order perturbation terms are included. Two solid lines (thick: $m_t = 178$ GeV, thin: $m_t = 171.4$ GeV) are m_{max} for arbitrary value of the CP-odd scalar mass m_A and two dotted lines are those for $m_A = 1$ TeV in the NMSSM. Thick-(thin-)dashed line is that for $m_t = 178(171.4)$ GeV in the MSSM. Squark and gluino masses are 1 TeV and $A_t = A_b = 2.5$ TeV. We see that m_{max} is maximized for large $\tan \beta$ in the MSSM, but it is typically smaller than that in the NMSSM especially for small $\tan \beta$ region.
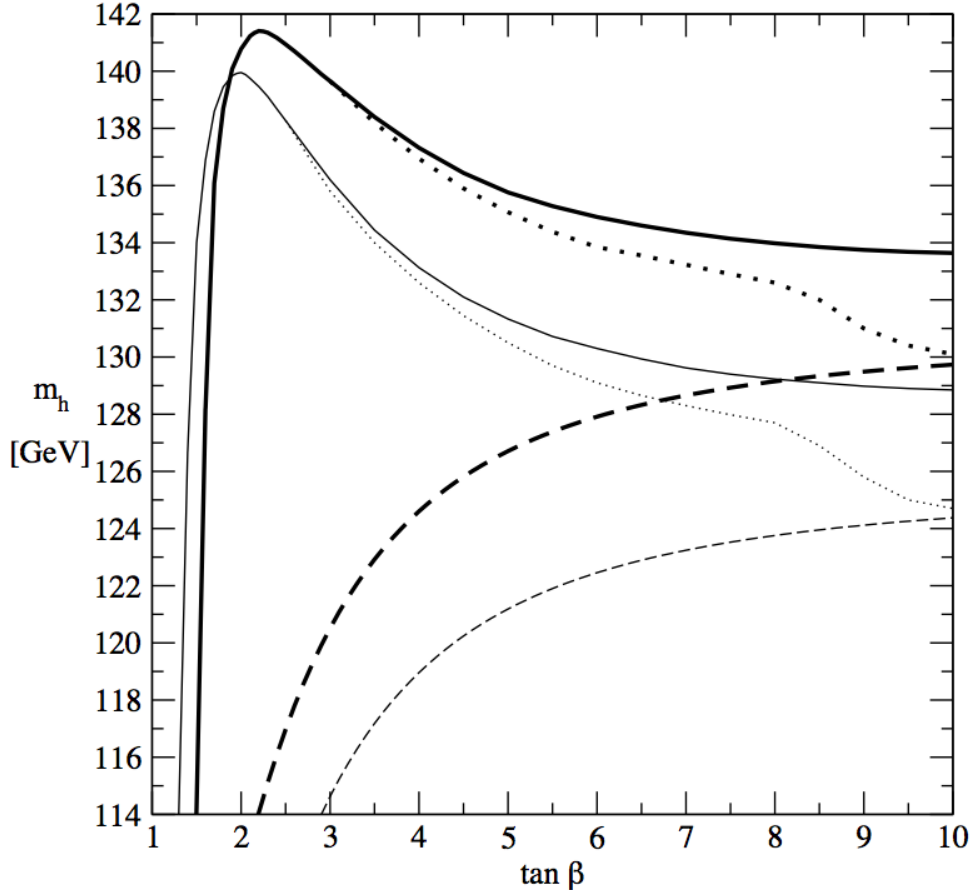
Figure 4.1: Upper bound on the Higgs mass in the NMSSM and the MSSM as a function of $\tan \beta$. For the calculation, not only the leading 1-loop term but also higher order perturbation terms are included. Two solid lines (thick: $m_t = 178$ GeV, thin: $m_t = 171.4$ GeV) are m_{max} for arbitrary value of the CP-odd scalar mass m_A and two dotted lines are those for $m_A = 1$ TeV in NMSSM. Thick-(thin-)dashed line is that for $m_t = 178(171.4)$ GeV in the MSSM. Squark and gluino masses are 1 TeV and $A_t = A_b = 2.5$ TeV. This figure is from Ref. [56].

4.1.2 Neutralinos

In the NMSSM the neutralinos are linear combinations of bino $\tilde{B}$, wino $\tilde{W}$, neutral higgsinos $\tilde{H}_d^0$ and $\tilde{H}_u^0$, and singlino $\tilde{S}$, the supersymmetric partner of the singlet scalar:

$$\tilde{\chi}_i^0 = N_{i\tilde{B}}\tilde{B} + N_{i\tilde{W}}\tilde{W} + N_{i\tilde{H}_d^0}\tilde{H}_d^0 + N_{i\tilde{H}_u^0}\tilde{H}_u^0 + N_{i\tilde{S}}\tilde{S}, \tag{4.5}$$

where i runs from 1 to 5. The mass matrix of the neutralinos is given by the following symmetric expression in the basis $(\tilde{B}, \tilde{W}, \tilde{H}_d^0, \tilde{H}_u^0, \tilde{S})$:

$$\mathcal{M}_{\tilde{\chi}^0} = \begin{pmatrix} M_1 & 0 & -c_\beta s_W m_Z & s_\beta s_W m_Z & 0 \\ & M_2 & c_\beta c_W m_Z & -s_\beta c_W m_Z & 0 \\ & & 0 & -\mu_{\text{eff}} & -\mu_\lambda s_\beta \\ & & & 0 & -\mu_\lambda c_\beta \\ & & & & \mu_\kappa \end{pmatrix}, \tag{4.6}$$

where M_1 and M_2 are masses of the gauginos, $c_\beta = \cos\beta, s_\beta = \sin\beta, c_W = \cos\theta_W, s_W = \sin\theta_W$, $\mu_\lambda = \lambda v$, and $\mu_\kappa = 2\kappa s$. Here θ_W is the Weinberg angle. We consider the case where the LSP is the lightest neutralino, $\tilde{\chi}_1^0$, and the NLSP is the lightest slepton, $\tilde{l}$.

As we will see later, the interaction among $\tilde{\chi}_1^0, \tilde{l}$, and a lepton f is a key ingredient in this study. The interaction Lagrangian is written as

$$-\mathcal{L}_{\tilde{\chi}_1^0\text{-}f\text{-}\tilde{l}} = \tilde{l}^* \overline{\tilde{\chi}_1^0}(G_{\text{L}f}P_{\text{L}} + G_{\text{R}f}P_{\text{R}})f + \text{h.c.}, \tag{4.7}$$

where

$$G_{\text{L}f} = c_f\left[\frac{g_2}{\sqrt{2}}\cos\theta_f(\tan\theta_W N_{1\tilde{B}} + N_{1\tilde{W}}) - \frac{m_f g_2}{\sqrt{2}m_W\cos\beta}\sin\theta_f N_{1\tilde{H}_d^0}\right], \tag{4.8}$$

$$G_{\text{R}f} = c_f\left[\sqrt{2}g_2\sin\theta_f\tan\theta_W N_{1\tilde{B}} + \frac{m_f g_2}{\sqrt{2}m_W\cos\beta}\cos\theta_f N_{1\tilde{H}_d^0}\right]. \tag{4.9}$$

Here m_f is the mass of the lepton f, and $f = e$, μ, and τ. The slepton is expanded as a linear combination of the flavor eigenstates Eq. (3.9).

We study two scenarios where the lightest neutralino is singlino- and bino-like. The detailed expressions of $\tilde{\chi}_1^0$ and the couplings $G_{\text{L}f}$ and $G_{\text{R}f}$ are different between the two cases. In the followings, we explicitly write down the mixing of the lightest neutralino in each case up to the second order in perturbation theory.

Singlino-like neutralino LSP

Up to the second order perturbative expansion, the singlino-like neutralino is

$$\tilde{\chi}^0 = -\frac{m_Z\mu_{\text{eff}}\mu_\lambda s_W c_{2\beta}}{(\mu_\kappa - M_1)(\mu_\kappa^2 - \mu_{\text{eff}}^2)}\tilde{B} + \frac{m_Z\mu_{\text{eff}}\mu_\lambda c_W c_{2\beta}}{(\mu_\kappa - M_2)(\mu_\kappa^2 - \mu_{\text{eff}}^2)}\tilde{W}$$
$$+ \frac{\mu_\lambda(\mu_{\text{eff}}c_\beta - \mu_\kappa s_\beta)}{\mu_\kappa^2 - \mu_{\text{eff}}^2}\tilde{H}_d^0 + \frac{\mu_\lambda(\mu_{\text{eff}}s_\beta - \mu_\kappa c_\beta)}{\mu_\kappa^2 - \mu_{\text{eff}}^2}\tilde{H}_u^0 + \tilde{S}, \tag{4.10}$$

where $c_{2\beta} = \cos 2\beta$, and the normalization factor is omitted. If the neutralino Eq. (4.10) is the LSP, the mixings $N_{1\tilde{B}}, N_{1\tilde{W}}$ and $N_{1\tilde{H}_d^0}$ in Eqs. (4.8) and (4.9) can be read off by comparing Eqs. (4.5) and (4.10). The free parameters in $G_{\text{L}f}$ and $G_{\text{R}f}$ are $M_1, M_2, \lambda, \kappa, \tan\beta, c_f$, and θ_f.

Bino-like neutralino LSP

Up to the second order perturbative expansion, the bino-like neutralino is

$$\tilde{\chi}^0 = \tilde{B} - \frac{m_Z^2 s_W c_W (M_1 + \mu_{\text{eff}} s_{2\beta})}{(M_1 - M_2)(M_1^2 - \mu_{\text{eff}}^2)} \tilde{W} - \frac{m_Z s_W (M_1 c_\beta + \mu_{\text{eff}} s_\beta)}{M_1^2 - \mu_{\text{eff}}^2} \tilde{H}_d^0$$
$$+ \frac{m_Z s_W (M_1 s_\beta + \mu_{\text{eff}} c_\beta)}{M_1^2 - \mu_{\text{eff}}^2} \tilde{H}_u^0 - \frac{m_Z \mu_{\text{eff}} \mu_\lambda s_W c_{2\beta}}{(M_1 - \mu_\kappa)(M_1^2 - \mu_{\text{eff}}^2)} \tilde{S}, \tag{4.11}$$

where $s_{2\beta} = \sin 2\beta$, and the normalization factor is omitted. If the neutralino Eq. (4.11) is the LSP, the mixings $N_{1\tilde{B}}, N_{1\tilde{W}}$ and $N_{1\tilde{H}_d^0}$ in Eqs. (4.8) and (4.9) can be read off by comparing Eqs. (4.5) and (4.11). The free parameters in $G_{\text{L}f}$ and $G_{\text{R}f}$ are $M_1, M_2, \lambda, \tan\beta, \mu_{\text{eff}}, c_f$, and θ_f. The couplings do not depend on κ.

4.1.3 BBN with a long-lived slepton

We explain exotic BBN processes caused by a long-lived slepton. Then we explain the difference of the couplings $G_{\text{L}f}$ and $G_{\text{R}f}$ between the NMSSM and the MSSM.

A long-lived slepton

The relic density of dark mater is well described by the coannihilation mechanism [47]. It requires the small mass difference δm between the neutralino LSP and the slepton NLSP. The two-body decay $\tilde{l} \to \tilde{\chi}_1^0 + \tau$ is kinematically forbidden when $\delta m < m_\tau$. Let us first consider the case where $c_e = c_\mu = 0$ and $c_\tau = 1$. In this case, the flavor is conserved and the slepton is stau. The only allowed decay channel is three- and four-body decay. These decay rates are suppressed due to the small phase space and the small couplings, and hence the sleptons become long-lived. Then it survives until the BBN era to form bound states with nuclei. Such long-lived slepton can account for the discrepancy of the lithium by exotic nuclear reactions with the bound state.

This situation radically changes when c_e and/or c_μ are nonzero as the flavor violating two-body decay channels

$$\tilde{l} \to \tilde{\chi}_1^0 + f, \quad f \ni e, \mu \tag{4.12}$$

open up. These channels do not suffer from the phase-space suppressions and the coupling suppressions, and thus may make the slepton lifetime much shorter. We note that the lifetime is proportional to $(G_{\text{L}f} + G_{\text{R}f})^{-2}$ where $f = \mu$ and e.

Exotic BBN reactions

As we saw in Sec. 3.3, there are three types of exotic BBN reactions with long-lived slepton, the internal conversion processes (3.11), the catalyzed fusion process (3.16), and the ^{4}He spallation processes (3.18).

The timescale to form bound state (^{7}Be $\tilde{l}^-$) is $\mathcal{O}(10^3)$ s [5]. This timescale is important because the primordial ^{7}Li exists as ^{7}Be in the BBN era. The internal conversion processes (3.11) proceed much faster and thus ^{7}Be is very efficiently destroyed. We note that ^{7}Li from (3.11a) is also destroyed by background protons. Thus if the slepton lifetime is longer than 10^3 s, we can obtain observed abundance of ^{7}Li through the internal conversion processes. We can control the timescales of the internal conversion processes (3.11) by changing free parameters in $G_{\text{L}\tau}$, $G_{\text{R}\tau}$, and δm.

The timescale to form bound state (^{4}He $\tilde{l}^-$) is $\mathcal{O}(10^4)$ s [5]. The abundance of ^{6}Li has sever upper bound. The abundance through the catalyzed fusion process (3.16) strongly depends on the slepton lifetime. Therefore, since the process can overproduce ^{6}Li, it gives an upper bound of the slepton

lifetime. We can solve the ^{6}Li problem by producing tiny amount of ^{6}Li through the catalyzed fusion process (3.16). In the situation, the slepton lifetime has to be tuned so that sufficient amount of ^{6}Li is produced. Therefore, the catalyzed fusion process (3.16) can also give lower bound of the slepton lifetime. The amount of ^{6}Li can be controlled by changing free parameters in G_{Lf} and G_{Rf} through the slepton lifetime since the timescale of the catalyzed fusion process (3.16) depend on neither G_{Lf} nor G_{Rf} where $f = \tau, \mu$, and e.

The standard BBN can predict observed abundances of ^{3}He and D. Therefore, the ^{4}He spallation processes (3.18) should not be efficient, which gives upper bound on their timescales and the slepton lifetime. We can also control these timescales by changing the parameters in $G_{L\tau}$, and $G_{R\tau}$ so that the overproduction of T (^{3}He in later time) and D does not occur.

Difference between the NMSSM and the MSSM

In the limit of $\lambda, \kappa \to 0$ fixing μ_{eff}, the NMSSM with bino-like LSP is reduced to the MSSM as long as we consider the exotic BBN processes [6, 7, 8]. In the singlino-like LSP scenario, the couplings G_{Lf} and G_{Rf} are in general smaller than those in the MSSM, and hence the slepton lifetime tends to be much longer than that in the MSSM. The couplings $G_{L\tau}$ and $G_{R\tau}$ need to be large so that the timescales of the internal conversion processes (3.11) are sufficiently short to solve the ^{7}Li problem. In such situation, however, the timescales of the ^{4}He spallation processes (3.18) are also short, and thus ^{3}He and D can be overproduced. We have to adjust the slepton lifetime to avoid the overproduction taking the flavor mixings of the slepton into account.

Taking these facts into account, we will search for parameter sets which can solve the lithium problems along the strategy that we show in the next section.

4.2 Strategy

We acquire parameter sets giving observed light element abundances, the Higgs mass, and dark matter relic density according to the following strategy.

4.2.1 Search for candidate region on λ-κ plane

We narrow the parameter space on λ-κ plane requiring that the slepton lifetime, $\tau_{\tilde{l}}$, and the timescale of the internal conversion processes, τ_{IC}, are in range where the lithium problems can be solved. Then the parameter region on λ-κ plane can be constrained since the lifetime and the timescale depend on the couplings G_{Lf} and G_{Rf}. We require following condition to be satisfied when δm is around 0.1 GeV.

The requirement for the slepton lifetime is

$$10^3 \text{ s} < \tau_{\tilde{l}} < 10^5 \text{ s}. \tag{4.13}$$

As we mentioned in Sec. 4.1.3, the slepton lifetime must be at least longer than the timescale of bound-state formation for the internal conversion processes Eq. (3.11), $\mathcal{O}(10^3)$ s, in order to obtain observed ^{7}Li abundance. The upper bound 10^5 s comes from the requirement that the slepton has sufficient longevity to produce sufficient amount of ^{6}Li avoiding the overproduction through the catalyzed fusion process (3.16).

We require the timescale of the internal conversion processes to be much shorter than the slepton lifetime so that the internal conversion (3.11) works sufficiently and then solve the ^{7}Li problem,

$$\tau_{\text{IC}} < 0.1\tau_{\tilde{l}}. \tag{4.14}$$

Since the parameter dependence on the timescale is different from that of the slepton lifetime, we introduce the requirement Eq. (4.14) independently from the requirement of the lifetime Eq. (4.13).

In addition, we require that the fraction of singlino in the neutralino LSP is larger than 90%,

$$N_{1\tilde{S}}^2 > 0.9, \tag{4.15}$$

for the singlino-like LSP scenario and the fraction of bino in the neutralino LSP is larger than 90%,

$$N_{1\tilde{B}}^2 > 0.9, \tag{4.16}$$

for the bino-like LSP scenario.

4.2.2 Selection of parameter sets

We impose constraints from the recent results of observational relic density of dark matter and experimental value of the Higgs mass in addition to those in Sec. 4.2.1. We use NMSSMTools 4.1.1 [57, 58, 59, 60, 61]. to calculate dark matter relic density and the Higgs mass. [1] Then we select several parameter sets from the region we obtained in the previous step.

The latest result for observed abundance of dark matter is reported by the Planck Collaboration as

$$0.1118 \leq \Omega_{\mathrm{DM}} h^2 \leq 0.1280 \tag{4.17}$$

at the 3σ level [29], and we apply this result as a constraint. In the calculation, we use MicrOMEGAs [63] included in NMSSMTools.

The latest experimental value of the Higgs mass is

$$m_h = 125.7 \pm 0.3(\text{stat.}) \pm 0.3(\text{syst.}) \text{ GeV} \tag{4.18}$$

by the CMS Collaboration [64], and

$$m_h = 125.5 \pm 0.2(\text{stat.})^{+0.5}_{-0.6}(\text{syst.}) \text{ GeV} \tag{4.19}$$

by the ATLAS Collaboration [65], respectively. There are several public codes for calculation of the Higgs mass, and it is known that uncertainty of about ± 3 GeV exists among their calculations [66, 67, 68, 69, 70]. Then we take the uncertainty into account in this study and require that

$$m_h = 125.6 \pm 3.0 \text{ GeV}. \tag{4.20}$$

4.2.3 Constraints from BBN

We perform reaction network calculations for light elements including the exotic nuclear-reactions with the bound-state effects. The baryon to photon ratio is taken to be $\eta = (6.04 \pm 0.08) \times 10^{-10}$ [29]. Then we obtain allowed regions in the parameters as a function of δm to fit observational light element abundances.

We adopt following observational bounds on light element abundances: the lithium 7 to hydrogen ratio $\text{Log}_{10}(^7\text{Li/H}) = -9.63 \pm 0.06$ [9], the lithium 6 to lithium 7 ratio $^6\text{Li}/^7\text{Li} = 0.046 \pm 0.022$ [10], the deuterium to hydrogen ratio $\text{D/H} = (2.80 \pm 0.20) \times 10^{-5}$ [71], and the helium 3 to deuterium ratio $^3\text{He/D} < 0.87 + 0.27$ [72]. It is notable that our scenario does not change the abundance of ^4He significantly.

---

[1] In the neutralino sector, NMSSMTools includes 1-loop radiative corrections for M_1, M_2, and μ_{eff} when it numerically diagonalize the mass matrix of the neutralino Eq. (4.6). On the other hand, we do not include the loop contribution in calculations of the neutralino masses and mixings for simplicity since the loop effects are negligible in our discussion.

For the moment, in order to obtain milder bounds as conservatively as possible we do not adopt newer observational bounds on the abundance of deuterium such as D/H = $(2.54 \pm 0.05) \times 10^{-5}$ and D/H = $(2.53 \pm 0.04) \times 10^{-5}$. They were quite-recently reported by Pettini and Cooke 2012 [73] and Cooke et al 2013 [74], respectively. About such small errors, we need third-party verifications as soon as possible.

4.3 Results of the BBN with a long-lived slepton in NMSSM

Now we show the results following the strategy shown in the previous section. The neutralino LSP is either singlino- or bino-like. We have two types of phenomenologically favored parameter spaces in each case: one is the region where λ and κ are relatively small, and $\tan\beta$ is large; the other is the region where λ and κ are relatively large, and $\tan\beta$ is small. Therefore, we have four cases. However, we do not consider the case where the neutralino LSP is bino-like, λ and κ are relatively small, and $\tan\beta$ is large. In the limit of $\lambda, \kappa \to 0$ with fixed μ_{eff}, the NMSSM is reduced to the MSSM, so the results are same as that in the MSSM [6, 7, 8]. We consider the other three cases in the followings.

First we consider the case where the neutralino LSP is singlino-like, λ and κ are relatively small ($\kappa \lesssim \lambda \ll 1$), and $\tan\beta$ is large ($\gtrsim 30$) [59]. We take four points of parameter sets and denote them by SS-1, SS-2, SS-3, and SS-4, respectively. Here "SS" stands for the "S"inglino-like neutralino LSP and "S"mall couplings region.

Next we consider the case where the neutralino LSP is singlino-like, λ and κ are relatively large ($0.5 \lesssim \lambda \lesssim 0.7$ and at most same order value of $\kappa \lesssim \lambda$) and $\tan\beta$ is small (~ 2). Large λ with small $\tan\beta$ leads to large tree contributions to the Higgs mass (the second and the third terms in Eq. (4.4)) while it is small in the region of the first case. Actually, λ has its maximal value ~ 0.7 though it depends on κ (see for example Table 1 in [62]). This comes from the requirement to avoid the Landau pole up to the GUT scale. The value of κ should not be much smaller than λ in order to obtain large tree contributions to the Higgs mass; in this case the negative contribution (the third term in Eq. (4.4)) do not become significant. Therefore, we investigate the range from at least 0.5 to 0.7 for λ, and same order of magnitude but relatively small range of κ. We take $\tan\beta \sim 2$ since the tree contributions in Eq. (4.4) are maximized around the value with large λ. We take four points of parameter sets and denote them by SL-1, SL-2, SL-3, and SL-4, respectively. Here "SL" stands for the "S"inglino-like neutralino LSP and "L"arge couplings region.

In the third case we consider the bino-like neutralino LSP and search the same region on λ-κ plane as in the second case [59, 62]. In the NMSSM the tree contributions to the Higgs mass are large, which is different from those the MSSM where well tuned 1-loop contribution is required. We take four points of parameter sets and denote them by BL-1, BL-2, BL-3, and BL-4, respectively. Here "BL" stands for the "B"ino-like neutralino LSP and "L"arge couplings region.

In the following results, we fix the parameters as $m_{\tilde{\chi}_1^0} = 350$ GeV, and $\sin\theta_f = 0.8$ for $f = e, \mu$, and τ.

4.3.1 Singlino-like neutralino LSP; small λ-κ region with large $\tan\beta$

Benchmark points

Figure 4.2 shows the region on a λ-κ plane with large $\tan\beta$ where the requirements, Eqs. (4.13)-(4.15), are satisfied. The left and right panels show the results for $c_e = 2 \times 10^{-9}$ and 10^{-9}, respectively. We discuss only the case for $\tan\beta = 30$ in each panel since we obtain almost same results for $\tan\beta > 30$. The mass of the lightest neutralino, $m_{\tilde{\chi}_1^0 \simeq \mu_\kappa}$, is almost equal to that of the next-to-lightest one, $m_{\tilde{\chi}_2^0} \simeq \mu_{\text{eff}}$, on the dotted line. Above the dotted line, the singlino-like neutralino is no longer the lightest one.

We can see that larger λ and smaller κ are allowed by larger c_e with fixed $\tan\beta$. This is explained by the requirement Eq. (4.13) and the dependence of the couplings, Eqs. (4.8) and (4.9), on λ and κ. These couplings become large as κ increase, and/or λ decreases. The slepton lifetime becomes short as the couplings and/or c_e increase. Therefore, larger c_e gives shorter slepton lifetime and allows the region with larger λ and smaller κ.

To check which requirements determine the favored region in Fig. 4.2, we draw Fig. 4.3 to show the distribution of the quantities which are relevant to the requirements, Eqs. (4.13)-(4.15). The parameters used are $c_e = 2 \times 10^{-9}$, $m_{\tilde{\chi}_1^0} = 350$ GeV, $\delta m = 0.1$ GeV, $\sin\theta_f = 0.8$, $\tan\beta = 30$, $M_1 = 500$ GeV, and $M_2 = 1000$ GeV. From the result we can see the favored region is determined by the requirement for the slepton lifetime of Eq. (4.13).

We take four reference points in the favored region for $\tan\beta = 30$ (red region in Fig. 4.2) as shown in Table 4.1. Table 4.2 shows the spectra and observables at these points. We omit small flavor mixing of the slepton in this calculation, and thus SS-1 and SS-2 give same results. All the dimensionful values are shown in GeV. The top rows show input parameters. We assume the relations for gaugino masses

$$M_1 = M_2/2, M_3 = 3M_2, \tag{4.21}$$

similar to the GUT relation, and, for simplicity, universal input soft-masses for each squark and slepton,

$$m_{\tilde{Q}_{1,2}} = m_{\tilde{Q}_3} = m_{\tilde{U}_{1,2}} = m_{\tilde{U}_3} = m_{\tilde{D}_{1,2}} = m_{\tilde{D}_3},$$
$$m_{\tilde{L}_{1,2}} = m_{\tilde{L}_3}, \; m_{\tilde{E}_{1,2}} = m_{\tilde{E}_3}. \tag{4.22}$$

The middle rows show output spectra. Every points give the observed Higgs mass Eq.(4.20). At these points, m_h receives significant contribution from the 1-loop correction (the fourth term in Eq. (4.4)) by the maximal mixing and large stop masses because the tree contributions (the second and third terms in Eq. (4.4)) are small.

In the bottom rows, we show relic density of the lightest neutralino, spin-independent cross section between the lightest neutralino and nucleon, the SUSY contribution to the muon anomalous magnetic moment, and the branching ratios of rare decays $B_s \to \mu^+\mu^-$ and $b \to s\gamma$, from top to bottom. At each point, the dark matter relic density is in range of the measured value [29]. The spin-independent cross section at each point is about four order of magnitude smaller than the present experimental bound [32]. The latest experimental result for the SUSY contribution to the anomalous magnetic moment is,

$$\delta a_\mu = a_\mu^{\text{exp}} - a_\mu^{\text{SM}} = (26.1 \pm 8.0) \times 10^{-10}, \tag{4.23}$$

where $a_\mu \equiv (g-2)_\mu/2$ [75, 76, 77]. For the branching ratio of $B_s \to \mu^+\mu^-$, the CMS Collaboration recently reported in Ref. [78] as

$$\text{BR}(B_s \to \mu^+\mu^-) = 3.0^{+1.0}_{-0.9} \times 10^{-9} \tag{4.24}$$

and also the LHCb Collaboration reported in Ref. [79] as

$$\text{BR}(B_s \to \mu^+\mu^-) = 2.9^{+1.1}_{-1.0}(\text{stat.})^{+0.3}_{-0.1}(\text{syst.}) \times 10^{-9}. \tag{4.25}$$

The branching ratio of $B \to X_s\gamma$ [80] is given by

$$\text{BR}(B \to X_s\gamma) = (3.43 \pm 0.21 \pm 0.07) \times 10^{-4}. \tag{4.26}$$

At each point, δa_μ and $\text{BR}(B_s \to \mu^+\mu^-)$ are in the ranges of 2σ and 1σ. The branching ratio of $b \to s\gamma$ is in the 2σ range at SS-3 and SS-4.

BBN results at the benchmark points

The left panels in Fig. 4.4 show the slepton lifetime $\tau_{\tilde{l}}$ (red-solid line; "slepton lifetime"), the timescales of the internal conversion processes (3.11a) (blue-solid line; "^{7}Be$\rightarrow^7$Li"), (3.11b) (blue-dash-dotted line; "^{7}Li$\rightarrow^7$He"), the ^{4}He spallation processes (3.18a) (brown-solid line; "tn"), (3.18b) (brown-dashed line; "dnn"), and (3.18c) (brown-dash-dotted line; "pnnn"), as a function of the mass difference between the slepton and the neutralino at SS-1, SS-2, SS-3, and SS-4 from top to bottom, respectively. The horizontal black-dashed line represents the timescale of the catalyzed fusion process (3.16) [55] at the temperature $T = 5$ keV (5×10^4 s) when (^{4}He $\tilde{l}^-$) is formed.

We show the allowed regions in the right panels of Fig. 4.4 which we obtain by comparing theoretical values to observational ones for light element abundances at SS-1, SS-2, SS-3, and SS-4 from top to bottom, respectively. Horizontal axis is the mass difference between the slepton NLSP and the neutralino LSP, and vertical axis is the yield value of the slepton at the beginning of the BBN, $Y_{\tilde{l}^-} = n_{\tilde{l}^-}/s$, where $n_{\tilde{l}^-}$ is the number density of the slepton and s is the entropy density. The regions surrounded by magenta-dotted(-solid) lines are allowed by observed ^{7}Li/H abundance at $2\sigma(3\sigma)$. The regions between the blue-solid line and the blue region are allowed by observed ^{6}Li/^{7}Li abundance at 2σ. The orange-solid lines ("Theoretical") represent the yield value of the slepton calculated with the parameters in Table. 4.2. The colored regions are excluded for ^{6}Li/^{7}Li (blue region; "^{6}Li/^{7}Li excluded"), ^{3}He/D (red region; "^{3}He/D excluded"), and D/H (cyan region; "D/H excluded"), respectively. The shaded and dotted regions are allowed by only ^{7}Li/H (3σ) and both ^{7}Li/H (3σ) and ^{6}Li/^{7}Li (2σ), respectively. At each point, we obtain allowed region from ^{7}Li/H (3σ) and ^{6}Li/^{7}Li (2σ) simultaneously.

We see in the right panels of Fig. 4.4 that the allowed region from ^{7}Li/H on the curve of the slepton yield value is in the range of $\delta m \sim (0.04, 0.07)$, $(0.07, 0.1)$, $(0.07, 0.1)$, and 0.1 GeV at the point SS-1, SS-2, SS-3, and SS-4 respectively. We note that the catalyzed fusion process affects the abundance of the ^{6}Li in these allowed regions even if the time scale of the reaction is much longer than the slepton lifetime and the timescales of the ^{4}He spallation proscesses. This is because the yield value of the slepton is much larger than observed abundance of the ^{6}Li. We roughly calculate a yield value of the ^{6}Li through the catalyzed fusion as follows;

$$\Delta Y_{^6\text{Li}} = Y_{\tilde{l}^-} e^{-\tau_{\text{B.F.}}/\tau_{\tilde{l}}} \frac{\Gamma_{\text{C.F.}}}{\Gamma_{\text{Sp.}} + \Gamma_{\tilde{l}} + \Gamma_{\text{C.F.}}}, \tag{4.27}$$

where $\Delta Y_{^6\text{Li}}$ is the yield value of the ^{6}Li, $\tau_{\text{B.F.}}$ is a timescale of (^{4}He $\tilde{l}^-$) formation, $\Gamma_{\tilde{l}}$ is a decay rate of the slepton, $\Gamma_{\text{Sp.}}$ and $\Gamma_{\text{C.F.}}$ are a reaction rate of the ^{4}He spallation processes and the catalyzed fusion process, respectively. In the equation, $Y_{\tilde{l}^-} e^{-\tau_{\text{B.F.}}/\tau_{\tilde{l}}}$ represents a yield value of the bound state, and the factor at the last of right hand side is the branching ratio of the bound state to the catalyzed fusion reaction. Here we consider the predicted value of the ^{6}Li along with the slepton yield value which we calculate with the parameters shown in Table 4.2. We put the constraint from the observed value on the calculated value as follows;

$$\frac{Y_{^6\text{Li,Ob.}}}{Y_{\tilde{l}^-}} \simeq 10^{-8} e^{-\tau_{\text{B.F.}}/\tau_{\tilde{l}}} \frac{\Gamma_{\text{C.F.}}}{\Gamma_{\text{Sp.}} + \Gamma_{\tilde{l}} + \Gamma_{\text{C.F.}}}, \tag{4.28}$$

where we choose the yield value as $Y_{\tilde{l}} \simeq 10^{-13}$ and $Y_{^6\text{Li,Ob.}} \simeq \mathcal{O}(10^{-21})$ which is the observed yield value of ^{6}Li [10]. We take the timescale of the bound state formation 5×10^4 s (see the Fig. 1 of Ref. [5]), and $\Gamma_{\text{C.F.}} \simeq \mathcal{O}(10^{-10})$ s^{-1}. We see that $\tau_{\tilde{l}} \simeq 10^4$ s and $\Gamma_{\text{Sp.}} \simeq 10^{-5}$ s^{-1} in the allowed region at the left panels of Fig. 4.4. We confirm that the calculated yield value of ^{6}Li is consistent with that of the observational value at the allowed region.

We also see that the allowed range of the mass difference is different in each point. This difference can be explained as follows. The selectron mixing is smaller at SS-2 than at SS-1. The smaller mixing

results in smaller coupling $G_{L,Re}$ and hence longer slepton lifetimes than that at SS-1 shown in the left panels in Fig. 4.4. The longer the lifetime is, the more the exotic BBN reactions occur because a larger number of the sleptons remains until they form bound state with ^{7}Be. More ^{7}Be are destroyed by the internal conversion processe at SS-2 than at SS-1. In such a situation, the yield value of the slepton required by observed ^{7}Li abundance can be smaller for the same δm. In fact, comparing the right panels of Fig. 4.4 of SS-1 and SS-2, we see that the 2 and 3 σ lines of ^{7}Li/H allows lower yield values and larger δm at SS-2. This result also can be understood in terms of the slepton lifetime. The lifetime must be adjusted to a certain range to solve the Li problems. As mentioned in Sec. 4.1.3, the lifetime is determined by both $G_{L,Re}$ and δm. For a fixed lifetime that can explain the observed ^{7}Li abundance, δm is larger when $G_{L,Re}$ is smaller. As a result, the allowed region extends to larger δm at SS-2 than at SS-1. For a longer slepton lifetime, on the other hand, more ^{3}He and D are produced by the ^{4}He spallation processes, and more ^{6}Li is produced by the catalyzed fusion process. Thus, the excluded regions caused by the ^{4}He spallation processes (red and cyan regions) and the catalyzed fusion process (blue region) are large compared to those at SS-1.

At the point SS-3, λ is taken slightly larger than the one at SS-1 while c_e and κ are taken the same. We see that the allowed region is in the range of $\delta m \sim (0.07, 0.1)$ GeV and is larger than that at SS-1. It is because the lifetime is longer than that at SS-1. However, the reason to make the lifetime longer is different from the case of SS-2. At SS-3, larger λ gives longer slepton lifetime (see top-left panel of Fig. 4.2), because $G_{L,Re}$ become smaller than those at SS-1 as shown in Table 4.2, due to the small mixing weights N_1's in the lightest neutralino. In Eq. (4.10), the mixing weights are inversely proportional to $\mu_\kappa^2 - \mu_{\rm eff}^2$. In the singlino-like LSP case, μ_κ and $\mu_{\rm eff}$, hence κ and λ, must be tuned so that $G_{L,R}$ are enough large. In fact, κ and λ are tuned well at SS-1. Taking λ larger than that at SS-1 even by a few %, $G_{L,Re}$ becomes smaller and hence the lifetime becomes longer. At the same time, $G_{L,R\tau}$ become smaller. It is still enough large to reduce ^{7}Be by the internal conversion processes but is small for the ^{4}He spallation processes. Thus, the excluded regions by ^{3}He and D are narrower than those at SS-2.

At SS-4, κ is taken by 1 % smaller than the one at SS-1 while the other parameters are taken the same. Again, due to the smaller κ, the lifetime of the slepton is longer than at SS-1, and indeed is the longest among the four parameters (see the left panels in Fig. 4.4). Then ^{3}He and D are too much produced even for smaller slepton yield values so that the excluded region from D/H narrows the allowed region. Furthermore, the timescales of the internal conversion processes (3.11) are longer than those at the other points. Thus more slepton yield value is necessary to obtain the observed abundance of ^{7}Li, and hence the allowed region at SS-1 is narrower.

In the end, it is important to notice that in the singlino-like LSP case, κ and λ must be well tuned to obtain fast internal conversion processes. As we have shown, only a few % of difference in the parameters drastically change the results. Thus, due to this tuning, our scenario is very predictable.
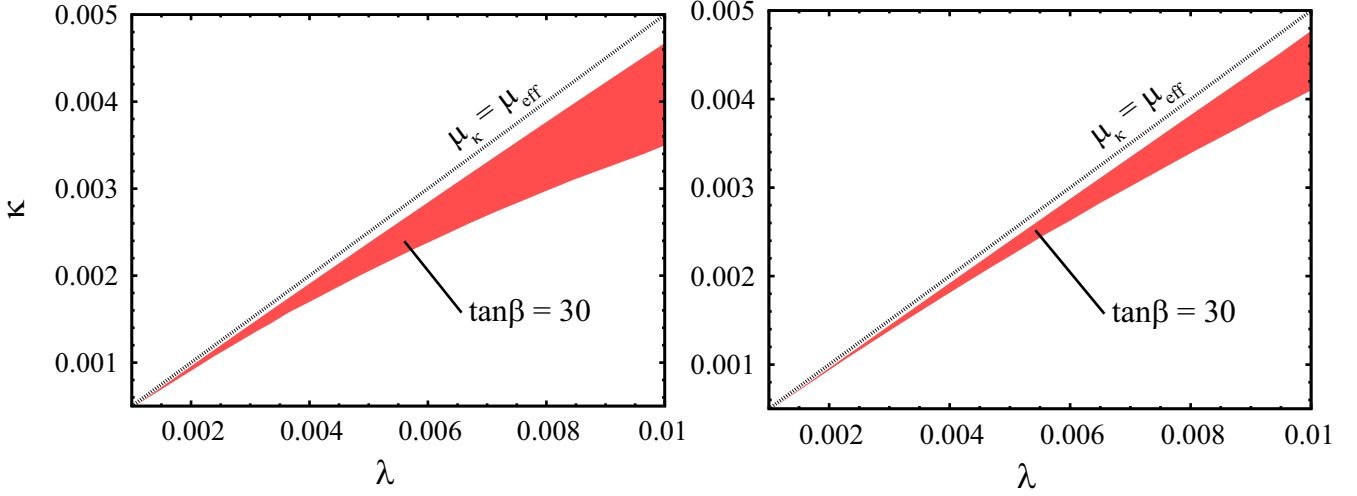
Figure 4.2: Favored region (red region; "$\tan\beta = 30$") in terms of requirements Eqs. (4.13)-(4.15) in λ-κ plane. Parameters are taken as $\tan\beta = 30$ and $c_e = 2 \times 10^{-9}$(left panel) and $c_e = 10^{-9}$(right panel). Other parameters are fixed as $m_{\tilde{\chi}_1^0} = 350$ GeV, $\delta m = 0.1$ GeV, $\sin\theta_f = 0.8$, $M_1 = 500$ GeV, and $M_2 = 1000$ GeV. The singlino-like neutralino is no longer the lightest one above the dotted line.
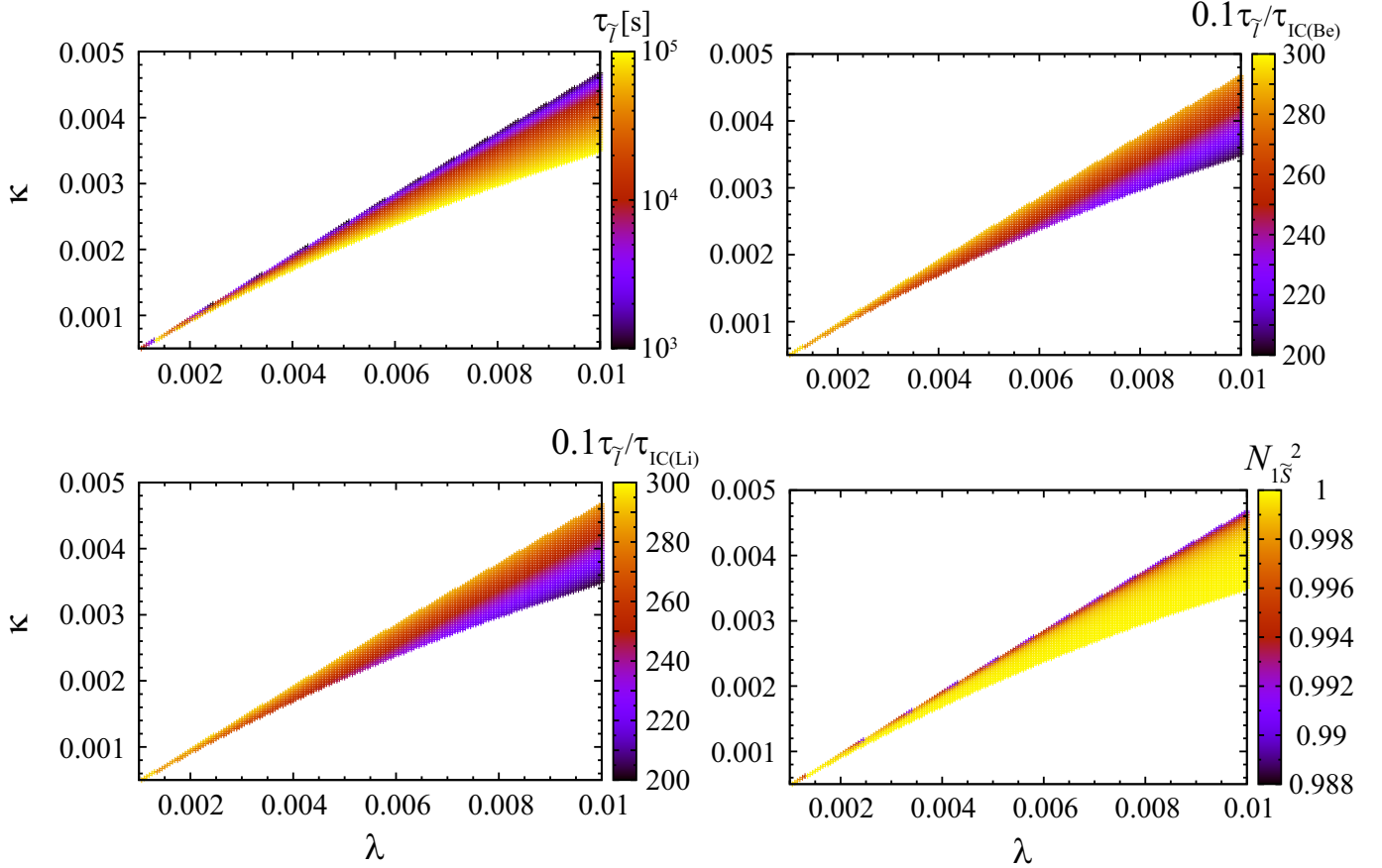
Figure 4.3: The distribution of the quantities relevant to the requirements, Eqs. (4.13)-(4.15), in the favored region from $c_e = 2 \times 10^{-9}$ and $\tan\beta = 30$. The color bar in each panel shows $\tau_{\tilde{l}}$ (top-left), $0.1\tau_{\tilde{l}}/\tau_{\mathrm{IC}}$ for $(^7\mathrm{Be}\,\tilde{l}^-) \to {}^7\mathrm{Li} + \tilde{\chi}_1^0 + \nu_l$ (top-right), $0.1\tau_{\tilde{l}}/\tau_{\mathrm{IC}}$ for $(^7\mathrm{Li}\,\tilde{l}^-) \to {}^7\mathrm{He} + \tilde{\chi}_1^0 + \nu_l$ (bottom-left), and $N_{1\tilde{S}}^2$ (bottom-right).

Table 4.1: Benchmark points in the favored region of Fig. 4.2.

Parameters	SS-1	SS-2	SS-3	SS-4
c_e	2×10^{-9}	10^{-9}	2×10^{-9}	2×10^{-9}
λ	0.0042	0.0042	0.00425	0.0042
κ	0.002	0.002	0.002	0.00195

Table 4.2: Spectra and observables at each point (see Tab. 4.1). All the dimensionful values are shown in GeV. The top rows show input parameters. SS-1 and SS-2 give common results since we omit small flavor mixing of the slepton. The middle rows show output spectra. The bottom rows show relic density of the lightest neutralino, spin-independent cross section between the lightest neutralino and nucleon, the SUSY contribution to the muon anomalous magnetic moment, and the branching ratios of rare decays $B_s \to \mu^+\mu^-$ and $b \to s\gamma$, and couplings Eqs. (4.8) and (4.9) from top to bottom.

| Input	SS-1, SS-2	SS-3	SS-4
M_2	1000.0	1000.0	1000.0
A_t	-3000.0	-4800.0	-7500.0
$m_{\tilde{L}_3}$	391.30	397.06	405.43
$m_{\tilde{E}_3}$	372.99	376.34	381.29
$m_{\tilde{Q}_3}$	1500.0	2000.0	3000.0
λ	0.0042	0.00425	0.0042
κ	0.0020	0.0020	0.00195
A_λ	1000.0	1300.0	1000.00
A_κ	-100.00	-100.00	-100.00
μ_{eff}	359.82	363.07	366.76
$\tan\beta$	30.000	30.000	30.000
Output			
h_1^0	123.89	126.16	127.30
h_2^0	316.70	317.05	314.58
h_3^0	3513.4	3939.4	3499.3
a_1^0	226.72	226.40	226.02
a_2^0	3513.4	3939.4	3499.3
$H^\pm$	3514.2	3940.1	3500.0
$\tilde{t}_1$	1367.9	1897.7	2925.2
$\tilde{t}_2$	1650.6	2235.9	3271.5
$\tilde{\tau}_1$	350.10	350.10	350.10
$\tilde{\tau}_2$	416.67	425.01	437.11
$\tilde{\chi}_1^0$	350.00	350.00	350.00
$\tilde{\chi}_2^0$	355.27	359.35	364.03
$\tilde{\chi}_3^0$	370.74	375.08	380.10
$\tilde{\chi}_4^0$	498.84	498.04	496.76
$\tilde{\chi}_5^0$	1021.1	1027.8	1035.7
$\Omega_{\tilde{\chi}_1^0}h^2$	0.11236	0.12656	0.12490
$\sigma_{\text{SI}}[\text{cm}^2]$	9.4085×10^{-49}	1.4012×10^{-49}	3.8721×10^{-50}
δa_μ	$1.1967 \times 10^{-9}(2\sigma)$	$1.2656 \times 10^{-9}(2\sigma)$	$1.2347 \times 10^{-9}(2\sigma)$
$\text{Br}(B_s^0 \to \mu^+\mu^-)$	$3.3924 \times 10^{-9}(1\sigma)$	$3.4349 \times 10^{-9}(1\sigma)$	$3.4442 \times 10^{-9}(1\sigma)$
$\text{Br}(b \to s\gamma)$	$2.5984 \times 10^{-4}(>3\sigma)$	$2.8109 \times 10^{-4}(2\sigma)$	$3.0311 \times 10^{-4}(2\sigma)$
$G_{\text{L}\tau}/c_\tau$	-0.014882	-0.0084607	-0.0055185
$G_{\text{R}\tau}/c_\tau$	0.019332	0.011050	0.0072524
$G_{\text{L}e}/c_e$	0.00066840	0.00038490	0.00025476
$G_{\text{R}e}/c_e$	0.0076689	0.0044158	0.0029225
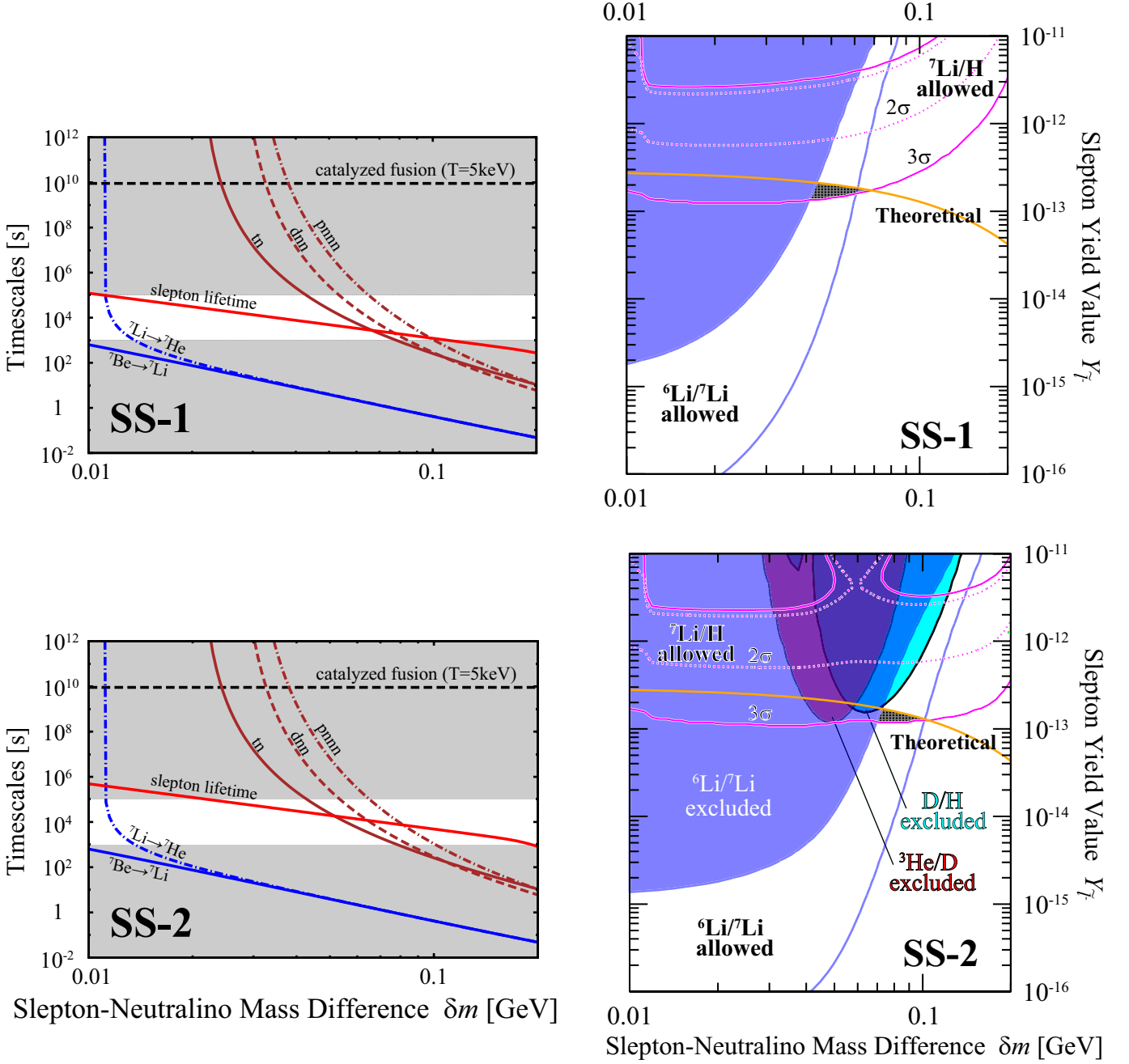
Figure 4.4: The left panels show the slepton lifetime $\tau_{\tilde{l}}$ (red-solid line; "slepton lifetime"), the timescales of the internal conversion processes (3.11a) (blue-solid line; "^{7}Be→^{7}Li"), (3.11b) (blue-dash-dotted line; "^{7}Li→^{7}He"), the ^{4}He spallation processes (3.18a) (brown-solid line; "tn"), (3.18b) (brown-dashed line; "dnn"), and (3.18c) (brown-dash-dotted line; "pnnn"), as a function of the mass difference between the slepton and the neutralino at SS-1 (top panel) and SS-2 (bottom panel). We also show the timescale of the catalyzed fusion (3.16) at the temperature $T = 5$ keV (5×10^4 s) when (^{4}He $\tilde{l}^-$) is formed as horizontal black-dashed line. In shaded regions Eq. (4.13) is not satisfied. The right panels show the allowed regions from observational light element abundances on δm-$Y_{\tilde{l}^-}$ plane at SS-1 (top panel) and SS-2 (bottom panel). The regions surrounded by magenta-dotted(-solid) lines are allowed by observed ^{7}Li/H abundance at $2\sigma(3\sigma)$. The regions between the blue-solid line and the blue region are allowed by observed ^{6}Li/^{7}Li abundance at 2σ. The orange-solid lines ("Theoretical") represent the yield value of the slepton at the begging of the BBN as a function of the mass difference. The colored regions are excluded for ^{6}Li/^{7}Li (blue region; "^{6}Li/^{7}Li excluded"), ^{3}He/D (red region; "^{3}He/D excluded"), and D/H (cyan region; "D/H excluded"), respectively. The shaded and dotted regions are allowed by only ^{7}Li/H (3σ) and both ^{7}Li/H (3σ) and ^{6}Li/^{7}Li (2σ), respectively.
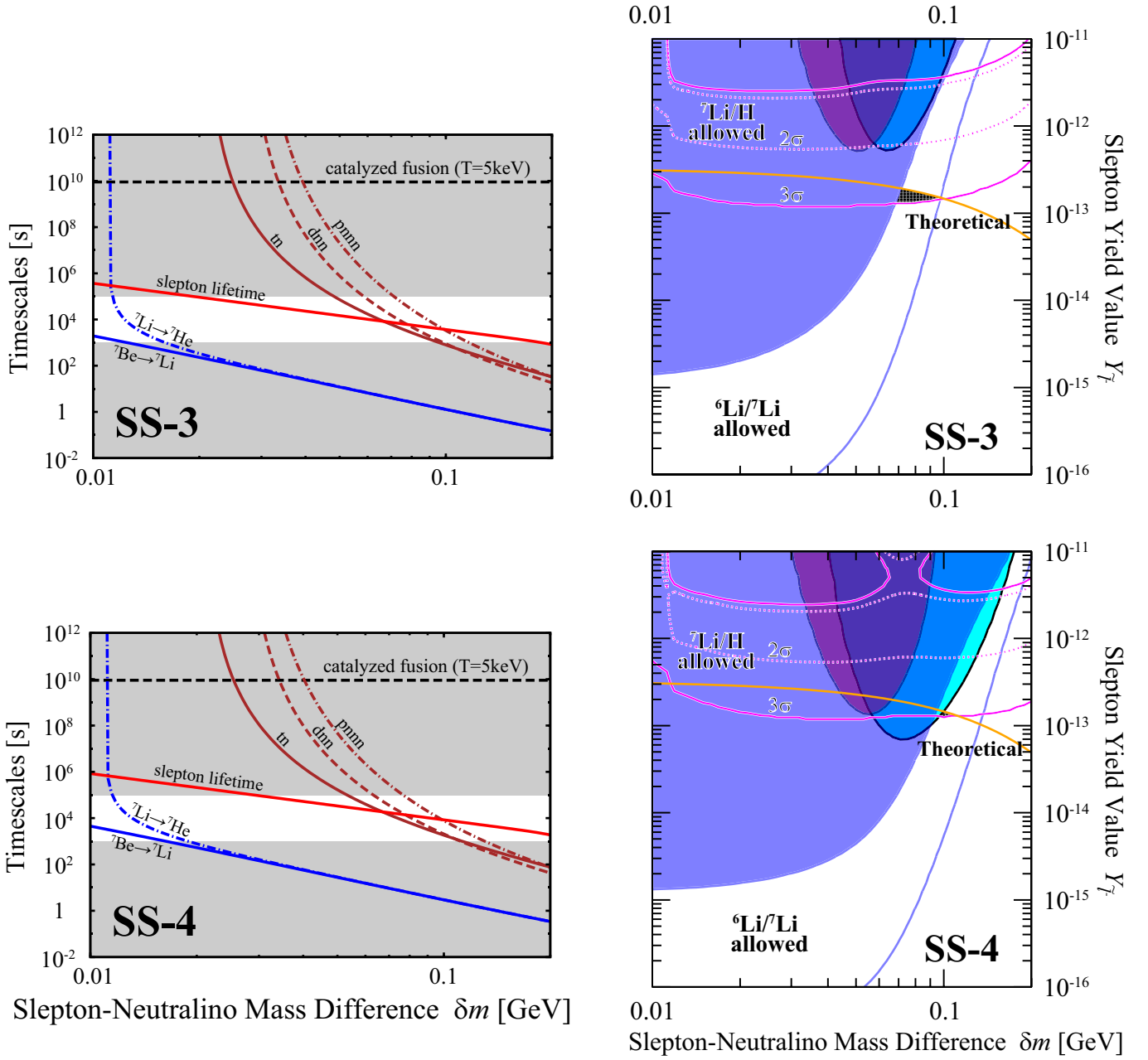
Figure 4.3: The results at SS-3 (top panels) and SS-4 (bottom panels) are shown. The lines and regions stand for the same meanings as those in the previous page.

4.3.2 Singlino-like neutralino LSP; large λ-κ region with small $\tan\beta$

Benchmark points

Figure 4.4 shows the favored region on λ-κ plane with small $\tan\beta$ where the requirements, Eqs. (4.13)-(4.15), are satisfied. The left and right panels show the results for $c_e = 5 \times 10^{-10}$ and 2×10^{-10}, respectively. The red and hatched regions are allowed by $\tan\beta = 2$ and 2.5, respectively.

To check which requirements determine the favored region in Fig. 4.4, we draw Fig. 4.5 to show the distribution of the quantities which are relevant to Eqs. (4.13)-(4.15). The parameters are $c_e = 5 \times 10^{-10}, m_{\tilde\chi_1^0} = 350$ GeV, $\delta m = 0.1$ GeV, $\sin\theta_f = 0.8, \tan\beta = 2, M_1 = 500$ GeV, and $M_2 = 1000$ GeV. From the result we see the favored region is determined by the requirement for the slepton lifetime Eq. (4.13).

We take four reference points in the favored region for $\tan\beta = 2$ (red regions in Fig. 4.4) as shown in Table 4.3. Table 4.4 shows the spectra and observables at these points. We omit small flavor mixing of the slepton in the calculation, and show the dimensionful values in GeV. Every points give the observed Higgs mass. In this case where λ and κ are large and $\tan\beta$ is small, the tree contributions in Eq. (4.4) (the second and the third terms) are significant, and 1-loop contribution (the forth term) is not so large.

In the bottom rows, we show relic density of the lightest neutralino, spin-independent cross section between the lightest neutralino and nucleon, the SUSY contribution to the muon anomalous magnetic moment, and the branching ratios of rare decays $B_s \to \mu^+\mu^-$ and $b \to s\gamma$, from top to bottom. At each point, the dark matter relic density is in range of the measured value [29]. The spin-independent cross section at each point is much larger than those at the points in the previous section and just below the present experimental bound. The calculated values of δa_μ at the points are out of 3σ range, since $\tan\beta$ is relatively small in this case. For the branching ratio of $B_s \to \mu^+\mu^-$ and $b \to s\gamma$, we obtained the values within 1σ and 2σ, respectively.

BBN results at the benchmark points

The left panels in Fig. 4.6 show the slepton lifetime $\tau_{\tilde l}$ (red-solid line; "slepton lifetime"), the timescales of the internal conversion processes (3.11a) (blue-solid line; "^{7}Be→^{7}Li"), (3.11b) (blue-dash-dotted line; "^{7}Li→^{7}He"), the ^{4}He spallation processes (3.18a) (brown-solid line; "tn"), (3.18b) (brown-dashed line; "dnn"), and (3.18c) (brown-dash-dotted line; "pnnn"), as a function of the mass difference between the slepton and the neutralino at SL-1, SL-2, SL-3, and SL-4 from top to bottom, respectively. The horizontal black-dashed line represents the timescale of the catalyzed fusion process (3.16) [55] at the temperature $T = 5$ keV (5×10^4 s) when (^{4}He $\tilde l^-$) is formed. In the right panels horizontal axis is the mass difference between the slepton NLSP and the neutralino LSP, and vertical axis is the yield value of the slepton at the beginning of the BBN.

We show the allowed regions in the right panels of Fig. 4.6 which we obtain by comparing theoretical values to observational ones for light element abundances at SL-1, SL-2, SL-3, and SL-4 from top to bottom, respectively. The lines and regions are the same as in Fig. 4.4. Thus we obtain allowed region from ^{7}Li/H (3σ) and ^{6}Li/^{7}Li (2σ) simultaneously at each point.

The points SL-3 and SL-4 have larger λ and smaller κ compared with those at SL-1, respectively. The couplings $G_{L,R}$ at these points, however, are not different from each other, since λ and κ are enough large so that we can get large $G_{L,R}$ without tuning in contrast to SS case. Thus we get similar result at these points.

On the contrary, at SL-2 the selectron mixing is small compared with that of SL-1, and hence the slepton lifetime is longer than the other points. This result in more spallation processes and make the allowed region narrower.
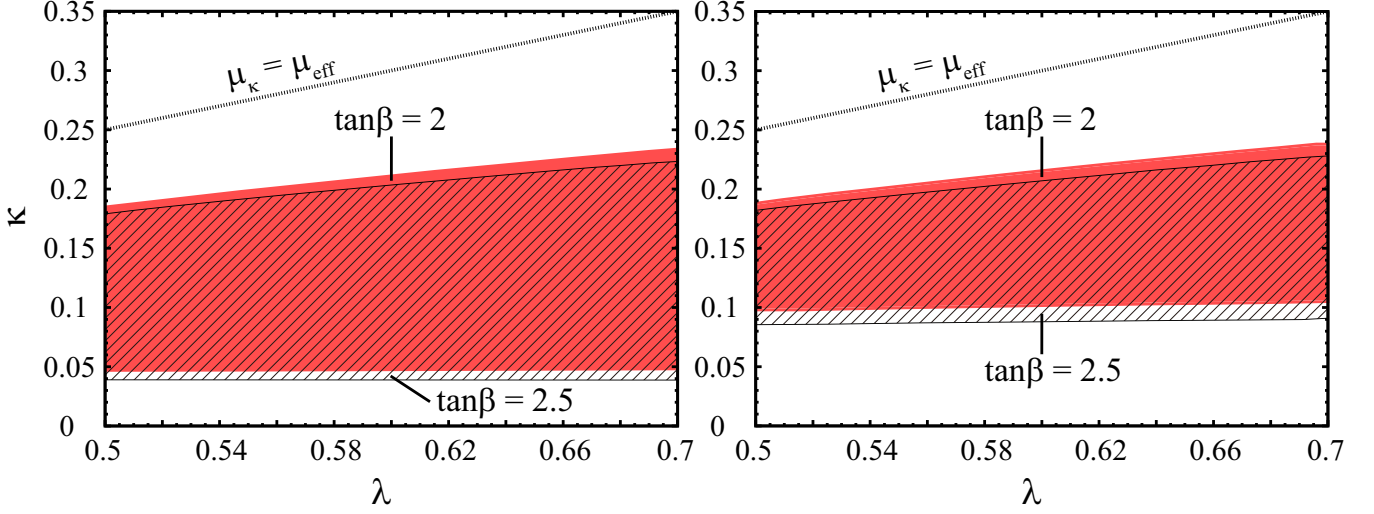
Figure 4.4: Favored region in terms of requirements Eqs. (4.13)-(4.15) in λ-κ plane. We took $\tan\beta = 2$ and 2.5 and $c_e = 5 \times 10^{-10}$ in left panel ($c_e = 2 \times 10^{-10}$ in right panel). Fixed parameters are $m_{\tilde{\chi}_1^0} = 350$ GeV, $\delta m = 0.1$ GeV, $\sin\theta_f = 0.8$, $M_1 = 500$ GeV, and $M_2 = 1000$ GeV. Red and shaded regions are the favored region from $\tan\beta = 2$ and 2.5, respectively. The singlino-like neutralino is no longer the lightest one above the dotted line.
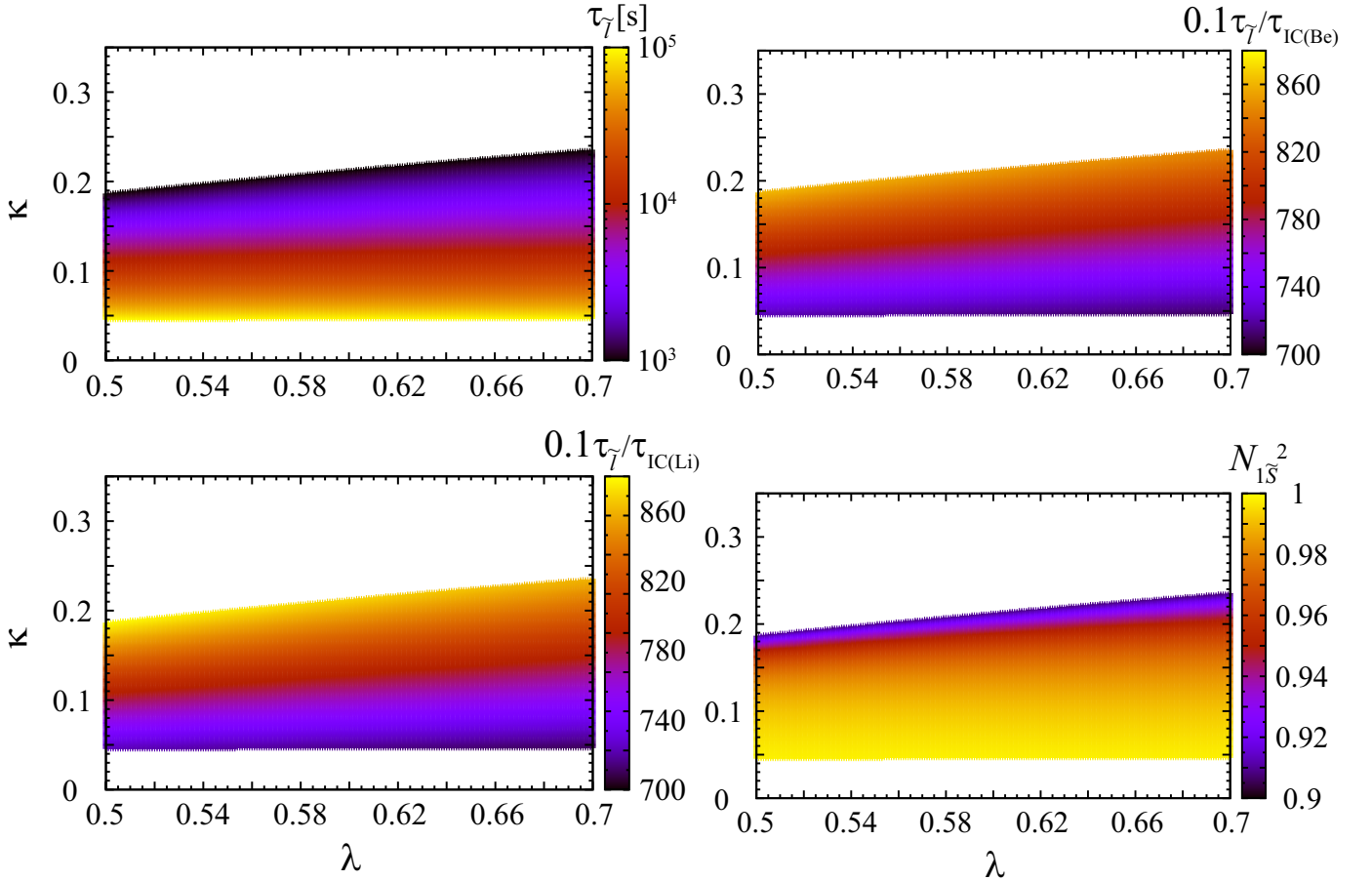
Figure 4.5: The distribution of the quantities relevant to the requirements, Eqs. (4.13)-(4.15), in the favored region from $c_e = 5 \times 10^{-10}$ and $\tan\beta = 2$. The color bar in each panel shows τ_l (top-left), $0.1\tau_{\tilde{l}}/\tau_{\mathrm{IC}}$ for $(^7\mathrm{Be}\,\tilde{l}^-) \rightarrow\ ^7\mathrm{Li} + \tilde{\chi}_1^0 + \nu_l$ (top-right), $0.1\tau_{\tilde{l}}/\tau_{\mathrm{IC}}$ for $(^7\mathrm{Li}\,\tilde{l}^-) \rightarrow\ ^7\mathrm{He} + \tilde{\chi}_1^0 + \nu_l$ (bottom-left), and $N_{1\tilde{S}}^2$ (bottom-right).

Table 4.3: Benchmark points in the favored region of Fig. 4.4 for $\tan\beta = 2$.

Parameters	SL-1	SL-2	SL-3	SL-4
c_e	$5{\times}10^{-10}$	2×10^{-10}	5×10^{-10}	5×10^{-10}
λ	0.68	0.68	0.695	0.68
κ	0.22	0.22	0.22	0.215

Table 4.4: Spectra and observables at each point (see Tab. 4.3). All the dimensionful values are shown in GeV. The top rows show input parameters. SL-1 and SL-2 give common results since we omit small flavor mixing of the slepton. The middle rows show output spectra. The bottom rows show relic density of the lightest neutralino, spin-independent cross section between the lightest neutralino and nucleon, the SUSY contribution to the muon anomalous magnetic moment, and the branching ratios of rare decays $B_s \to \mu^+\mu^-$ and $b \to s\gamma$, and couplings Eqs. (4.8) and (4.9) from top to bottom.

| Input	SL-1, SL-2	SL-3	SL-4
M_2	1000.0	1000.0	1000.0
A_t	-1500.0	-1800.0	-2800.0
$m_{\tilde{L}_3}$	356.86	357.93	361.23
$m_{\tilde{E}_3}$	353.36	353.96	355.84
$m_{\tilde{Q}_3}$	1000.0	1000.0	1000.0
λ	0.6800	0.6950	0.6800
κ	0.2200	0.2200	0.2150
A_λ	1120.0	1180.0	1100.0
A_κ	-10.000	-10.000	-10.000
μ_{eff}	527.17	537.90	538.91
$\tan\beta$	2.0000	2.0000	2.0000
Output			
h_1^0	127.13	126.66	124.36
h_2^0	370.96	354.77	369.96
h_3^0	1303.6	1348.4	1313.9
a_1^0	152.72	262.92	150.73
a_2^0	1303.8	1348.8	1313.8
$H^\pm$	1295.0	1339.0	1304.3
$\tilde{t}_1$	696.15	660.83	528.37
$\tilde{t}_2$	959.18	983.66	1059.9
$\tilde{\tau}_1$	350.10	350.10	350.10
$\tilde{\tau}_2$	363.35	364.99	370.03
$\tilde{\chi}_1^0$	350.00	350.00	350.00
$\tilde{\chi}_2^0$	468.58	471.30	471.37
$\tilde{\chi}_3^0$	547.60	558.78	559.13
$\tilde{\chi}_4^0$	553.96	561.55	562.02
$\tilde{\chi}_5^0$	1013.7	1014.1	1014.1
$\Omega_{\tilde{\chi}_1^0} h^2$	0.12684	0.12672	0.12489
$\sigma_{\text{SI}}[\text{cm}^2]$	1.8983×10^{-45}	3.1914×10^{-45}	1.7546×10^{-45}
δa_μ	$1.0707 \times 10^{-10}(>3\sigma)$	$1.1346 \times 10^{-10}(>3\sigma)$	$1.3675 \times 10^{-10}(>3\sigma)$
$\text{Br}(B_s^0 \to \mu^+\mu^-)$	$3.5373 \times 10^{-9}(1\sigma)$	$3.5374 \times 10^{-9}(1\sigma)$	$3.5365 \times 10^{-9}(1\sigma)$
$\text{Br}(b \to s\gamma)$	$3.2030 \times 10^{-4}(2\sigma)$	$3.1658 \times 10^{-4}(2\sigma)$	$3.0507 \times 10^{-4}(2\sigma)$
$G_{\text{L}\tau}/c_\tau$	0.0012549	0.0013068	0.0012826
$G_{\text{R}\tau}/c_\tau$	0.030877	0.029833	0.029090
$G_{\text{L}e}/c_e$	0.0026200	0.0025373	0.0024746
$G_{\text{R}e}/c_e$	0.029853	0.028910	0.028196
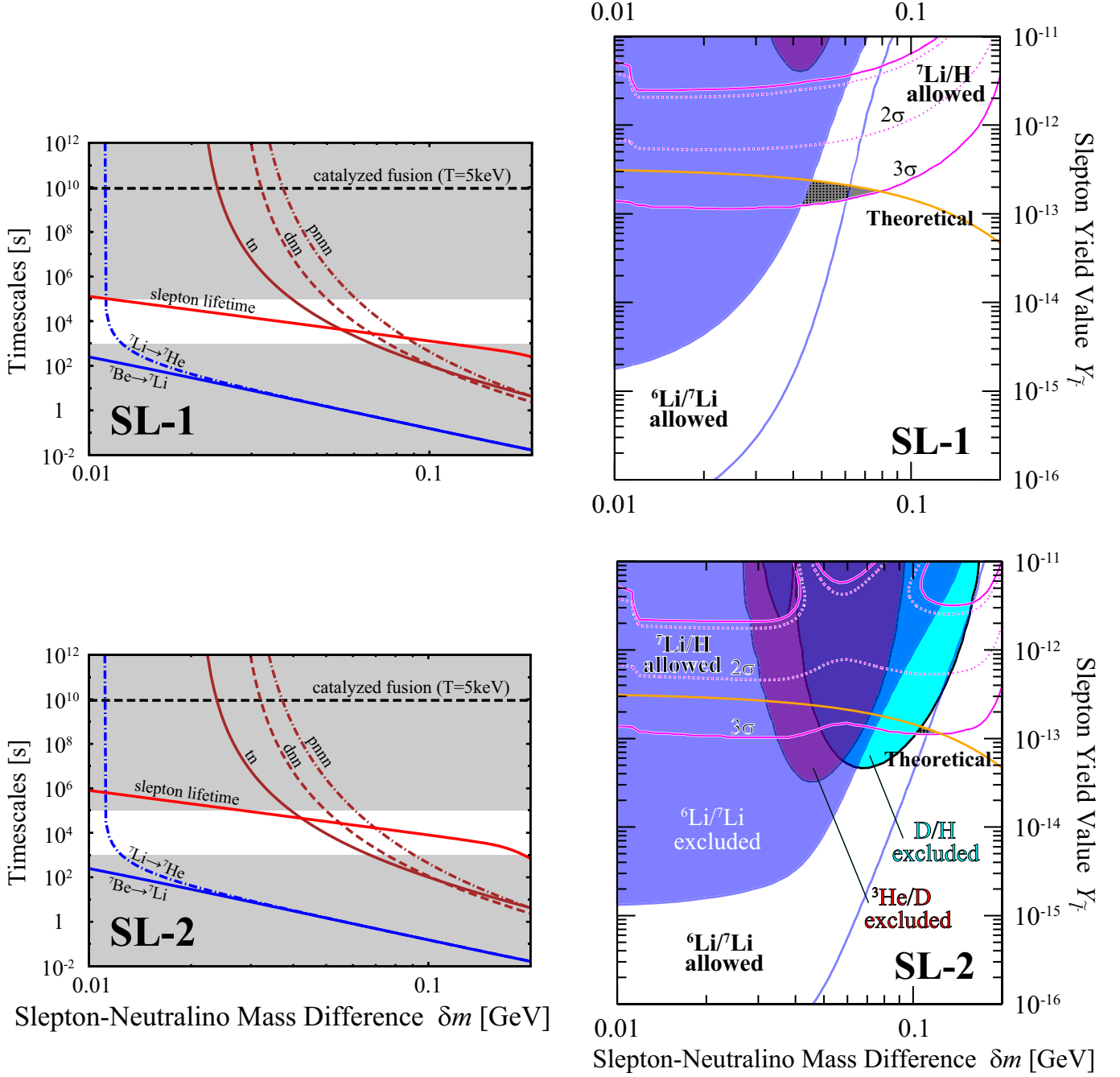
Figure 4.6: The left panels show the slepton lifetime $\tau_{\tilde{l}}$ (red-solid line; "slepton lifetime"), the timescales of the internal conversion processes (3.11a) (blue-solid line; "^{7}Be→^{7}Li"), (3.11b) (blue-dash-dotted line; "^{7}Li→^{7}He"), the ^{4}He spallation processes (3.18a) (brown-solid line; "tn"), (3.18b) (brown-dashed line; "dnn"), and (3.18c) (brown-dash-dotted line; "pnnn"), as a function of the mass difference between the slepton and the neutralino at SL-1 (top panel) and SL-2 (bottom panel). We also show the timescale of the catalyzed fusion (3.16) at the temperature $T = 5$ keV (5×10^4 s) when (^{4}He $\tilde{l}^-$) is formed as horizontal black-dashed line. In the shaded regions, Eq. (4.13) is not satisfied. The right panels show the allowed regions from observational light element abundances on δm-$Y_{\tilde{l}^-}$ plane at SL-1 (top panel) and SL-2 (bottom panel). The regions surrounded by magenta-dotted(-solid) lines are allowed by observed ^{7}Li/H abundance at $2\sigma(3\sigma)$. The regions between the blue-solid line and the blue region are allowed by observed ^{6}Li/^{7}Li abundance at 2σ. The orange-solid lines ("Theoretical") represent the yield value of the slepton when the BBN starts as a function of the mass difference. The colored regions are excluded for ^{6}Li/^{7}Li (blue region; "^{6}Li/^{7}Li excluded"), ^{3}He/D (red region; "^{3}He/D excluded"), and D/H (cyan region; "D/H excluded"), respectively. The shadowed and dotted regions are allowed by only ^{7}Li/H (3σ) and both ^{7}Li/H (3σ) and ^{6}Li/^{7}Li (2σ), respectively.
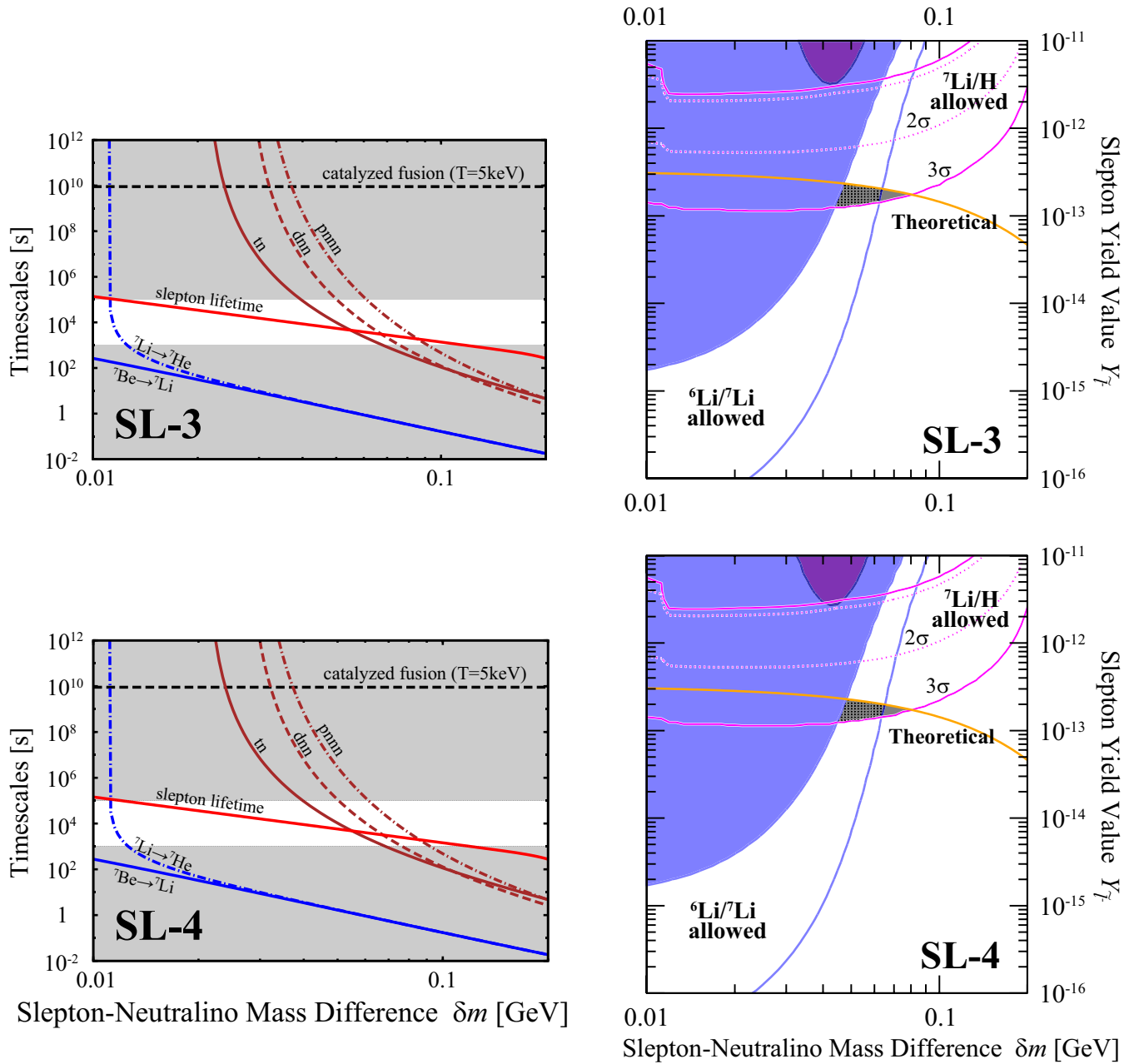
Figure 4.6: The results at SL-3 (top panels) and SL-4 (bottom panels) are shown. The meanings of the lines and regions are same as those in the previous page.

4.3.3 Bino-like neutralino LSP; large λ-κ region with small $\tan\beta$

We finally show the results in the third case where the neutralino LSP is bino-like with relatively large λ, κ and small $\tan\beta$. In this case, the first term is dominant in the couplings Eqs. (4.8) and (4.9), and they hardly depend on the parameters, $\lambda, \kappa, \tan\beta, \mu_{\mathrm{eff}}, M_1$, and M_2, since $N_{1\tilde{B}}^2 \simeq 1$. Therefore, we do not have to check the dependence on these parameters of the slepton lifetime and relevant timescales of the exotic BBN reactions (3.11) and (3.18) since they also do not depend on these parameters.

Benchmark points

We take four reference points in the favored region for $\tan\beta = 2$ as shown in Table 4.5. Table 4.6 shows the spectra and observables at these points. All the dimensionful values are represented in GeV. The top rows show input parameters and the middle rows show output spectra. Every points give the observed Higgs mass. As in the results of Sec. 4.3.2, observed Higgs mass is obtained by virtue of large contribution of the tree terms. In this respect, the result is completely different from the case with bino-like neutralino in the MSSM, where the 1-loop contribution lifts up the Higgs mass.

In the bottom rows, we show relic density of the lightest neutralino, spin-independent cross section between the lightest neutralino and nucleon, the SUSY contribution to the muon anomalous magnetic moment, and the branching ratios of rare decays $B_s \to \mu^+\mu^-$ and $b \to s\gamma$, from top to bottom. At each point, the dark matter relic density is in range of the measured value [29]. The spin-independent cross sections are about one order of magnitude smaller than those at points we chose in the previous section, and below the present experimental bound. The calculated values of δa_μ at the points are below 3σ range which is caused by small $\tan\beta$. For the branching ratio of $B_s \to \mu^+\mu^-$ and $b \to s\gamma$, we obtained the values within 1σ and 2σ, respectively.

BBN results at the benchmark points

The left panels in Fig. 4.7 show the slepton lifetime $\tau_{\tilde{l}}$ (red-solid line; "slepton lifetime"), the timescales of the internal conversion processes (3.11a) (blue-solid line; "^{7}Be$\to^7$Li"), (3.11b) (blue-dash-dotted line; "^{7}Li$\to^7$He"), the ^{4}He spallation processes (3.18a) (brown-solid line; "tn"), (3.18b) (brown-dashed line; "dnn"), and (3.18c) (brown-dash-dotted line; "pnnn"), as a function of the mass difference between the slepton NLSP and the neutralino LSP at BL-1, BL-2, BL-3, and BL-4 from top to bottom, respectively. The horizontal black-dashed line represents the timescale of the catalyzed fusion process (3.16) [55] at the temperature $T = 5$ keV (5×10^4 s) when (^{4}He $\tilde{l}^-$) is formed. In the right panels horizontal axis is the mass difference between the slepton NLSP and the neutralino LSP, and vertical axis is the yield value of the slepton at the beginning of the BBN.

We show the allowed regions in the right panels of Fig. 4.7 which we obtain by comparing theoretical values to observational ones for light element abundances at BL-1, BL-2, BL-3, and BL-4 from top to bottom, respectively. The lines and regions are the same as those in the previous section. At BL-1, BL-2, and BL-3, we obtain allowed region only for ^{7}Li/H (3σ) while at BL-4, that for ^{6}Li/^{7}Li (2σ) is also obtained simultaneously.

At BL-2 and BL-3, κ and λ are small compared with those at BL-1, respectively. As was mentioned in the beginning of this section, the slepton lifetime and timescales of the internal conversion processes (3.11) and the ^{4}He spallation processes (3.18) hardly depend on the NMSSM parameters. This is the reason why almost no difference exists among the results at BL-1, BL-2, and BL-3. The couplings $G_{\mathrm{L}f}$ and $G_{\mathrm{R}f}$ are large compared with those in the singlino-like LSP scenario, and hence the timescales of the internal conversion processes (3.11) and the ^{4}He spallation processes (3.18) are one or two order of magnitude shorter than those in the singlino-like LSP scenario. Therefore, the observed abundance of ^{7}Li/H is obtained in smaller slepton yield value compared with the singlino-like LSP scenarios, Fig. 4.4 and 4.6. In addition, the excluded regions by ^{3}He/D and D/H lie downward compared to those of

the singlino-LSP secnario (e.g., compare the results at SL-2 and BL-1). Indeed, the results at BL-1, BL-2, and BL-3 are almost same as the result in the MSSM, Fig. 3 in Ref. [7], where the same values for $c_e, m_{\tilde{\chi}_1^0}, \sin\theta_f$ and CP-violating phase are used.

Only at BL-4, tiny flavor mixing exists. This result is similar to that in the MSSM, Fig. 4 (middle panel) in Ref. [8], where same values for $c_e, m_{\tilde{\chi}_1^0}, \sin\theta_f$ and CP-violating phase are used.

Table 4.5: Benchmark points on λ-κ plane for $\tan\beta = 2$.

Parameters	BL-1	BL-2	BL-3	BL-4
c_e	0	0	0	5×10^{-11}
λ	0.68	0.68	0.6	0.68
κ	0.32	0.2	0.32	0.32

Table 4.6: Spectra and observables at each point (see Tab. 4.5). All the dimensionful values are shown in GeV. The top rows show input parameters. BL-1 and BL-4 give common results since we omit small flavor mixing of the slepton. The middle rows show output spectra. The bottom rows show relic density of the lightest neutralino, spin-independent cross section between the lightest neutralino and nucleon, the SUSY contribution to the muon anomalous magnetic moment, and the branching ratios of rare decays $B_s \to \mu^+\mu^-$ and $b \to s\gamma$, and couplings Eqs. (4.8) and (4.9) from top to bottom.

| Input	BL-1, BL-4	BL-2	BL-3
M_2	713.36	713.25	712.97
A_t	-1500.0	-1500.0	-1500.0
$m_{\tilde{L}_3}$	359.32	359.32	359.32
$m_{\tilde{E}_3}$	354.76	354.76	354.76
$m_{\tilde{Q}_3}$	1000.0	1000.0	1000.0
λ	0.6800	0.6800	0.6000
κ	0.3200	0.2000	0.3200
A_λ	1000.0	1480.0	1500.0
A_κ	-100.00	-100.00	-100.00
μ_{eff}	900.00	900.00	900.00
$\tan\beta$	2.0000	2.0000	2.0000
Output			
h_1^0	125.23	126.51	124.35
h_2^0	844.57	552.89	960.06
h_3^0	1793.5	1983.6	2115.8
a_1^0	372.60	289.22	379.68
a_2^0	1792.3	1983.7	2114.5
$H^\pm$	1783.8	1974.3	2108.5
$\tilde{t}_1$	853.37	853.41	853.51
$\tilde{t}_2$	1132.1	1132.1	1132.2
$\tilde{\tau}_1$	350.10	350.10	350.10
$\tilde{\tau}_2$	367.13	367.13	367.13
$\tilde{\chi}_1^0$	350.00	350.00	350.00
$\tilde{\chi}_2^0$	696.36	534.28	697.51
$\tilde{\chi}_3^0$	842.69	699.36	906.34
$\tilde{\chi}_4^0$	908.00	909.78	914.24
$\tilde{\chi}_5^0$	944.68	934.66	984.08
$\Omega_{\tilde{\chi}_1^0} h^2$	0.11956	0.11964	0.11968
$\sigma_{\text{SI}}[\text{cm}^2]$	3.6870×10^{-46}	3.7874×10^{-46}	3.7116×10^{-46}
δa_μ	$1.3398 \times 10^{-10} (> 3\sigma)$	$1.3370 \times 10^{-10} (> 3\sigma)$	$1.3296 \times 10^{-10} (> 3\sigma)$
$\text{Br}(B_s^0 \to \mu^+\mu^-)$	$3.5381 \times 10^{-9}(1\sigma)$	$3.5382 \times 10^{-9}(1\sigma)$	$3.5383 \times 10^{-9}(1\sigma)$
$\text{Br}(b \to s\gamma)$	$3.1907 \times 10^{-4}(2\sigma)$	$3.1754 \times 10^{-4}(2\sigma)$	$3.1668 \times 10^{-4}(2\sigma)$
$G_{\text{L}\tau}/c_\tau$	0.15080	0.15080	0.15076
$G_{\text{R}\tau}/c_\tau$	0.40310	0.40310	0.40313
$G_{\text{L}e}/c_e$	0.15108	0.15108	0.15108
$G_{\text{R}e}/c_e$	0.40289	0.40289	0.40289
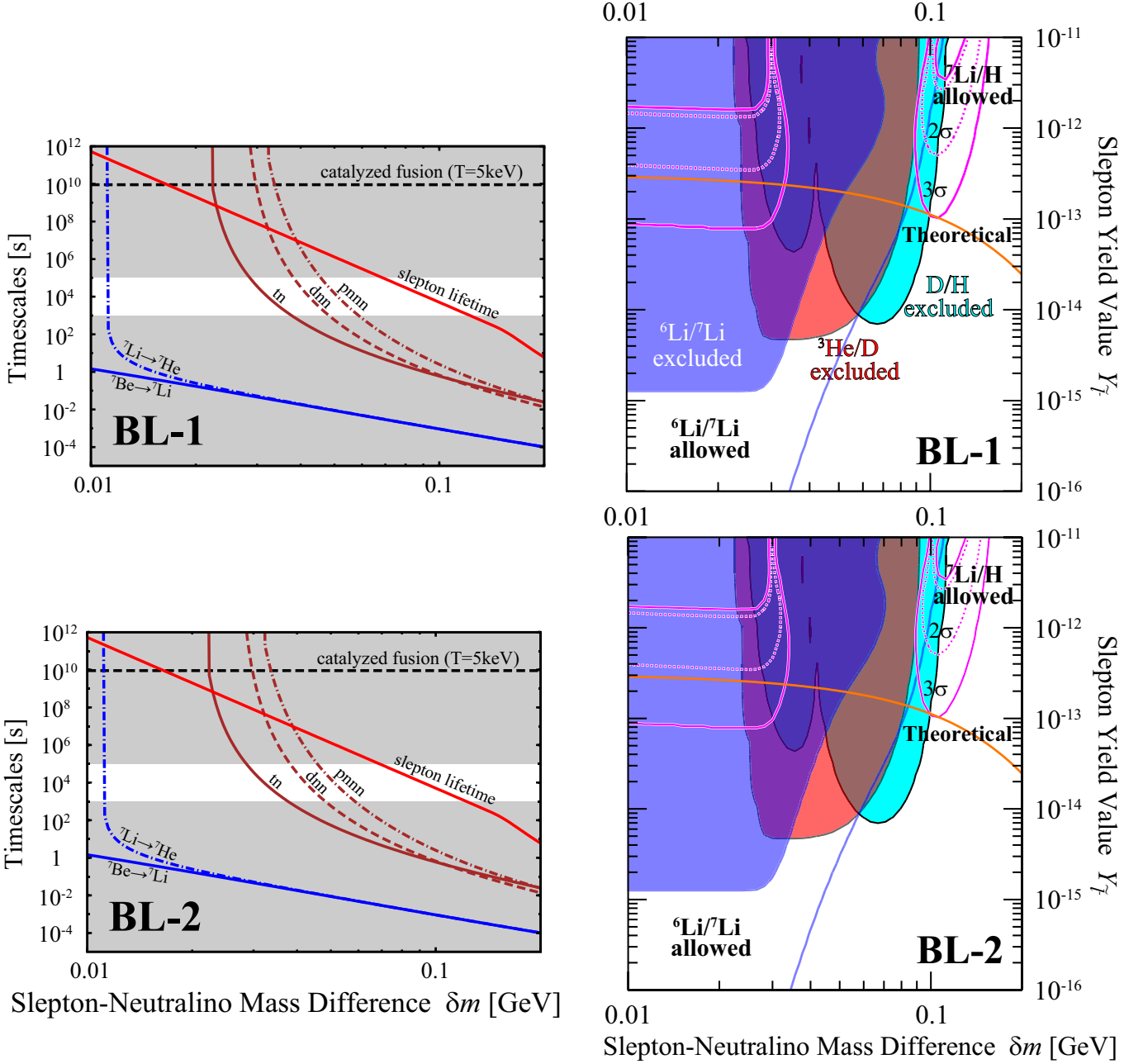
Figure 4.7: The left panels show the slepton lifetime $\tau_{\tilde{l}}$ (red-solid line; "slepton lifetime"), the timescales of the internal conversion processes, Eqs. (3.11a) (blue-solid line; "^{7}Be$\to^7$Li") and (3.11b) (blue-dash-dotted line; "^{7}Li$\to^7$He"), the ^{4}He spallation processes, Eqs. (3.18a) (brown-solid line; "tn"), (3.18b) (brown-dashed line; "dnn"), and (3.18c) (brown-dash-dotted line; "pnnn"), as a function of the mass difference between the slepton and the neutralino at BL-1 (top panel) and BL-2 (bottom panel). We also show the timescale of the catalyzed fusion (3.16) at the temperature $T = 5$ keV (5×10^4 s) when (^{4}He $\tilde{l}^-$) is formed as horizontal black-dashed line. In the shaded regions, Eq. (4.13) is not satisfied. The right panels show the allowed regions from observational light element abundances on δm-$Y_{\tilde{l}^-}$ plane at BL-1 (top panel) and BL-2 (bottom panel). The regions surrounded by magenta-dotted(-solid) lines are allowed by observed ^{7}Li/H abundance at $2\sigma(3\sigma)$. The regions between the blue-solid line and the blue region are allowed by observed ^{6}Li/^{7}Li abundance at 2σ. The orange-solid lines ("Theoretical") represent the yield value of the slepton when the BBN starts as a function of the mass difference. The colored regions are excluded for ^{6}Li/^{7}Li (blue region; "^{6}Li/^{7}Li excluded"), ^{3}He/D (red region; "^{3}He/D excluded"), and D/H (cyan region; "D/H excluded"), respectively. The shadowed and dotted regions are allowed by only ^{7}Li/H (3σ) and both ^{7}Li/H (3σ) and ^{6}Li/^{7}Li (2σ), respectively.
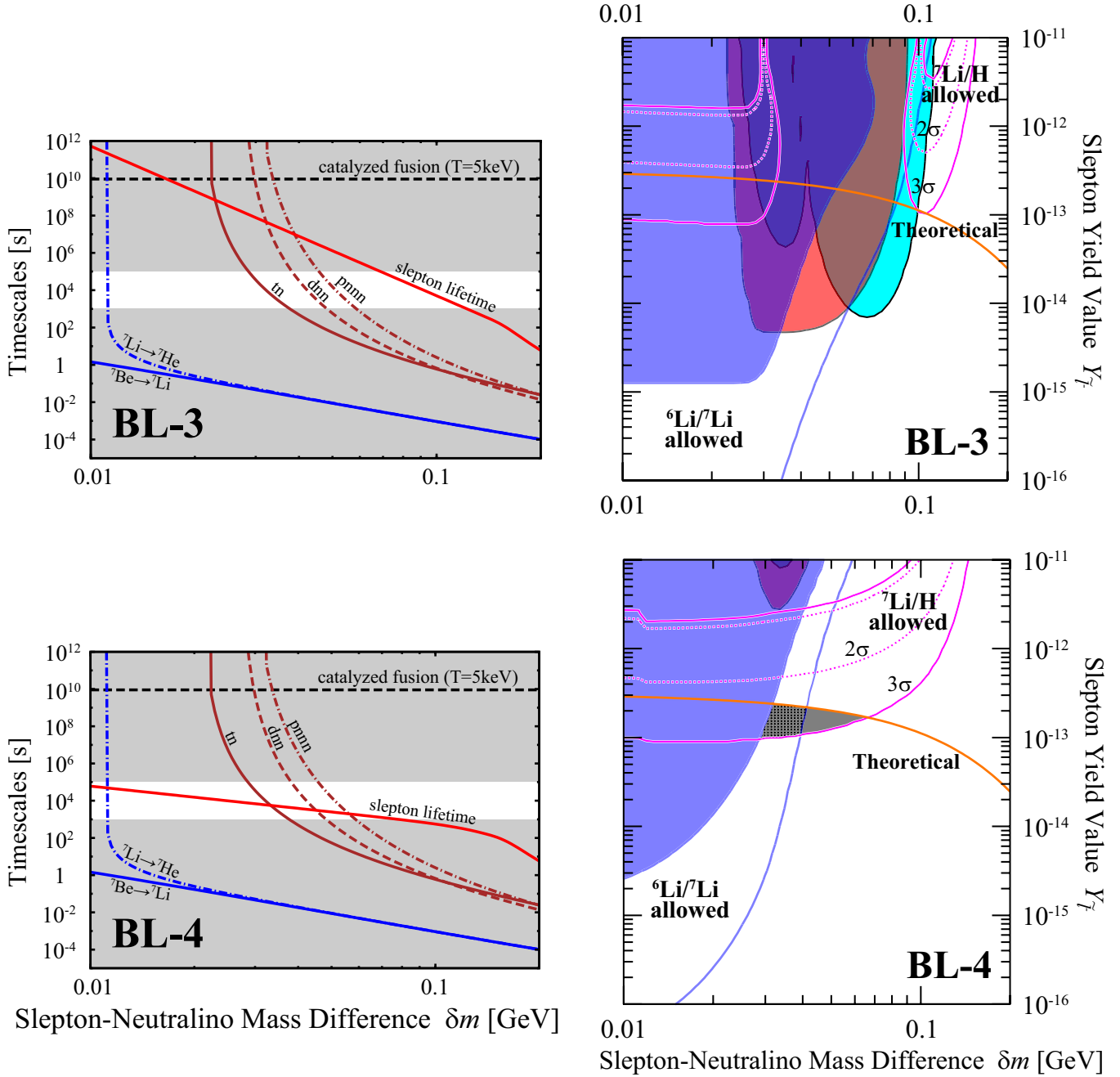
Figure 4.7: The results at BL-3 (top panels) and BL-4 (bottom panels) are shown. The meanings of the lines and regions are same as those in the previous page.

Chapter 5

Summary

We have considered a scenario of the NMSSM where the slepton NLSP is long-lived due to the degenerated masses between the NLSP and the neutralino LSP. In the scenario, we have confirmed that the ^{7}Li and ^{6}Li problems can be solved, and observed dark matter relic density and the Higgs mass can be obtained simultaneously.

In Chap. 2, we have explained three shortcomings that we focus on in this study: lepton flavor violation, dark matter, and light element abundances.

In Chap. 3, we have considered the secnario in the MSSM. In the scenario, the slepton NLSP is long-lived so that it can survive until the BBN era due to small mass difference between the NLSP and the LSP. Then the sleptons can form bound states with nuclei, and exotic nuclear reactions are induced by the bound state effects. We have taken three exotic reactions into account. First one is the internal conversion processes where the sleptons form bound states with ^{7}Be and ^{7}Li and the nuclei are converted into lighter ones to reduce ^{7}Li abundance, and solve the ^{7}Li problem. Second one is the catalyzed fusion process where the slepton forms bound state with ^{4}He. This process produces ^{6}Li, and thus can solve the ^{6}Li problem. This can give upper bound on the lifetime of the slepton, since the time scale of this process is longer than those of the internal conversion processes, and the catalyzed fusion process can overproduce ^{6}Li. The final one is the ^{4}He spallation processes where the sleptons form bound states with ^{4}He and they are destroyed into T, D, p, and n. The overproduction of the spallation products can ruin successful BBN. We have analyzed the yield value and the slepton lifetime with the intergenerational mixings as well as the relic abundances of the light elements including above exotic processes. Then we have found allowed regions for light element abundances and the flavor mixing parameters of the slepton.

In Chap. 4, we extended the MSSM into the NMSSM and have confirmed that the scenario we had introduced is also hold in the NMSSM. We specifically considered the case where the neutralino is the stable LSP and the lightest slepton is the NLSP, and where the mass difference of the two is so tiny that the slepton becomes long-lived enough to survive until the time of the nucleosynthesis in the early universe. The sleptons interact with the synthesized nuclei and turn into the LSP staying until today as dark matter particles, while the light elements alter their relic abundance.

We searched for benchmark set of parameters that can successfully drive this scenario and simultaneously can reproduce the mass of Higgs particle within (125.6 ± 3.0) GeV. Three cases of benchmark parameters are presented: (1) Singlino-like neutralino, small λ-κ with large $\tan\beta$, (2) Singlino-like neutralino, large λ-κ with small $\tan\beta$, and (3) Bino-like neutralino, large λ-κ with small $\tan\beta$. In every three cases, we found the successful benchmark values of (c_e, λ, κ) We confirmed that they lead to the permissible abundance of dark matter and are consistent with other experimental bounds (Tables 4.2, 4.4, and 4.6).

We then traced the BBN reaction network including the exotic nuclear reactions. We employed $Y_{\tilde{l}^-}$ (slepton yield value)-δm (LSP-NLSP mass difference) parameter plane to present the regions of

parameters that can account for the observed abundance of light elements. These results are illustrated in terms of timescales for the relevant exotic BBN reactions. The slepton need to be long-lived enough to form the bound state with ^{7}Be. The coupling G_{L,R_τ} should be however large enough so that the internal conversion processes occur sufficiently. The other important processes are the catalyzed fusion process and the ^{4}He spallation processes, both of which arise from $(^4$He $\tilde{l}^-)$. Although the overproduction of the light elements produced through the processes are not desired, the suitable amount of ^{6}Li created from the catalyzed fusion process is favored to achieve the observed abundance of ^{6}Li. From this, we can give the upper limit on the slepton lifetime. Furthermore, we have to consider the fact that the ^{4}He spallation processes, in general, work more efficiently than the catalyzed fusion process. For such a reason, we need the short lifetime of slepton not to make the bound state with ^{4}He. Thus, the slepton is desired to make the bound state with ^{7}Be and not with ^{4}He. Incidentally we can obtain suitable ^{6}Li abundance from the catalyzed fusion process with adequate slepton lifetime, since the observed abundance is quite tiny as explained around Eq. (4.28). As a result, the upper and lower limits for the slepton lifetime are imposed. In the case of (1), the specific relation between λ and κ is necessary to make the couplings G_{L,R_τ} large so that ^{7}Be is reduced by the internal conversion processes. Indeed, we tune the parameters λ and κ to make $\mu_\kappa^2 - \mu_{\rm eff}^2$ small, that is, G_{L,R_τ} large at SS-1. Even under the circumstances, we also need a sizable flavor mixing, c_e, in order to make the slepton lifetime short and hence reduce a number of $(^4$He $\tilde{l}^-)$. Thus we obtain the allowed region at SS-1. On the contrary, at SS-2 the flavor mixing c_e is small and hence the slepton lifetime becomes longer. It shifts the allowed region to larger δm. Outside of the tuned parameter region for λ and κ, $G_{L,R}$ can be rapidly small so that the allowed region becomes small (SS-4) (Fig. 4.4). In the case of (2), due to large λ and κ, $G_{L,R}$ are large so that the internal conversion processes occur efficiently. In the same reason as (1), a suitable flavor mixings are also necessary to avoid the extra amount of $(^4$He $\tilde{l}^-)$ (Fig. 4.6), otherwise, we may miss the allowed region (SL-2). In the case of (3), the coupling G_{L,R_τ} does not depend mainly on λ and κ. Therefore, the results of the case (3) are same as in the case of the MSSM (Fig. 4.7).

We conclude that our scenario successfully works in the NMSSM and can simultaneously account for the abundance of dark matter, that of light elements, and the mass of Higgs particle. Since all the three cases we considered here are consistent to the present phenomenological bounds, they should be distinguished through the characteristic signals of accelerator experiments. Search for such signals are left for future works.

Acknowledgement

I owe my deepest gratitude to my supervisor, Professor Joe Sato, for instructing me on research and many kinds of seminars and lectures over the years. I have learned what I need to proceed research through the instructions, and I could not finish this thesis without it. I studied many basics from lectures and seminars by Professor Yoshiaki Tanii. Professor Naoya Inoue and Professor Kazuo Hida asked me many questions with interest. I would like to express my gratitude to them.

I am deeply grateful to my collaborators, Kazunori Kohri, Masafumi Koike, Yasufumi Konishi, Takashi Shimomura, Kenichi Sugai and Masato Yamanaka, for fruitful discussion and suggestions. They spared time to discuss in many times, and encourage me to proceed research.

I would like to thank all people I met in the laboratory of elementary particle physics, all my friends, and my family who support and encourage my life in the laboratory over the years. I have spent fulfilling research life thanks to them.

Bibliography

[1] G. Aad *et al.* [ATLAS Collaboration], Phys. Lett. B **716** (2012) 1 [arXiv:1207.7214 [hep-ex]].

[2] S. Chatrchyan *et al.* [CMS Collaboration], Phys. Lett. B **716** (2012) 30 [arXiv:1207.7235 [hep-ex]].

[3] J. E. Kim and H. P. Nilles, Phys. Lett. B **138** (1984) 150.

[4] T. Jittoh, K. Kohri, M. Koike, J. Sato, T. Shimomura and M. Yamanaka, Phys. Rev. D **76** (2007) 125023 [arXiv:0704.2914 [hep-ph]].

[5] T. Jittoh, K. Kohri, M. Koike, J. Sato, T. Shimomura and M. Yamanaka, Phys. Rev. D **78** (2008) 055007 [arXiv:0805.3389 [hep-ph]].

[6] T. Jittoh, K. Kohri, M. Koike, J. Sato, T. Shimomura and M. Yamanaka, Phys. Rev. D **82** (2010) 115030 [arXiv:1001.1217 [hep-ph]].

[7] T. Jittoh, K. Kohri, M. Koike, J. Sato, K. Sugai, M. Yamanaka and K. Yazaki, Phys. Rev. D **84** (2011) 035008 [arXiv:1105.1431 [hep-ph]].

[8] K. Kohri, S. Ohta, J. Sato, T. Shimomura and M. Yamanaka, Phys. Rev. D **86** (2012) 095024 [arXiv:1208.5533 [hep-ph]].

[9] J. Melendez and I. Ramirez, Astrophys. J. **615** (2004) L33 [astro-ph/0409383].

[10] M. Asplund, D. L. Lambert, P. E. Nissen, F. Primas and V. V. Smith, Astrophys. J. **644** (2006) 229 [arXiv:astro-ph/0510636].

[11] Y. Konishi, S. Ohta, J. Sato, T. Shimomura, K. Sugai and M. Yamanaka, arXiv:1309.2067 [hep-ph].

[12] A. Abada, arXiv:1310.3800 [hep-ph].

[13] J. Adam *et al.* [MEG Collaboration], arXiv:1303.0754 [hep-ex].

[14] A. M. Baldini, F. Cei, C. Cerri, S. Dussoni, L. Galli, M. Grassi, D. Nicolo and F. Raffaelli *et al.*, arXiv:1301.7225 [physics.ins-det].

[15] B. Aubert *et al.* [BaBar Collaboration], Phys. Rev. Lett. **104** (2010) 021802 [arXiv:0908.2381 [hep-ex]].

[16] B. Meadows, M. Blanke, A. Stocchi, A. Drutskoy, A. Cervelli, M. Giorgi, A. Lusiani and A. Perez *et al.*, arXiv:1109.5028 [hep-ex].

[17] U. Bellgardt *et al.* [SINDRUM Collaboration], Nucl. Phys. B **299** (1988) 1.

[18] A. Blondel, A. Bravar, M. Pohl, S. Bachmann, N. Berger, M. Kiehn, A. Schoning and D. Wiedner *et al.*, arXiv:1301.6113 [physics.ins-det].

[19] K. Hayasaka, K. Inami, Y. Miyazaki, K. Arinstein, V. Aulchenko, T. Aushev, A. M. Bakich and A. Bay *et al.*, Phys. Lett. B **687** (2010) 139 [arXiv:1001.3221 [hep-ex]].

[20] C. Dohmen *et al.* [SINDRUM II. Collaboration], Phys. Lett. B **317** (1993) 631.

[21] R. J. Barlow, Nucl. Phys. Proc. Suppl. **218** (2011) 44.

[22] W. H. Bertl *et al.* [SINDRUM II Collaboration], Eur. Phys. J. C **47** (2006) 337.

[23] Y. G. Cui *et al.* [COMET Collaboration], KEK-2009-10.

[24] F. Zwicky, Helv. Phys. Acta **6** (1933) 110.

[25] T. S. van Albada, J. N. Bahcall, K. Begeman and R. Sancisi, Astrophys. J. **295** (1985) 305.

[26] D. Clowe, M. Bradac, A. H. Gonzalez, M. Markevitch, S. W. Randall, C. Jones and D. Zaritsky, Astrophys. J. **648** (2006) L109 [astro-ph/0608407].

[27] A. Refregier, Ann. Rev. Astron. Astrophys. **41** (2003) 645 [astro-ph/0307212].

[28] J. A. Tyson, G. P. Kochanski and I. P. Dell'Antonio, Astrophys. J. **498** (1998) L107 [astro-ph/9801193].

[29] P. A. R. Ade *et al.* [Planck Collaboration], arXiv:1303.5076 [astro-ph.CO].

[30] M. W. Goodman and E. Witten, Phys. Rev. D **31** (1985) 3059.

[31] P. Cushman, C. Galbiati, D. N. McKinsey, H. Robertson, T. M. P. Tait, D. Bauer, A. Borgland and B. Cabrera *et al.*, arXiv:1310.8327 [hep-ex].

[32] D. S. Akerib *et al.* [LUX Collaboration], arXiv:1310.8214 [astro-ph.CO].

[33] E. Armengaud *et al.* [EDELWEISS Collaboration], Phys. Lett. B **702** (2011) 329 [arXiv:1103.4070 [astro-ph.CO]].

[34] Z. Ahmed *et al.* [CDMS-II Collaboration], Science **327** (2010) 1619 [arXiv:0912.3592 [astro-ph.CO]].

[35] D. Y. .Akimov, H. M. Araujo, E. J. Barnes, V. A. Belov, A. Bewick, A. A. Burenkov, V. Chepel and A. Currie *et al.*, Phys. Lett. B **709** (2012) 14 [arXiv:1110.4769 [astro-ph.CO]].

[36] E. Aprile *et al.* [XENON100 Collaboration], Phys. Rev. Lett. **107** (2011) 131302 [arXiv:1104.2549 [astro-ph.CO]].

[37] E. Aprile *et al.* [XENON100 Collaboration], Phys. Rev. Lett. **109** (2012) 181301 [arXiv:1207.5988 [astro-ph.CO]].

[38] C. E. Aalseth *et al.* [CoGeNT Collaboration], Phys. Rev. D **88** (2013) 012002 [arXiv:1208.5737 [astro-ph.CO]].

[39] Z. Ahmed *et al.* [CDMS-II Collaboration], Phys. Rev. Lett. **106** (2011) 131302 [arXiv:1011.2482 [astro-ph.CO]].

[40] R. Agnese, et al., submitted to: Phys. Rev. Lett. (2013).

[41] G. Angloher, M. Bauer, I. Bavykina, A. Bento, C. Bucci, C. Ciemniak, G. Deuter and F. von Feilitzsch *et al.*, Eur. Phys. J. C **72** (2012) 1971 [arXiv:1109.0702 [astro-ph.CO]].

[42] R. Bernabei *et al.* [DAMA Collaboration], Eur. Phys. J. C **56** (2008) 333 [arXiv:0804.2741 [astro-ph]].

[43] C. Savage, G. Gelmini, P. Gondolo and K. Freese, JCAP **0904** (2009) 010 [arXiv:0808.3607 [astro-ph]].

[44] M. Pospelov and J. Pradler, Ann. Rev. Nucl. Part. Sci. **60** (2010) 539 [arXiv:1011.1054 [hep-ph]].

[45] J. Beringer *et al.* [Particle Data Group Collaboration], Phys. Rev. D **86** (2012) 010001.

[46] F. Spite and M. Spite, Astron. Astrophys. **115** (1982) 357.

[47] K. Griest and D. Seckel, Phys. Rev. D **43** (1991) 3191.

[48] J. Edsjo and P. Gondolo, Phys. Rev. D **56** (1997) 1879

[49] T. Jittoh, J. Sato, T. Shimomura and M. Yamanaka, Phys. Rev. D **73** (2006) 055009 [Erratum-ibid. D **87** (2013) 019901] [hep-ph/0512197].

[50] M. Kamimura, Y. Kino and E. Hiyama, Prog. Theor. Phys. **121**, 1059 (2009) [arXiv:0809.4772 [nucl-th]].

[51] K. Kohri and T. Takahashi, Phys. Lett. B **682** (2010) 337 [arXiv:0909.4610 [hep-ph]].

[52] C. Bird, K. Koopmans and M. Pospelov, Phys. Rev. D **78**, 083010 (2008) [arXiv:hep-ph/0703096].

[53] E. Komatsu *et al.* [WMAP Collaboration], Astrophys. J. Suppl. **192**, 18 (2011) [arXiv:1001.4538 [astro-ph.CO]].

[54] M. Pospelov, Phys. Rev. Lett. **98**, 231301 (2007) [arXiv:hep-ph/0605215].

[55] K. Hamaguchi, T. Hatsuda, M. Kamimura, Y. Kino and T. T. Yanagida, Phys. Lett. B **650** (2007) 268 [arXiv:hep-ph/0702274].

[56] U. Ellwanger and C. Hugonie, Mod. Phys. Lett. A **22** (2007) 1581 [hep-ph/0612133].

[57] U. Ellwanger, J. F. Gunion and C. Hugonie, JHEP **0502** (2005) 066 [hep-ph/0406215].

[58] U. Ellwanger and C. Hugonie, Comput. Phys. Commun. **175** (2006) 290 [hep-ph/0508022].

[59] G. Belanger, F. Boudjema, C. Hugonie, A. Pukhov and A. Semenov, JCAP **0509** (2005) 001 [hep-ph/0505142].

[60] U. Ellwanger and C. Hugonie, Comput. Phys. Commun. **177** (2007) 399 [hep-ph/0612134].

[61] M. Muhlleitner, A. Djouadi and Y. Mambrini, Comput. Phys. Commun. **168** (2005) 46 [hep-ph/0311167].

[62] S. F. King, M. Muhlleitner and R. Nevzorov, Nucl. Phys. B **860** (2012) 207 [arXiv:1201.2671 [hep-ph]].

[63] G. Belanger, F. Boudjema, A. Pukhov and A. Semenov, arXiv:1305.0237 [hep-ph].

[64] [CMS Collaboration], CMS-PAS-HIG-13-005.

[65] [ATLAS Collaboration], ATLAS-CONF-2013-014.

[66] B. C. Allanach, eConf C **010630**, P319 (2001) [hep-ph/0110227].

[67] A. Djouadi, hep-ph/0211357.

[68] B. C. Allanach, S. Kraml and W. Porod, JHEP **0303**, 016 (2003) [hep-ph/0302102].

[69] B. C. Allanach, A. Djouadi, J. L. Kneur, W. Porod and P. Slavich, JHEP **0409**, 044 (2004) [hep-ph/0406166].

[70] J. -J. Cao, Z. -X. Heng, J. M. Yang, Y. -M. Zhang and J. -Y. Zhu, JHEP **1203** (2012) 086 [arXiv:1202.5821 [hep-ph]].

[71] M. Pettini, B. J. Zych, M. T. Murphy, A. Lewis and C. C. Steidel, MNRAS, **391** (2008) 1499.

[72] J. Geiss and G. Gloeckler, Space Sience Reviews **106**, 3 (2003).

[73] M. Pettini and R. Cooke, Mon. Not. Roy. Astron. Soc. **425**, 2477 (2012) [arXiv:1205.3785 [astro-ph.CO]].

[74] R. Cooke, M. Pettini, R. A. Jorgenson, M. T. Murphy and C. C. Steidel, arXiv:1308.3240 [astro-ph.CO].

[75] G. W. Bennett *et al.* [Muon G-2 Collaboration], Phys. Rev. D **73** (2006) 072003 [hep-ex/0602035].

[76] M. Davier, A. Hoecker, B. Malaescu and Z. Zhang, Eur. Phys. J. C **71** (2011) 1515 [Erratum-ibid. C **72** (2012) 1874] [arXiv:1010.4180 [hep-ph]].

[77] K. Hagiwara, R. Liao, A. D. Martin, D. Nomura and T. Teubner, J. Phys. G **38** (2011) 085003 [arXiv:1105.3149 [hep-ph]].

[78] S. Chatrchyan *et al.* [CMS Collaboration], Phys. Rev. Lett. **111** (2013) 101804 [arXiv:1307.5025 [hep-ex]].

[79] RAaij *et al.* [LHCb Collaboration], Phys. Rev. Lett. **111** (2013) 101805 [arXiv:1307.5024 [hep-ex]].

[80] Y. Amhis *et al.* [Heavy Flavor Averaging Group Collaboration], arXiv:1207.1158 [hep-ex].